Porous Organic and Inorganic-Organic Hybrid Materials for Electrochemical Energy Conversion & Storage

---

A Thesis Submitted for the Degree of

MASTER OF SCIENCE

as a part of the

Integrated Ph.D Programme

(Materials Science)

By

Tarandeep Singh

Chemistry and Physics of Materials Unit (CPMU)
Jawaharlal Nehru Centre for Advanced Scientific Research (A Deemed University)
Bangalore – 560064

Dedicated to my
FAMILY

DECLARATION

I hereby declare that the matter embodied in the thesis entitled "***Porous Organic and Inorganic-Organic Hybrid Materials for Electrochemical Energy Conversion & Storage***" is the result of investigations carried out by me at the Chemistry and Physics of Materials Unit, Jawaharlal Nehru Centre for Advanced Scientific Research, India under the supervision of Prof. Tapas Kumar Maji and that it has not been submitted elsewhere for the award of any degree or diploma.

In keeping with the general practice in reporting the scientific observations, due acknowledgement has been made whenever the work described is based on the findings of other investigators. Any omission that might have occurred due to oversight or error in judgement is regretted.

Tarandeep Singh

CERTIFICATE

I hereby certify that the work described in this thesis entitled "***Porous Organic and Inorganic-Organic Hybrid Materials for Electrochemical Energy Conversion & Storage***" has been carried out by Tarandeep Singh under my supervision at the Chemistry and Physics of Materials Unit, Jawaharlal Nehru Centre for Advanced Scientific Research, India and that it has not been submitted elsewhere for the award of any degree or diploma.

Prof. Tapas Kumar Maji
CPMU, JNCASR
(Research Supervisor)

Acknowledgements

I wish to express my heartfelt gratitude to my research supervisor Prof. Tapas K. Maji for his constant support, guidance and encouragement to try new research areas throughout the course of investigation. His invaluable suggestions and ideas have always inspired me to think out of the box and tackle any problem in a simple way. His enthusiasm and dedication towards research has always motivated me to work much harder than doing at the present to strive for excellence.

Prof. C. N. R. Rao, FRS, has always been a source of inspiration. Being in JNCASR gave an opportunity to learn a lot from him by his enlightening scientific lectures and motivational talks.

I express my deep gratitude to Prof. Chandrabhas Narayana, Chairman of CPMU, for allowing me to use various facilities of the Centre and always encouraging me.

I am thankful to the faculty members of JNCASR for their great courses that have enriched my knowledge about science. I specially thank Prof. S. Balasubramanian, Prof. M. Eswaramoorthy, Prof. Sarit S. Agasti, Prof. K.S. Narayan, Prof. Chandrabhas Narayana, Prof. Rajesh Ganapati, Prof. A Sundaresan, Prof. Shobhana Narasimhan, Prof. Ranjan Dutta, Prof. Sridhar Rajaram, Prof. Umesh Waghmare, Prof. Swapan K. Pati, Prof. Kanishka Biswas, Prof. Sebastian C. Peter, Dr. Prem Kumar, Prof. Tapas K. Maji and Prof. Aloknath Chakraborty of IISc for their courseworks that have helped me a lot during research.

I am thankful to all my collaborators: Dr. Debabrata Samanta for his fruitful discussions in computational calculations and help in synthesis and characterization a material, Dr. Ashish Singh for his help in OER measurements, Dr. Chayanika Das for helping me to learn electrochemistry, Ms. Neha and Prof. Swapan K. Pati for their motivation, discussion and computational studies which helped a lot in understanding the reasons for the results obtained.

I am also thankful to all the technical staff members of JNCASR, namely Mr. Anil, Mr. Vasu, Mr. Alla Srinivas Rao, Mr. Mahesh, Mrs. Usha and Ms. Selvi for their timely help.

I also thank JNCASR library, Complab, Hostel, Dhanvantri, Academic Section and all the Administrative staff who have made my stay at JNCASR very comfortable and pleasant from the day I am here.

My special thanks to all my lab family: Syamantak da, Sohini di, Shubhajit da, Ashish bhaiya, Sanchita, Subarna di, Suresh bhaiya, Parul di, Faruk, Alolika, Rambabu bhaiya, Debu da, Nivedita di, Papri di, Pramod and Chayanika di. My research would not be possible without their guidance at every step. Moreover their caring, cooperative, helpful and friendly nature made a perfect enjoyable atmosphere for research or outside the lab during lab treats etc. My sincere thanks to Sohini di for her help and guidance from day 1 when I entered the lab.

I would also like to thank Supreeti Mam for being a wonderful host, kind gesture, lots of food, especially tasty muffins, and, Neel and Sonai for their wonderful company.

My sincere thanks to all my Int. Ph.D. batch mates for their constant love and support throughout my stay in JNCASR.

I am thankful to my undergrad teachers, especially Dr. Venus for believing in me always and motivating me to do research. His hard work and time spent with me for the preparation of my entrance exams helped me a lot to take my first step into research.

Also I thank my undergrad friends and school friends: Gourav, Robinder and Inderpreet for being just a call away always and the fruitful discussions.

I am also very thankful to my Cooper Pair Dr. Ankush Kumar for being there always with me and motivating me. His support and guidance have helped me a lot to learn about research. I still miss the discussions we had over meals. I thank him for being there with me from my first day in JNCASR.

Last but not the least! My family members without whom I would not be what I am here today. I don’t have words to thanks my family members who are always beside me and never letting me feel alone. Constant motivation by my family members, specially my brother Gursimar Singh and my parents have always pushed me to do something unique, dream big and work hard to achieve it. I also thank Jasveen didi for always being there with me & motivating me and Harmehar Singh for his infinite love and being a constant source of entertainment.

Above all, I am always thankful to The Almighty who always showered His choicest blessing on me. Without Him, I would not be here and stand nowhere. I am grateful for His abundant blessing in every endeavor I have taken.

Preface

This thesis consists of five chapters and discusses about energy conversion and storage in porous organic and inorganic-organic hybrid materials.

Chapter 1 describes various inorganic-organic hybrid and organic porous materials. Further it discusses the electrocatalytic reactions such as oxygen reduction reaction (ORR), oxygen evolution reaction (OER) and hydrogen evolution reaction (HER) and the application of these reactions in Zn-air batteries and water electrolysis.

Chapter 2 discusses the design, synthesis and characterization of a nanoscale metal organic framework (NMOF) with redox active ligand and the design of the framework lead to close placement of donor and acceptor ligands. NMOF shows photochromic, electrochromic nature and electrochemically reduced ligand is stabilized by different counter cations.

Chapter 3 deals with porous materials derived from metal-organic frameworks. The obtained carbonaceous material is studied for HER. This is further used as cathode material for Zn-air batteries and is also used as a catalyst for electrochemical overall water splitting.

Chapter 4 describes the design synthesis and characterization of redox-active donor-acceptor conjugated microporous polymer (CMP). The metal free CMP is studied for ORR and HER. Moreover, Co nanoparticles are in-situ stabilized which lead to the introduction of OER. Further, Zn-air batteries were fabricated which were used to power water electroyser and thus self powered overall water splitting was shown.

Chapter 5 contains the synthesis of porphyrin based redox-active donor-acceptor conjugated microporous polymer (CMP). The metal free system was studied for ORR. Upon metallation, CMP showed ORR, OER as well as HER. This was used as a cathode material for Zn-air battery. Metallated CMP being trifunctional in nature was used as both anode and cathode material for water electrolysis. Moreover, the fabricated battery was shown to be sufficient to power water electrolyzer and thus lead to H_2 and O_2 evolution.

TABLE OF CONTENTS

Introduction

Photo- and Electrochromic Nanoscale Metal-Organic Framework

MOF Derived Co_3O_4@Co/NCNT Nanocomposite for Electrochemical Hydrogen Evolution, Flexible Zinc-Air Batteries and Overall Water Splitting

Chapter 1

Introduction

1. Porous Materials for Energy Storage and Conversion

Global warming, energy conversion and energy storage are some of the major challenges in today's world. As the world population is rising at a fast rate, the burden on fossil fuels, to fulfill the energy demands, is increasing drastically. It is predicted that the energy demand will grow by two folds in next 15 years.[1] So the major concern for the scientists is to find out cheap, clean and renewable energy sources. This can be achieved in several ways, one of them being the use of electrochemical reactions. Several electrochemical energy systems have been developed but the most effective and efficient developments include fuel cells, electrochemical overall water splitting and metal-air batteries. But these all rely on some basic yet energy demanding processes which include oxygen reduction reaction (ORR), water oxidation or oxygen evolution reaction (OER) and hydrogen evolution reaction (HER). These reactions generally take place at the surface, but the catalytic activity can be improved if the reactants reach the catalytic sites, not only on the surface but also in the bulk. So, the best deal to make this is possible is to use the high surface area porous materials (Figure 1) for the energy storage and conversion as the active materials.

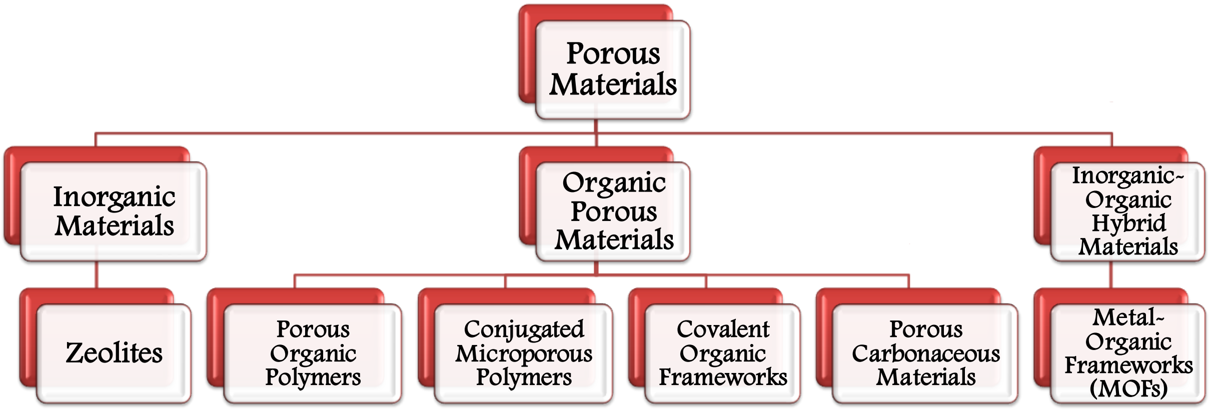

Figure 1: Schematic showing three classes of porous materials.

The introduced porosity will not only help in the accessibility to the active sites but also will help in enhanced mass transport and diffusion of the reactant. Few of the common routes for the development of porous materials include the use of hard templates such as mesoporous silica, carbon or soft templates such as surfactants.[2, 3] Zeolites are inorganic microporous materials, with well-defined pores, which are formed by the tetrahedral of Si, P, Ge, Ga etc with O.[4] But, the lack of ability to functionalize the pore restricts its desired tunability towards various applications. As a solution to this, metal-organic frameworks (MOFs) or porous coordination polymers (POPs) came into the existence. MOFs are crystalline porous materials consisting of infinite array of metal ions joined with functionalized organic ligands via coordination bonds. Various types of metal nodes and organic linkers can be assembled into MOFs via hydrothermal/solvothermal reactions,[5-7] metal-ligand solution layering[8] etc. MOFs have been extensively used in gas storage and separation,[9-15] catalysis,[16-19] magnetism,[8, 20, 21] sensing[22-24] and many more. Downsizing of MOFs particle size to nanometer scale regime has opened many new applications as in drug delivery,[25, 26] diagnostics,[27, 28] solar cells[29] etc. Their nanometer scale morphology helps to disperse these MOFs better in aqueous or non-aqueous medium and thus helps in increasing the processability for coatings on various substrates for device based applications.[30] Further, in recent past, MOFs have been proved to be excellent templates and precursors for the synthesis of various nanostructures such as metal oxides,[31, 32] metal phosphides,[33-35] metal carbides[36] and even metal nanoparticles.[37, 38] This can be done by carbonizing the MOFs at higher temperature. Moreover, MOF derived materials have shown excellent properties in field of catalysis,[38, 39] energy storage and conversion.

Another very unique class of materials are conjugated microporous polymers(CMPs) which consist of both nodes and spacers as organic molecules connected via covalent bonds, and are often microporous in nature. These can have high surface area reaching upto 1115 m^2/g.[40, 41] Not only this, CMPs have characteristic high chemical and thermal stabilities as compared to its monomers or other linear polymers. Moreover their π-conjugated backbones provide certain advantages, such as high quantum yield fluorescence, semiconducting nature, efficient exciton migration if compared to non-porous linear analogues.[42] It is beyond any doubt that zeolites posses much more thermal stability, MOF posses much more chemical functionalities and carbonaceous materials posses much more conductivity values as compared to CMPs. But what makes them unique is the combination of all the properties of different materials into a single moiety and thus making it a potential material to be used not only in conventional applications, such as gas storage and separation,[43-45] but also in various catalysis[46-48] and, energy storage and conversion devices.[49, 50] Herein, in this introductory chapter, we discuss about various synthetic techniques, challenges and finally introduce these materials as electrocatalysts for ORR, OER and HER. Further, the utilization of these reactions in metal-air batteries (particularly Zn-air battery) and water electrolyzers is discussed.

2. Synthetic Strategies of MOFs and Potential Applications

MOFs constitute two central components in the framework. As the name suggests, metal centers act as nodes while organic ligands as the connectors.[51] Various motifs can be obtained depending on the nature of metal ion, metal-linker stoichiometry, and structure functionalization of the ligand, solvent used, temperature and many more.[52] Thus the important parameters which decide the motif include the co-ordination number of the metal ion and the number of co-ordinating sites of the linker. Co-ordination number of the metal ions can change from 2 to 7 and thus giving a variety of geometries. The geometries vary from linear, T-shaped, tetrahedral and all the way to pentagonal-bipyramidal and their distorted forms (Figure 2a). Instead of using the free metal ion, metal complexes help in controlling the bond angles, number of co-ordinating sites etc. Also, the sites which are not required can be blocked by the use of macrocycles or chelating ligands. On the other hand, the geometry and type of the linker also plays an important role. Few of the commonly used linkers are shown in the Figure 2b.

MOFs also possess various types of linkages between the metal ion and the ligands. These can be the simple co-ordinate bonds, co-ordinate bonds along with H-bond, co-ordinate bonds along with other interactions such as π-π interaction or C-H$\cdots\pi$ interaction between the ligands and the co-ordinate bond along with the mixture of other interactions.[51] Various ways can be used for the synthesis of MOFs. Conventional methods include solvothermal/ hydrothermal techniques, simple heating of the mixture of metal ions and the ligand in aqueous or non aqueous medium. But the modern ways include mechanochemical synthesis,[53] electrochemical synthesis[53, 54] or by the use of microwaves.[55, 56] Various applications of MOFs[57] are shown in Figure 3.

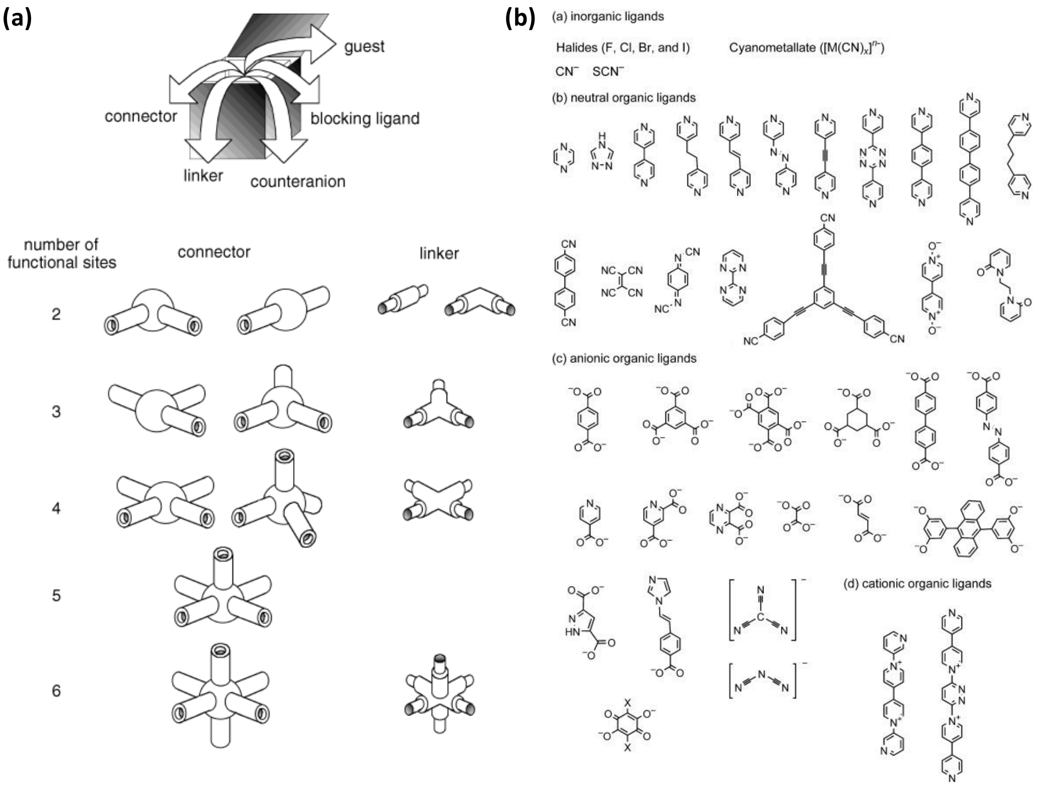

Figure 2: (a) Schematic showing possible geometries that can be formed by using different linkers and metal connectors; (b) Common linkers used for the synthesis of MOFs. Reprinted with permission from ref. no. 51.

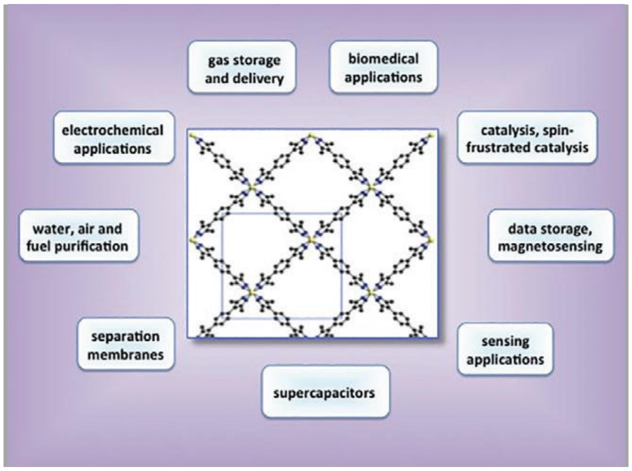

Figure 3: Applications of MOFs. Reprinted with permission from ref. no. 57.

2.1 Nanoscale Metal-Organic Frameworks

Downsizing the materials to nanoscale is a well known strategy, which is exploited from long ago and is known to enhance the properties of the material by many folds as compared to the bulk counterpart.[30, 58] It is often observed that the properties possessed by nanoscale materials even surpass that observed in the bulk state of art materials. One of the primary observations on scaling down the material is the many fold increase in its surface area. Various organic and inorganic nanoscale materials are already developed, but the formation of hybrid organic-inorganic nanoscale materials is still a hot topic being worked upon. Till date, despite the porous nature of MOFs and many other fascinating properties, these were not the choice for the device fabrication due to non-processable nature. So, the development of processable nanoscale MOFs (NMOFs) is required to fill the gap between the requirements for fabrication techniques and the outstanding properties of MOFs. Lowering even one dimension to nanoscale leads to many changes in properties, reactivity etc. This approach is not only proved beneficial in the field of catalysis, sensing,[59, 60] light emitting applications or devices[61] but also in various biological studies. Nowadays, NMOFs are widely used for drug delivery, biomedical imaging, intracellular pH sensing in live cells,[62] drug carries, MRI contrast agents[63] and many more.[64, 65] The applications of NMOFs are not only affected by the size, but also the shape and the morphology. So the morphology and the shape can be tuned to meet the desired applications. As an example, the spherical shaped NMOFs are more effective for drug release because of the uniform degradation of the framework. On the other hand, non spherical or asymmetrical shaped frameworks possess better catalytic activities. This is due to the lower mass transfer limit and higher surface area in NMOFs. Theoretically, it is found that the most active catalytic sites are present at the edges and corners as compared to the facets. So the asymmetric shaped NMOFs also helps in exposing more number of corners and edges to the reacting species and thus improve the efficiency.[58] NMOFs can be broadly classified into three categories based on their dimensionality. These include 0-D NMOF which are equivalent to particles, 1-D include those possess fiber, tube or rods like morphology and 2-D include thin films and membranes as shown in Figure 4.[66]

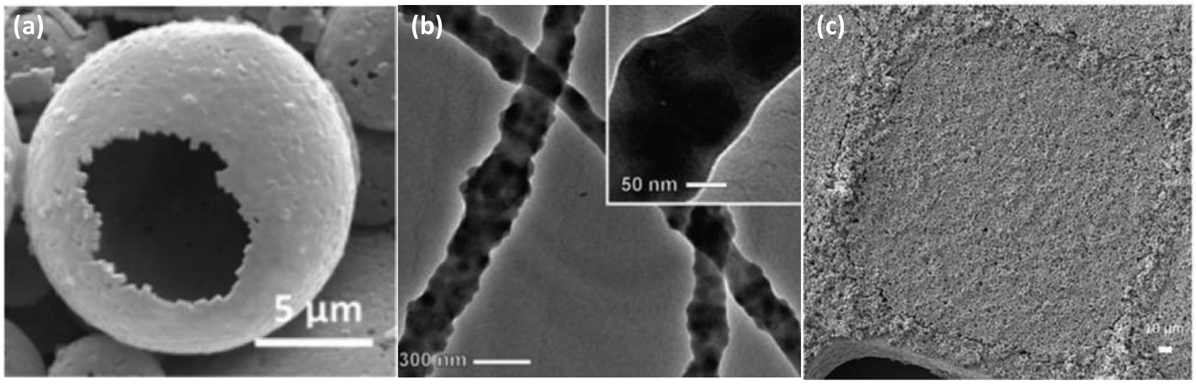

Figure 4: (a) 0-D nanostructures; (b) 1-D nanostructures; (c) 2-D nanostructures. Reprinted with permission from ref. no. 66.

2.1.1 Synthesis Techniques

The combination of the properties of MOFs to those possessed by nanoscale materials can increase the scope of MOFs to a different level. This can be achieved by following the 'bottom up approach', which is commonly used in the synthesis of nanomaterials. This strategy focuses on the control of the self-assembly of building blocks at the nanometer scale. The presence of enormous number of metal ions and organic ligands has led to the formation of a library of NMOFs. Some of the common ways to synthesize 0-D or 1-D nanoscale metal-organic frameworks include (a) the confined growth of the supramolecular assembly at nanoscale by the use of emulsions or template, (b) controlled precipitation of self-assembled metal–organic polymers by the use of poor solvents, by fast precipitation by the use of external agents such as microwave radiation, ultrasounds, and solvothermal/hydrothermal methods by careful choice of the solvents.[30] In (a), nanoemulsions are formed by the use of surfactants, for which the size ranges from 50 nm to 1000 nm, and these small droplets act as the "nanoreactors" to confine the self-assembly and thus control the nucleation and growth process of the metal-organic frameworks. In this approach, the precursors are initially dissolved in the solvents that will be dispersed. Further, oil-in-water (or the vice-versa) emulsions are formed by the use of surfactants. The collision between the droplets containing the precursors, upon the application of external stimuli, starts the self assembly process but due to the confinement into the nanospace, the growth process is limited to nanoscale. This leads to the formation of NMOFs.[67, 68] In the latter approach (b), reaction conditions are designed in such a way that favors the fast nucleation process. As it is well known from the synthetic strategies of MOFs, that on increasing the temperature, increases the solubility of the precursors which lead to the slow precipitation process leading to the thermodynamic product, and thus helping the crystallization to occur. So, this can be avoided by the use of microwave irradiation, ultrasonic waves or by the choice of the solvent which helps in the fast precipitation of the frameworks formed.[69, 70] Another very effective method for the synthesis of NMOFs is the coordination modulation method, in which, a molecule similar to the ligand, but having single functionality, is used to bind to the metal center and thus prevent further self-assembly.[71, 72]

As discussed above, the product size and morphology also play an important role for tuning the application as per the desired requirements. So various strategies have been followed to control the shape and size of the resulting NMOF. It is found that type of the solvent, nature, stoichiometry, concentration of the building blocks and the reaction conditions play a crucial role in deciding the size and shape of the NMOFs.[30] In a report, Jung *et al*. studied the formation of NMOF by using Zn(II) and metallosalen as the building blocks by the variation of the ratio of DMSO/DMF used during the solvothermal reaction and observed the variation in sizes of the nanocubes formed on changing the solvent.[73] In the same report, the effect of reaction temperature was also studied and it was concluded that on increasing the temperature of the reaction lead to the increment in the particle size. In an another report, Ni *et al*. showed the effect of the concentration of the building blocks on the formation on NMOFs when synthesized by using the microwave. Whereas, Lin *et al*. varied the composition of the surfactant, and thus the composition of the emulsions to produce Gd(II)-BDC nanorods, the length of which could be altered by changing the molar ratio between the water and surfactant.[74]

2.1.2 Applications

NMOFs gives the advantage of utilizing the individual properties of the metal ions and the organic ligands along with their synergistic effect.[30] As an example, the interaction of metal ions with phonons and electrons can lead to applications such as tunable luminescence and other light harvesting properties[75, 76] or can show interesting magneto-optic behavior.[77]

On the other hand, the presence of organic ligands shows their distinct properties such as fluorescence, chromism, formation of radicals etc. Due to these properties, NMOFs have been utilized to show the electrochromic and photochromic behavior. With these properties, NMOFs open up a completely new class of applications in which they can be utilized. Some of them are briefly discussed.

2.1.2.1 Photochromism and Electrochromism

Photochromic materials are known to go through chemical transformation between different states possessing different properties, the transformation for which is initiated by the electromagnetic waves, atleast in one direction. The chemical transformation should be reversible in nature either thermally or photochemically. Photochromism is being studied from long age, since its discovery in 1867 by Fritsche when it was first observed in orange tetracene.[78, 79] Since then, it did not gain much interest as of today due to its vast application in memory and display devices, optical fibers, solar cells etc. Various organic and inorganic photochromic systems are known but the combination of photochromism along with the nanosystem would lead to enthralling properties. Light stimulated tuning in HOMO-LUMO band gap due to the modulation in the electronic arrangement in a molecule results in photochromism. This may lead to the change in properties such magnetism, electrical conductivity, catalytic activity etc. Photochromism has been introduced into various nanosystems such as nanomachines,[80, 81]nanoelectronics[82-85] (molecular junctions, OFETs, photochromic response towards superconductivity), various self assembled systems such as polymers, liquid crystalline superstructures[86] etc. Apart from this, various biological nanosystems[87] [88-90] (including nucleic acids, receptors ion channels etc) and also the porous structures such as metal-organic cubes or metal-organic frameworks have shown photochromism[91, 92] and therefore the photochromic response such as controlled capture or release of the guest molecules on shining the light. For instance, Murase *et al*. designed a coordination cage with the composition of $Pd_{12}L_{24}$ containing 24 azobenzene units most of which are located towards the interior of the cage. Initially, the cavity (formed when azobenzene is in trans form) being hydrophobic in nature, was able to encapsulate pyrene and 1-pyrenecarboxlic acid in the cavity. But on shining of UV light (azobenzene converted to cis form), the reversal of hydrophobicity was observed, thus making the pore less hydrophobic which resulted in the release of the guest molecules.[93] Various metal-organic cages have been designed and synthesized with functionalized photoswitchable ligands that have been used in various biomedical applications. Further, photochromic MOFs or NMOFs can be synthesized by encapsulating photochromic guest molecules into the framework or by the inclusion of the photochromic ligand in the framework. Kitagawa *et al*. encapsulated azobenzene into Zn_2(terephthalate)$_2$(triethylenediamine) MOF which showed the variation in the available space in the pore for N_2 on changing the the azobenzene from trans to cis form.[94] Whereas, Zhou *et al*. synthesized MOF containing the photochromic ligand containing azobenzene side chains. It was demonstrated that trans to cis isomerization of azobenzene decreased the CO_2 uptake of the MOF which may be due to the blockage of the adsorption sites by the azobenzene molecule in cis form.[95] On the other hand, Yaghi *et al*. synthesized non-interpenetrated 1D Mg based MOF containing pendant photochromic azobenzene and demonstrated the release of the dye molecules on shining the light.[96]

Electrochromic materials are known to undergo the change in absorbance spectrum on the application of potential and thus, reducing or oxidizing the redox active species. The change obtained should be reversible in nature. As the population is increasing at a fast rate, the need for energy to maintain comfortable temperature and lightning inside the building is increasing drastically.[97, 98] Electrochromic material has the potential applications in the development of smart windows (the optical properties of which can be tuned on the application of potential). Other potential applications of electrochromic material include information displays, self-dimming rear mirrors for automobiles, electronic papers, electrochromic e-skins, and so on. An electrochromic device generally consists of 5 layers which include glass with transparent conductor, ion storage film, electrolyte (ion conductor), electrochromic film and transparent conductor.[98] In brief, a transparent electrically conducting layer (generally ITO or PEDOT:PSS) is coated onto a transparent substrate, mostly glass or plastic (in case of flexible substrate). On one side, the electrochromic material forms a thin layer followed by the liquid or gel electrolyte. The electrolyte is an ionic conductor and can easily conduct small ions such as Li^+ or H^+, but is an electron insulator. This is followed by the other layer of ion collector, on the conducting substrate. On the application of potential, the charge on the electrochromic layer is balanced by the counter ion from the electrolyte. Thus, the efficiency will depend upon the facile movement of counter ions inside the electrochromic layer. So, the use of highly porous and stable materials would be a great deal to work upon.[99] But, electrochromic materials have not been commercialized due to their high cost, low coloration efficiency, slow response time, requirement of high potentials and short-term durability. Electrochromic MOFs or NMOFs can be synthesized by using redox-active ligand as the linker which undergoes the change in absorbance spectrum in the visible range. Till date, various inorganic (transition metal oxides such as tungsten oxide, niobium oxide),[100] metallo-organic (such as polypyridyl complexes with metal ions, prussian blue analogs)[101-104] and conducting organic polymers (polyanilines, polypyrrole, polythiophenes)[101] have been studied as electrochromic materials. Apart from these, MOF thin film have been grown which contain the redox active groups that show electrochromic behavior upon reduction or oxidation. For instance, Dinca *et al*. grew MOF thin films consisting of Zn^{2+} ions and bis- (pyrazolyl)naphthalene diimide (Zn-NDI) as ligand onto glass coated FTO (Figure 5a,c).

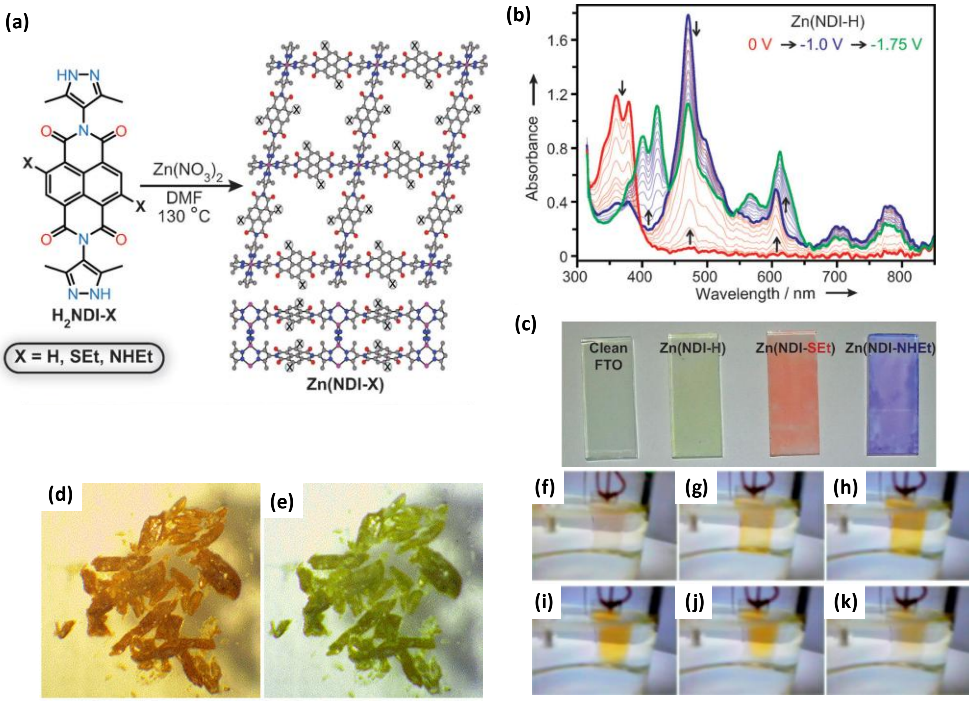

Figure 5: (a) Image showing the structure of Zn(NDI-X) MOF; (b) Spectroelectrochemical data for X = H; (c) Optical images showing the films of Zn(NDI-X) on FTO; (d,e) Image showing photochromism in NBU3; (f-k) Images showing the electrochromic behavior of NBU3. Reprinted with permissions from ref. no. 105 and 107.

It was shown that naphthalene diimide ligands underwent one and two electron reduction on the application of potential and thus change in colour was observed. The change in absorption spectra was observed on formation of radical anion and the dianion (Figure 5b). Due to the same reason, different colour changes were observed on the films varying as green for H, red for SEt and blue for NHEt.[105] On the other hand, Hupp *et al*. showed reversible electrochromism in MOF consisting of free standing acicular nanorods.[106] Many other electrochromic materials are synthesized but the materials possessing both electrochromism and photochromism are still being explored. Recently, Han *et al* synthesized [Zn(NDI-ATZ)$(DMF)_2]_n$ (NDI-ATZ = NDI based tetrazole ligand) (NBU3) which underwent a colour change from yellow to green on keeping in sunlight for 15 min and came back to the original state by keeping in dark for 1 hour (Figure 5d,e). Along with this, electrochemical behavior was also studied as shown in Figure 5f-k. Photoinduced and electrochemical radical generation on NDI was found to be responsible for the dual behavior.[107]

3. MOF Derived Nanomaterials for Energy Storage and Conversion

3.1 MOF Derived Carbonaceous Nanostructures

Apart from the nanoscale MOFs, nanostrucutres derived from MOFs, as the precursors or templates, are another class of porous materials which are obtained by the high temperature pyrolysis of the framework followed by physical and chemical treatments. Long ago, the nanoporous carbonaceous materials formed by traditional methods possessed good porosity along with high surface area, but also possessed disordered structure with a broad distribution of the pore size. So to overcome these limitations, hard and soft template techniques were followed. The hard templates used to obtain carbonaceous materials generally include zeolites or mesoporous silica which result in the formation of ordered micro, meso and macro pores.[108-111] But the lack of ability to functionalize the pores as per the requirement restricts its use. The other technique which uses soft templates requires the thermal decomposition of the organic precursors before the carbonization process is complete. This generally results in the diverse structures and morphologies. Moreover, the fine control over the composition and thus the resulting morphology is difficult even if simple mixture of metal salt and the organic moiety is used as the precursor. So, to get the precise control over these factors, the idea of carbonizing MOFs came into the picture. As the linkers in MOFs can be easily tuned for different applications, thus the carbonization of the MOFs leads to complex compositions along with the required functionalizations which in return show the enhanced properties. Moreover, the low temperature (≈500 °C) pyrolysis helps to maintain the precise control over shape, size and structure along with high stability, large surface area and high conductivity.[112, 113] So these materials are proved to be the potential candidates for applications in gas storage and separation,[114-116] sensing,[117-119] energy storage and conversion etc. Above all this, the use of heteroatom containing ligand in the preparation of MOFs can help to control the amount of the doping in the derived structure. The doping of the heteroatom results in the tuning of the overall electronic structure. So with MOFs as the precursors, the electronic and geometric structure can be precisely controlled as per the requirements. Another way to dope heteroatoms in the derived materials focuses on the encapsulated guest molecules in the MOF framework. As another face of the MOF derived materials, these can also be used for the stabilization of the nanoparticles within the pores. Jayaramulu *et al*. showed the synthesis of nanoporous boroncarbonnitride derived from a Zn MOF consisting of bim (tetrakis(1-imidazolyl)borate) and 1,4-ndc (ndc = naphthalenedicarboxylate) as the ligands. The resulting BCN showed the coral-like morphology with high surface area of 988 m^2/g. This showed good uptake and storage properties of CO_2 and H_2. Moreover, it was shown to be a good support for the stabilization of Au and Pd nanoparticles.[120] Apart from the above applications, MOF derived materials are also known to be highly active and stable electrocatalysts for ORR , OER and HER, and cathode materials for metal-air batteries. Figure 6 shows the timeline of development of MOF derived materials for energy storage and conversion applications.[113]

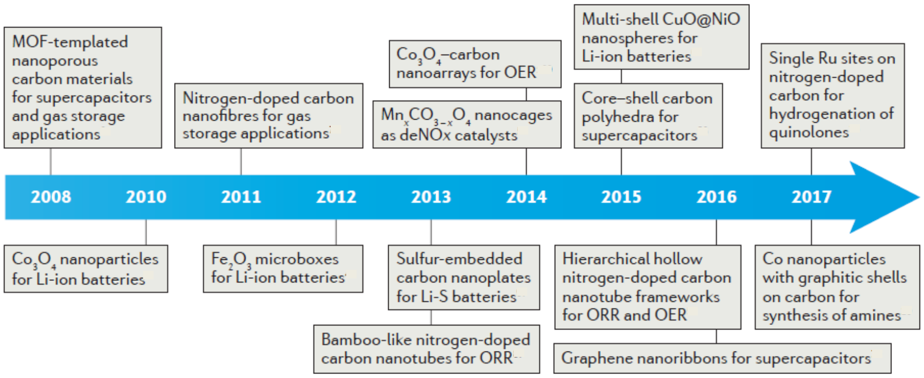

Figure 6: Timeline showing the development of MOF derived materials for energy storage and conversion applications. Reprinted with permission from ref. no. 113.

3.2 Electrocatalysis

Many electrochemical reactions are energy demanding processes and thus do not proceed easily due to the large activation barriers. So the electrocatalysts need to be developed which lowers the activation barrier of these electrochemical reactions along with the improvement in efficiency and the selectivity of the products formed. The electrode reaction mainly occurs only at the interface of the catalyst and the electrolyte. So only a few layers of the catalyst will be exposed to the electrolyte and thus not exposing all the active sites for the reaction to occur. This will lead to low efficiency of the catalyst. So to prevent this mass loss, designing a hollow porous structure would be a good strategy to work upon. The hollow porous nature of the catalyst will help in improved mass transport and easy diffusion of the reactants and the products to and from the catalytic sites. Moreover, MOFs contain the metal centers or other heteroatoms in a periodic fashion. So, the carbonization of the MOF templates helps in uniform distribution of the hetroatoms throughout the structure. Also, in many cases, it has been observed that the metal ion is converted to metal nanoparticles on carbonization. Theoretically it is shown that the catalytic activity is maximum if catalytic site is lying on the edge or the vertex of the solid material instead of being in the face. So, using MOFs as the template prevents the agglomeration of the nanoparticles to each other and also expose most of the catalytic active sites at the edges or the facets.[121]

Core-shell nanostructures are found to be highly active for electrocatalytic activites. This is due to the synergistic effects between the core and the shell and thus the electron density of the outer shell may vary due to the presence of the core. Recently, Lu *et al*. designed and synthesized a core-shell bifunctional electrocatalyst showing good ORR and HER activities. In this work, zinc and iron doped porous carbons were synthesized by pyrolysis of bimetallic Zn and Fe containing MOF which was wrapped around the Au nanoparticles (Au@Zn-Fe-C). It is shown that this possessed very good ORR activity with a low onset of 0.94 V v/s RHE along with high stability and methanol tolerance. Also, Au@Zn-Fe-C was shown to be highly active for hydrogen evolution reaction in acidic medium with onset of -0.08 V v/s RHE. It was shown that the activity of the catalyst varied with the amount of Au nanoparticles loaded and the thickness of the metal-carbon shells. Also, Au nanoparticles played an important role by promoting the electron transfer to zinc-iron embedded porous carbon.[122] In an another report, hollow frameworks consisting of nitrogen doped carbon nanotube framework (NCNT) were synthesized by pyrolysing a well known metal-organic framework ZIF-67 without any other precursor. The framework showed bifunctionality towards ORR and OER and showed outstanding performance by overcoming the performance by the state of art catalyst Pt/C. In-situ cobalt nanoparticles formed during the pyrolysis process were removed by the acid treatment. Also, the morphology of ZIF-67 particles even after pyrolysis is retained. The rough surface obtained showed the formation of various NCNTs on its surface. Moreover, the open voids obtained, showed the hollow nature of the formed nanotubes. The high catalytic activity of metal free NCNTs obtained is assumed to be the result of the chemical composition and the hollow structure.[113] Apart the the electrocatalysis, MOF derived nanostructures also show various application in energy storage devices as discussed in the following section.

3.3 Energy Storage

Electrochemical energy storage devices have received huge attention in recent past for their use in modern electronic devices. Although Li-ion batteries were developed long back and have been commercialized on huge scale but have several limitations such as safety concerns, high cost and scarcity of Li metal in Earth's crust. So, to avoid the use of Li, various alternatives are being developed such as Na-ion batteries,[123] Zn-air batteries[124] etc. But these are still at their infancy stage. Various materials have been developed for the applications in these batteries but MOF derived nanostructures are receiving a lot of attention because of their tunable structure and chemical composition, porous nature, bifunctional nature towards electrocatalysis and many more, as already discussed. In a report, Fan *et al*. developed amorphous carbon nitride and zinc oxide composite by pyrolysis of ZIF-8. The material possessed high thermal stability and was used as the anode material in Na-ion battery. Moreover, the robust chemical nature of the composite offered highly stable electrochemical behavior with only 0.016 % loss in capacity per cycle in 2000 cycles at the current density of 1.67 A/g.[125] In an another recent report Wang *et al*. reported another MOF derived nanostructure which was used as the anode material in Na-ion battery. In this report, ZIF-67 was consciously chosen as it contained Co^{2+} metal centre along with nitrogen rich 2-methylimidazole as a source for nitrogen doped carbon (NC). ZIF-67 was pyrolysed in two steps. The first yielded the small metal particles covered with NC. This was further annealed at lower temperature in air which gradually converted Co to Co_3O_4 and thus yielding Co_3O_4@NC. Moreover, this retained the morphology of ZIF-67 along with Co_3O_4@NC at the surface, as revealed by the TEM images. On examining the electrochemical performance, Co_3O_4@NC showed high capacity and ultra-long cycling stability with a capacity degradation of only 0.03% per cycle with the 1100 cycles at 1 A/g.[126] Apart from the Na-ion battery, the bifunctional behavior of various derived materials for ORR and OER makes them potential materials for electrically rechargeable metal-air batteries. Various MOF derived materials are used as cathode materials in zinc-air batteries. In one of the recent reports, Wang *et al*. pyrolysed a 2-D dual metal (Co/Zn) zeolitic imdazole framework . This led to in-situ formation Co nanoparticles which were uniformly distributed in the derived NCNT matrix. This material being bifunctional electrocatalyst possessed both ORR and OER, a rechargeable Zn-air battery was constructed which gave an OCP of 1.365 V along with the current density of 90 mA/cm^2 at 0.8 V and yielded the power density of 101 mW/cm^2.[127] Similarly, various MOF derived materials are also well known for other energy storage applications such as Li-S batteries[128, 129] or supercapacitors.[130, 131]

4. Conjugated Microporous Polymers

The idea of designing and utilizing porous materials started all the way back from zeolites & mesoporous silica and then to modern class of materials which include MOFs and MOF derived materials for various applications. Another fascinating class of porous materials is completely organic porous polymers and among this includes a very unique class of polymers known as conjugated microporous polymer (CMPs). As the name suggests, CMPs are completely π-conjugated polymers possessing intrinsic microporosity (i.e. pore size is less than 2 nm) and thus possess high surface area. These polymers are formed by the covalent bonding between fully conjugated nodes and linkers, resulting in a three dimensional (3-D) network which is amorphous in nature. Thus, due to covalent bonding, CMPs show high thermal stability. In this thesis, CMPs have been designed and synthesized which have been studied for applications in energy storage and conversion devices, but before that it is important to have a critical view on their design, synthesis, properties.

4.1 Synthesis

CMP materials have synthetic flexibility which is advantageous over crystalline materials (COFs). In general, CMPs can be synthesized using C-C coupling, Schiff base condensation, amide coupling etc. Apart from this, the existence of a large library of nodes and linkers with a huge distribution of the functional groups is a boon to tune the properties of the material as per the requirements. Not only this, the variation in the reaction conditions such as temperature, solvents, time scale of the reaction and catalysts provide a good control of the reaction, resulting in numerous possibilities of tuning the porosity, morphology and subsequently the applications in resultant CMP. For the synthesis of CMPs a dynamic design strategy should be followed, the primary requirement of which is the need of the basic building blocks to have minimum of two reactive groups at the terminals.[132]

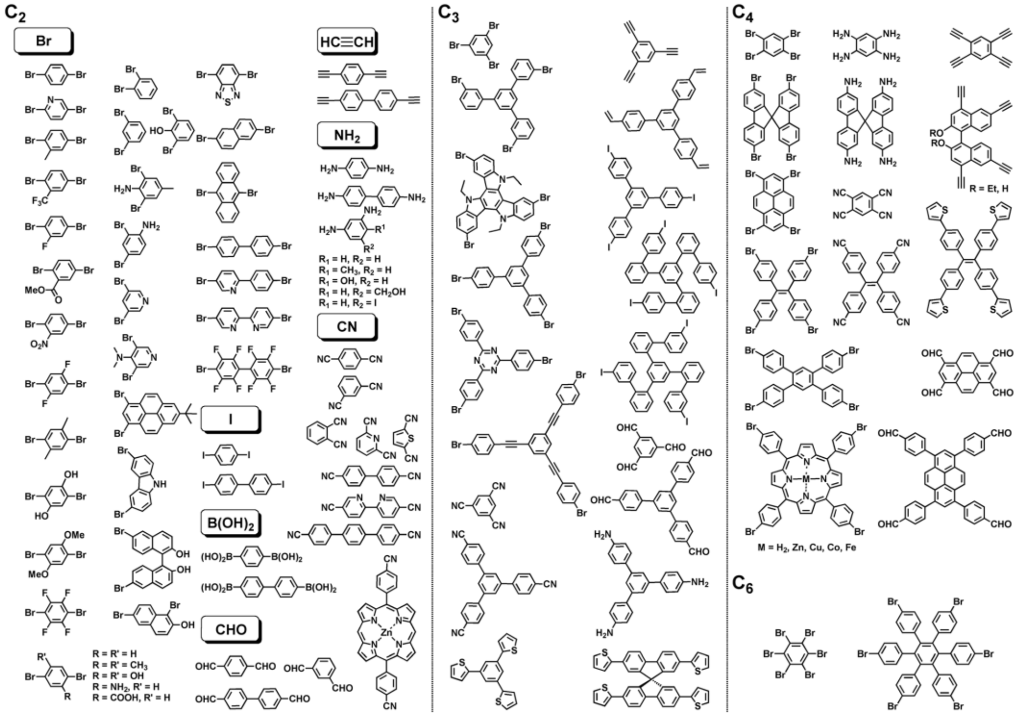

Figure 7: Library of linkers that can be used to synthesize CMPs and their symmetry. Reprinted with permissions from ref. no. 132.

The formation of CMPs with intrinsic and permanent porosity is the result of the formation of covalent bonds between C_2+C_3, C_2+C_4, C_2+C_6 or C_3+C_4, C_3+C_6 and C_4+C_6. Also, combination of three monomers of C_2 symmetry, two monomers of C_3 or C_4 symmetry also lead to the formation of CMPs. Figure 7 shows a large variety of linkers or nodes with different end group functionalities which have been used to synthesize a library of CMPs with different functionalities in the resulting polymer. These building blocks should be linked as per the strategy above with a π-conjugated bond. Suzuki cross coupling reaction, Yamamoto reaction, Sonogashira-Hogihara reaction, oxidative coupling reaction, Friedel-Craft reaction, phenazine ring formation, Schiff base condensation and cyclotrimerization reaction are some of the most common reactions used for the synthesis of CMPs (Figure 8).[132] This shows the use of easy synthetic methods to synthesize CMPs. Moreover, CMPs are the kinetically controlled products, so their synthesis requires very less reaction time as compared to the formation of their crystalline counter parts such as covalent organic frameworks. CMPs can easily be characterized with the help of modern techniques such as infrared (FT-IR) and ^{13}C solid state NMR spectroscopies along with imaging techniques such as field emission scanning electron microscopy (FESEM) or transmission electron microscopy (TEM). On the other hand, porous nature of the framework provide variety of applications such as in organic electronics,[133] photocatalysis,[134, 135] energy storage[136] etc. With these fascinating applications and other advantages discussed above, CMPs hold a large possibility of commercialization in near future.

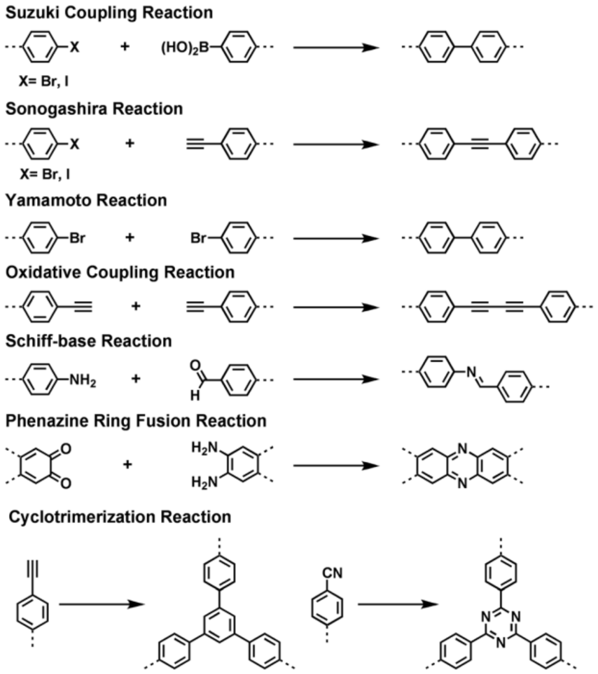

Figure 8: Schematic showing different reactions that can be used to synthesize CMPs. Reprinted with permissions from ref. no. 132.

4.2 Applications

Long back, CMPs were studied widely for their applications in gas storage and separation,[137] and heterogeneous catalysis[138, 139] due to their porous nature. In one of the reports, Liao *et al*. synthesized nitrogen rich conjugated microporous polymers (NCMPs) which were synthesized by chemical oxidative polymerization between multiconnected aniline precursors.[139] It was shown that NCMPs were effective at storage of CO_2, I_2 and H_2. Apart from this, NCMPs were also showed selectivity towards CO_2 over N_2 at ambient pressure. As nitrogen in NCMPs act as a binding site to coordinate metal ions, NCMPs are shown to be a support for $PdCl_2$ catalyst which was used for Suzuki-Miyaura coupling reaction under mild conditions and aqueous reaction medium with high recyclability with the retention of more than 94% of activity after six continuous cycles.[139] Apart from this, Roy *et al*. designed and synthesized a novel redox-active donor acceptor CMP which was found to be active for oxygen reduction reaction (ORR) and is one of the metal free TPA containing polymers.[42] In an another report, Bhattacharyya *et al*. has also designed and synthesized redox-active donor acceptor consisting of tris-(4-aminophenyl)amine (TPA**)** and perylenediimide (PDI) as the node and linker respectively. The presence of nitrogen centre helped for in-situ stabilization Co and Au nanoparticles. The metal free CMP TPA-PDI showed good ORR activity which improved upon Co doping. This was supported by DFT calculations. Moreover, upon doping of Au nanoparticles CMP was used for organocatalysis. Moreover, the recyclability was checked for three cycles and no decrease in activity was observed.[140] This proved that CMPs are one of the best matrices for the heterogeneous catalysis, metal ion or metal nanoparticles stabilization which are highly efficient due to their roboust structure and high porosity. Apart from the gas storage, separation and heterogeneous catalysis, CMPs are also widely studied for sensing applications, light harvesting materials, organic light emitting diodes[133, 141] and photocatalysis. On the other hand, donor acceptor approach is also widely used in various energy storage devices such as supercapacitors.[142-145] Therefore the above discussion indicates that the donor acceptor approach is one of the powerful approaches used in CMPs to get versatile applications.

4.3 Applications in Fuel Cells and Water Electrolysis

In this materialistic world, the need and consumption of energy is increasing at an alarming rate and still, the major sources for energy are non renewable sources such as fossil fuels. But now, it is need of the hour to develop low cost, environment friendly and durable energy conversion and storage devices. For this, till date, electrochemical energy is found out to be a cleanest and most efficient source. Major advances include the development of fuel cells, water electrolyzers, supercapacitors, batteries etc and these have their fundamentals in utilizing the electrochemical reactions such as oxygen reduction reaction (ORR), oxygen evolution reaction (OER) and hydrogen evolution reaction (HER). So, for the effective implementation, development of an efficient, stable and cost effective catalyst is the major concern. Nowadays, various attempts are being made to use the electrochemical energy to power electric vehicles (EVs). As a first step towards the goal was the development of Toyota Mirai car which works on the fuel cell technology and releases water as the exhaust waste.[146] But the use of expensive Pt based catalysts as cathode has increased the cost by many folds. Recently, another EV is developed which runs using water, metal and air as the fuel and is claimed to be a zero emission vehicle. But there is still a long way to go. For this, the material needs to be systematically designed to get the maximum efficiency. Using metal free or non noble metal based porous materials, having high electrochemical accessible area as the catalyst would be a good strategy to start with. The developments of advanced techniques have helped a lot for the development of the desired materials. Many materials have been developed which have not only been shown as the monofunctional catalysts but also bifunctional catalysts and a very as few trifunctional catalysts for ORR, OER and HER. For the development of such catalysts, it is important to know more about these reactions.

4.3.1 Oxygen Reduction Reaction (ORR)

Fuel cells are one of the major upcoming sources of the renewable electrochemical source of energy in which the chemical energy is directly converted to electrical energy. Unlike batteries, fuel cells do not require any energy for charging purpose. Instead, it works indefinitely as long as there is continuous supply of the raw materials. Various types of fuel cells have been developed such as molten carbonate fuel cells (MCFC), solid oxide fuel cells (SOFC), phosphoric acid fuel cells (PAFC) etc. The development of proton exchange membrane fuel cells (PEMFCs) has made the use of fuel cells possible as the current power source at the commercial level. This is due to low weight, volume, operating temperature, use of solid electrolyte as proton exchange membrane and high power density as compared to other types of fuel cells. PEMFCs are being used as power sources in various applications such as EVs and provide a step forward to solve the global energy problem.

PEMFC uses H_2 and O_2 gasses as the fuels. At anode, hydrogen oxidation reaction (HOR) ($H_2 \rightarrow 2H^+ + 2e^-$) takes place in which H_2 is oxidized to protons. The electrons are passed through the external circuit and protons pass through the proton exchange membrane to the cathode. At cathode oxygen reduction reaction (ORR) takes place using the electrons from the anode. The reduced oxygen then combines with the proton and thus giving out water as the by product. But the bottle neck in commercializing these fuel cells at much lower cost lies in ORR which is a very sluggish reaction and requires the use of expensive noble metal based catalysts. Moreover, ORR can proceed through either two electron process (with the formation of H_2O_2 followed by H_2O) or through four electron process (involving the direct conversion to H_2O with insignificant production of H_2O_2). Mostly, four electron process is the favored process for the application in fuel cells. So, the development of efficient cathode materials possessing low onset potential, high current density and good stability would be worth to work upon.

4.3.1.1 ORR Mechanism

ORR has sluggish reaction kinetics in which molecular oxygen is converted to two atoms of oxygen ($O_2 \rightarrow 2O \quad \Delta H = 498\ kJ/mol$). So, for higher current density and improved efficiency of the catalyst, this barrier should overcome with the minimum amount of energy (i.e the overpotential). The mechanism of ORR is complicated and can proceed through different pathways depending upon the electrolyte and the catalyst. It can follow with two electron transfer pathway with the production of hydrogen peroxide or four electron transfer pathway with direct conversion to water.[147]

(a) Two electron process

In acidic solution:

$$O_2 + 2H^+ + 2e^- \rightarrow H_2O_2 \qquad E_0 = 0.70\ V$$

$$H_2O_2 + 2H^+ + 2e^- \rightarrow 2H_2O \qquad E_0 = 1.76\ V$$

In alkaline solution:

$$O_2 + H_2O + 2e^- \rightarrow HO_2^- + OH^- \quad E_0 = -0.065\,V$$

$$HO_2^- + H_2O + 2e^- \rightarrow 3OH^- \quad E_0 = 0.867\,V$$

(b) Four electron process

In acidic solution:

$$O_2 + 4H^+ + 4e^- \rightarrow H_2O \quad E_0 = 1.229\,V$$

In basic solution:

$$O_2 + H_2O + 4e^- \rightarrow 4OH^- \quad E_0 = 0.401\,V$$

So ORR can be summarized as:

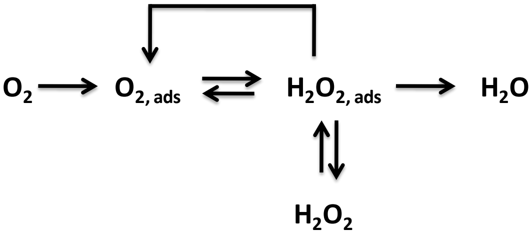

Figure 9: Schematic summarizing the ORR process.

4.3.2 Hydrogen Evolution Reaction (HER) & Oxygen Evolution Reaction (OER)

The electrolysis of water to H_2 and O_2 is one of the promising renewable energy sources which can be used in various energy consuming devices and can be used as the source for sustainable energy. Hydrogen gas which is produced as the product of above reaction is one of the cleanest source of fuel till date. Hydrogen possesses highest mass energy density as compared to other fuels and thus is viewed as the future fuel with promising applications. H_2 is widely used in industries such as petroleum refining, manufacturing of ammonia by Haber-Bosch process and so on. But, currently the hydrogen is being produced by the steam reforming process of coal which in turn releases large amount of carbon dioxide and various other gasses into the atmosphere and thus contributing to global warming. So, cheap, effective and green energy resources are required to produce hydrogen at large scale. This can be done by either photochemical pathway (i.e by using light as the source of energy and designing the catalyst that absorbs the light, preferably in visible region, and lowers the activation barrier to easily overcome the required energy) or by electrochemical water splitting (i.e applying the potential and thus overcoming the activation barrier). Latter pathway is one of the most exploited ways to fulfill the demand of hydrogen. Many Pt or Pt based noble metal catalysts are the state of materials for hydrogen evolution reaction (HER). But these being expensive cannot be used on daily basis. So, the development of cheap, porous and robust materials is needed to be designed and synthesized for efficient hydrogen production. Along with this, oxygen evolution reaction (OER) is the counter reaction that acts as a bottleneck for facile overall water splitting. OER involves the production of the molecular oxygen at the anode and is one the most energy greedy process along with slow kinetics. The thermodynamic potential for water oxidation reaction is 1.23 V where as for hydrogen evolution reaction, the potential is found out to be 0 V. So, for the overall water electrolysis, minimum potential of 1.23 V is required. Various oxide materials such as RuO_2, IrO_2 have been regarded as the state of art catalysts due to their low overpotential, high current density and high stability of oxides in basic medium. But less abundance of these oxides make them expensive catalysts and thus preventing their further use. So it is a necessity to develop a cheap, earth abundant catalyst for efficient water oxidation reaction. The operational voltage of a water electrolyzer depends upon the design of the electrolyzer and the kinetics of the anodic and cathodic reactions and thus the effects can be summarized as in the following equation:[148]

$$V_{op} = V_{eq} + \eta_A + |\eta_C| + \eta_\Omega$$

Where $V_{op} = operating\ voltage\ of\ the\ electrolyser,$

$V_{eq} = thermodynamic\ potential\ for\ water\ oxidation,$

η_A & $\eta_C = overpotentials\ for\ anodic\ \&\ cathodic\ reactions\ respectively,$

and $\eta_\Omega = overpotential\ required\ to\ overcome\ resistance\ losses.$

For an ideal catalyst, the anodic and cathodic overpotentials are zero. So the operating voltage directly depends upon the equilibrium potential required for overall water splitting and the resistance losses. These resistance losses can be minimized by the efficient design of the electrolyzer and thus reduce the operating potential of the electrolyzer for efficient generation of H_2 and O_2. Similar to ORR, water oxidation and proton reduction can also be carried out in both acidic and basic media and the reactions can be describes as follows:

In basic media:

$$(OER)\ 4OH^- \rightarrow O_2 + 2H_2O + 4e^-\ (V_A = 1.23\text{ V w.r.t. RHE})$$

$$(\text{HER})\ 4H_2O + 4e^- \rightarrow 2H_2 + 4OH^-\ (V_C = 0\text{ V w.r.t. RHE})$$

In acidic media:

$$(OER)\ 2H_2O \rightarrow O_2 + 4H^+ + 4e^-\ (V_A = 1.23\text{ V w.r.t. RHE})$$

$$(HER)\ 4H^+ + 4e^- \rightarrow 2H_2\ (V_C = 0\text{ V w.r.t. RHE})$$

4.3.2.1 HER Mechanism

Similar to ORR, HER can also take place in both acidic medium and alkaline medium. In acidic medium, H_3O^+ is the proton source which is reduced to H_2. Whereas, on the other hand, in alkaline medium, H_2O acts as the proton source resulting in the formation of H_2 gas. In acidic medium, the adsorption energy of the reactant on the catalyst surface is one of the key parameters to decide the conversion efficiency and the stability of the catalyst. Moderate adsorption energy of H^+ and H_2O provides low overpotential for the reaction to occur. Whereas in alkaline medium, a proper balance between the hydrogen adsorption, prevention of adsorption of OH^- and the energy required for water splitting is required for good efficiency. Also, high energy is required for the dissociation of water molecule to form proton and thus undergo HER. So HER reaction proceeds through three steps in alkaline medium, which include the adsorption of water onto the catalyst which is followed by the dissociation of water and thus resulting in the reactive intermediates. The adsorption step or the Volmer step can be represented as

$$2H_2O + S + 2e^- \rightarrow 2S - H_{ad} + 2OH^-$$

Where S represents the catalyst surface.

This can be followed by any one of the two recombination steps which can be represented as

$$Heyrovsky\ step: H_2O + e^- + H^* \rightarrow H_2 + OH^-$$

$$Tafel\ step: H^* + H^* \rightarrow H_2$$

Volmer step includes the adsorption of the reactive species on the catalyst surface. So, this is the mandatory step that will take place. Further to find out the rate determining step in HER, tafel slop is of great help. If the Tafel slope is found out to be 30 mV/dec, Tafel step is the rate determining step. On the other hand, Tafel slope of 40 mV/dec shows that the reaction proceeds through Heyrovsky mechanism and thus this would be the rate determining step.

Apart from this, Tafel slope of 120 mV/dec shows Volmer step to be the rate determining step and thus the reaction can proceed through any of the two recombination steps.[149]

In contrast to HER in alkaline medium, the reaction proceeds much easily in the acidic medium. This is due to the high energy required to break the covalent bond during water dissociation in alkaline medium. Whereas, in acidic medium, very weak dative bond in H_3O^+ has to be cleaved for the formation of a proton and thus very less energy is required. In acidic medium also, HER proceeds through the similar steps as in the alkaline medium, but the set of reactions that occur are as follows:[150]

1) $H^+ + cat + e^- \rightarrow cat - H^* \quad (Volmer\ reaction, Tafel\ slope = 120\, mV/dec)$

2) $cat - H^* + e^- \rightarrow M + H_2 \quad (Heyrovsky\ reaction, Tafel\ slope = 40\ mV/dec)$

3) $2[cat - H^*] \rightarrow 2M + H_2 \quad (Tafel\ reaction, Tafel\ slope = 30\ mV/dec)$

Similar to ORR, many non-noble metal or metal free systems have been developed that are highly efficient towards HER. The library of the catalyst include various metal oxides,[151, 152] 2-D nanomaterials,[153, 154] MOF derived porous materials, organic polymers such as CMPs[155, 156] etc.

4.3.2.2 OER Mechanism

For the development of an efficient catalyst, good knowledge about the mechanism of the reaction is necessary. OER is generally dependent on the surface sites, the nature of the electrolyte, i.e acidic or alkaline, etc. OER follows different mechanisms in acidic and alkaline media.

In acidic medium[157]:

$$S + H_2O \rightarrow S - OH + H^+ + e^-$$
$$S + OH \rightarrow S - O + H^+ + e^-$$
$$2[S - O] \rightarrow 2S + O_2$$

Where S = surface of the catalyst.

In basic medium:[158]

$$S + OH^- \rightarrow S - OH + e^-$$
$$S - OH + OH^- \rightarrow S - O + H_2O + e^-$$
$$2\,[S - O] \rightarrow O_2 + S$$

The polarization curve can lead to the tafel plot which inturn gives the tafel slope, exchange current density and thus helps to understand the kinetics of the reaction. To overcome the large energy barrier for OER with low overpotentials, many metal free or non nobel metal containing catalysts have been developed, those include various oxides,[159-161] nanomaterials,[162, 163], MOF derived materials, metal doped porous organic polymers, covalent organic frameworks[164], and many more.

4.4 Bifunctional Catalysts for ORR and OER

Various monofunctional catalysts have been developed till today, but the development of bifunctional is still the topic of research because of the need in various renerwable energy storage and conversion devices such as metal-air batteries, regenerative fuel cells etc. ORR is the main reaction occurring on the cathode of fuel cells and metal-air batteries during the discharge process. Opposite to this, OER occurs at the anode of the water electrolyser and is also used to electrically recharge the metal-air batteries (*vide infra*). So, it is important to develop a stable bifunctional electrocatalyst for the efficient working of metal-air batteries. Till date, Pt/C is regarded as the state of catalyst for ORR. But this being highly expensive and cannot be commercialized. Moreover, Pt/C is found to be inactive for OER due to the formation of oxide on the surface and thus prevents its use in many of the applications. Oxides such as RuO_2 or IrO_2 are known to be the state of art catalyst for OER. But these also being highly expensive, their scarcity and inefficiency towards ORR prevents their wide commercialization. So, it is need of the hour to develop efficient, stable, non noble metal based electrocatalysts which reduce the activation barrier for these reactions to a large extent and thus require low overpotentials for the reaction to proceed and obtain the desired current density. Various transition metal oxides, hydroxides, sulphides, carbon materials and composites are shown to be bifunctional towards ORR and OER. However, MOF derived materials and organic porous materials (with metal encapsulation) possessing bifunctionality are still rare.[165] Many MOF derived electrocatalysts are being reported which form nanostructures along with periodic doping of heteroatoms such as N, P, S, B etc. These heteroatoms being more electronegative in nature than carbon pull the electrons towards itself and thus making the carbon electron deficient. This promotes the adsorption of oxygen on the formed nanostructures and is thus found to be bifunctional electrocatalyst showing both ORR and OER activities. Li *et al*. found out the roles of different types of N obtained upon carbonization of MOF. It was found out that quaternary N was responsible for the current density, whereas pyridinic N was responsible for the onset potential.[166] Encapsulation of transition metal in between the graphene layers or carbon nanotubes is found to show both ORR and OER with good activities and stability. Recently Li *et al*. encapsulated Co nanoparticles in nitrogen doped graphene shells which was found to be active towards ORR and HER.[167] Whereas, Kim *et al*. synthesized nanomaterial which consists of nanocactus shaped Co_3O_4 grown onto the carbon nanotubes. This showed efficient electrocatalytic activity towards ORR and OER with the small potential difference of 0.72 V between the onset for OER and $E_{1/2}$ for ORR.[168] Further, core-shell $Co@Co_3O_4$ encapsulated in NCNT was derived by the pyrolysis of MOF explained the synergistic effect of core-shell structure on the electrocatalytic activity towards ORR and OER.[169] The catalyst showed the reversible overvoltage of only 0.85 V which even surpasses that of state of art catalysts such as Pt/C, IrO_2 and RuO_2. Further, $Fe/Fe_3C@C$ (Fe@C) nanoparticles were doped the combination of N doped graphene and CNT. The detailed experiments were carried out to find the reason for ORR and OER activity. It was shown that Fe@C provides the electrons to the carbon core, thus promoting ORR activity. Whereas Fe@C nanoparticles and N doped species were found to be responsible for high OER activity. Moreover, MOF derived metal free bifunctional electrocatalysts have also been developed.[170]

Moreover, the development of trifunctional catalyst is a boon for the advancement in many energy storage and conversion devices such as regenerative fuel cells. In regenerative fuel cells, hydrogen and oxygen are used as the fuels and thus the chemical energy is converted to electrical energy. The two main reactions that take place include oxygen reduction reaction and hydrogen oxidation reaction (HOR) with the emission of water as the byproduct. The hydrogen and oxygen consumed during this process are generated cathode and anode respectively of the water electrolyser. Water oxidation reaction (i.e OER) takes place at the anode while the proton reduction reaction (i.e HER) takes place on the cathode. So, as of now, the electrodes in regenerative fuel cell requires different catalysts for ORR, OER, HOR and HER. Pt/C is a very well known and efficient catalyst for HOR and requires very less amount of loading for sufficient conversion. But ORR, OER and HER are the bottle neck reactions. So, using different state of art catalyst for three processes makes the commercializing of regenerative fuel cells very difficult as well as cost greedy process. To overcome this problem, the development of a cost effective, efficient, stable and non noble metal based trifunctional catalyst would be a revolutionary development not only in the field of regenerative fuel cells but in many other devices in general. Till date, only countable number of trifunctional catalyst possessing ORR, OER as well as HER are reported. Following the same strategy of heteroatom doping, a trifuntional electrocatalyst can also be developed as shown by Dai *et al*. by doping graphene with nitrogen, phosphorus and fluorine. This was obtained by thermal activation of mixture of ammonium hexafluorophosphate and polyaniline coated on graphene oxide at 950 ^{o}C for 1 hour. Uniform distribution of the heteroatom on graphene was found thus, this changed the surface properties of graphene, hence improving its electrocatalytic activity.[171]

5 Zinc-Air Battery

The continuous use of fossil fuels is having very deteriorating effect on the global atmosphere. As a solution the world is moving towards using the sustainable energy harvesting, conversion and storage systems. One of them is batteries which convert and store electrical energy. Various types of batteries have been developed, the most extensively used of which include the Li-ion batteries. High power and energy density of Li-ion batteries lead to the fast commercialization in the global market making it the promising energy source. From the past few years, the development of electrical vehicles (EVs), from hybrid vehicles to plug-in followed by pure EVs has gained lot of attention and advancement. Recently, Tesla Model S EV was developed which used Li-ion battery as the power source. But Li-ion batteries suffer from many disadvantages, starting from the lack of Li in earth crust and all the way to safety issues. So now-a-days, post Li-ion batteries are being worked upon, the most common of which are the metal-air batteries. Metal-air batteries use the metal as the anode (negative electrode), and the air breathing electrode as the cathode. So unlike Li-ion batteries, metal-air batteries lie between the traditional batteries, which use metal as anode, and fuel cells which require porous electrodes and continuous supply of O_2 from the surrounding atmosphere. The most common metal which is which is being used as anode in metal-air batteries is zinc, because of its low cost and spontaneous chemistry with oxygen. Zn-air batteries have high theoretical energy density of 1086 Wh/kg (including oxygen) which is almost 5 times less than the Li-ion batteries. Moreover, zinc metal being abundant, much cheaper than Li reduces the overall cost of the battery.

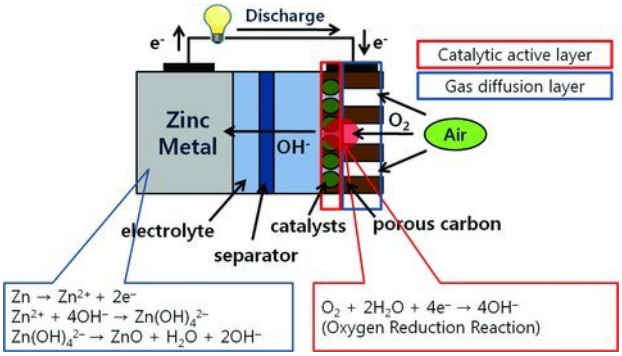

Figure 10: Schematic showing the Zn-air battery scheme & design of the cathode along with the reactions involved at anode & cathode. Reprinted with permissions from ref. no. 172.

The primary Zn-air battery consists of Zn electrode as anode, the air electrode (with catalyst coated) as the cathode along with the separator between the two electrodes (Figure 10).[172] The aqueous alkaline electrolyte is generally used. At the negative electrode, the oxidation of Zn takes place and thus converting Zn to zincate ions [$Zn(OH)_4^{2-}$] which are soluble in the electrolyte. On supersaturation, zincate ions are decomposed to form insoluble ZnO. On the other hand, the positive electrode is the gas diffusion layer (GDL) with the coating of the catalyst. Oxygen gas from the atmosphere passes through the GDL which is reduced at surface of the catalyst and thus ORR takes place. So, for the primary battery, ORR active catalyst is used as the cathode.[124]

$$(Negative\ electrode)\quad Zn + 4OH^- \rightarrow Zn(OH)_4^{2-} + 2e^-$$

$$Zn(OH)_4^{2-} \rightarrow ZnO + H_2O + 2OH^-$$

$$(Positive\ electrode)\quad O_2 + 4e^- + 2H_2O \rightarrow 4OH^-$$

$$(Overall\ reaction)\quad 2Zn + O_2 \rightarrow 2ZnO$$

To build a secondary battery that can be recharged requires all the opposite reactions to occur. The soluble zincate ions are converted back to zinc metal. But the solubility of the zincate ions leads to less cycling stability on repetitive charge and discharge. Furthermore, the opposite reaction of ORR, i.e OER should occur at the air cathode. So for an electrically rechargeable battery, the catalyst on air cathode should possess bifunctionality in nature which is capable of both ORR and OER. So, various bifunctional electrocatalysts are developed which are active for both ORR and OER and are thus used as the cathode material for electrically rechargeable battery. Flexible and wearable electronics is trending these days and as the name suggests, they deliver the same function even on mechanical deformation. So, for the development of flexible electronics, flexible energy storage devices are also required. These can be obtained by using flexible electrodes along with the gel electrolyte to prevent its leakage under stressed conditions. For Zn-air batteries, generally polyvinyl alcohol (PVA) gel electrolyte is used along with KOH. Here, this gel serves both as the electrolyte as well as the separator to differentiate the two electrodes. The PVA gel consists of both micro and nano sized pores that can accommodate the electrolyte through the capillary action and thus transport hydroxyl ions in a quasi-solid state by the cross linking process.[173] Many Zn-air batteries have been developed but only few flexible batteries have been developed and even few knittable batteries have been developed till date. As discussed, the requirement for the primary battery is ORR which is used for discharging the battery and opposite reaction, OER is required to electrically recharge the battery. So, recently, Co-N-C active sites were confined in B, N co-doped carbon nanosheets by Mu *et al*. in which the presence of an electron deficient B lowers the oxygen reaction activation barriers and thus making the material bifunctional in nature. The materials when used as the cathode in Zn-air batteries possessed high OCP of 1.43 V with the peak power density of 100.4 mW/cm^2. Further a flexible battery was also prepared with PVA gel as the electrolyte, which also showed good cyclic performance. Zn-air batteries can also be converted to fully flexible batteries as shown by Yang *et al*., in which the zinc was electrodeposited on the flexible conducting carbon cloth and was used as the anode material along with N-doped Co_3O_4 mesoporous nanowires as the cathode.[174] Further, Li *et al*. showed the development of a cable type Zn-air battery which used zinc wire as the anode along with the gel electrolyte and $NiCo_2O_4$@N-OCNT films as bifunctional catalysts as the cathode material.

Outlook

With modernization, the need of energy is rising at a fast pace and so does the need of renewable & efficient energy storage and conversion systems. Extensive research has lead to the development and commercialization of various energy storage systems such as Li-ion batteries. But lesser number of pros than cons has shifted the interest of researchers towards other sustainable systems. Careful tailoring of the porous materials can lead to multiple properties in a single system. The application of electrochromic and photochromic materials in smart windows have taken the human comfort one step forward. Also, the application in smart windows provide a good opportunity to store the solar energy. To exploit this solar energy, a trifunctional material possessing photochoromism, electrochromism along with energy storage is required, but these are still rare. NMOF being solution processable is carefully designed to possess all the desired properties in a single system. Moreover, the variety of ligands used in MOFs can lead to interesting MOF derived heteroatom doped nanostructures which have been found to be efficient energy conversion and energy storage system. Electrically rechargeable Zn-air batteries require bifunctional materials capable of ORR and OER, whereas electrolysis of water requires a material active for OER and HER. But the development of materials that can be used in Zn-air batteries as well as water electrolysis is still underexplored. For this, MOF derived core-shell wrapped in NCNT is exploited. Further, taking a step closer to organic materials, trifunctional redox active donor-acceptor conjugated microporous materials were carefully designed which were used as a cathode material for Zn-air battery and as both anode and cathode for water electrolysis which was powered by the fabricated Zn-air battery and thus showing self powered overall water splitting. It is believed that the approach followed in designing the materials will lead to the development of new multifunctional materials which will be useful for energy and environment applications.

6. References

1. M. Tahir, L. Pan, F. Idrees, X. Zhang, L. Wang, J.-J. Zou and Z. L. Wang, *Nano Energy*, 2017, **37**, 136.
2. A. H. Lu and F. Schüth, *Adv. Mater.*, 2006, **18**, 1793.
3. M.-H. Sun, S.-Z. Huang, L.-H. Chen, Y. Li, X.-Y. Yang, Z.-Y. Yuan and B.-L. Su, *Chem. Soc. Rev.*, 2016, **45**, 3479.
4. J. Jiang, J. Yu and A. Corma, *Angew. Chem. Int. Ed.*, 2010, **49**, 3120.
5. O. M. Yaghi and H. Li, *J. Am. Chem. Soc.*, 1995, **117**, 10401.
6. D. M. Young, U. Geiser, A. J. Schultz and H. H. Wang, *J. Am. Chem. Soc.*, 1998, **120**, 1331.
7. A. Chakraborty, S. Bhattacharyya, A. Hazra, A. C. Ghosh and T. K. Maji, *Chem. Commun.*, 2016, **52**, 2831.
8. A. Hazra, S. Bonakala, K. K. Bejagam, S. Balasubramanian and T. K. Maji, *Chem. Eur. J.*, 2016, **22**, 7792.
9. J. A. Mason, J. Oktawiec, M. K. Taylor, M. R. Hudson, J. Rodriguez, J. E. Bachman, M. I. Gonzalez, A. Cervellino, A. Guagliardi, C. M. Brown, P. L. Llewellyn, N. Masciocchi and J. R. Long, *Nature*, 2015, **527**, 357.
10. A. Kertik, L. H. Wee, M. Pfannmöller, S. Bals, J. A. Martens and I. F. J. Vankelecom, *Energy Environ. Sci.*, 2017, **10**, 2342.
11. M. Matsumoto and T. Kitaoka, *Adv. Mater.*, 2016, **28**, 1765.
12. H. Li, K. Wang, Y. Sun, C. T. Lollar, J. Li and H.-C. Zhou, *Mater. Today*, 2018, **21**, 108.
13. D.-X. Xue, Q. Wang and J. Bai, *Coord. Chem. Rev.*, 2019, **378**, 2.
14. P. García-Holley, B. Schweitzer, T. Islamoglu, Y. Liu, L. Lin, S. Rodriguez, M. H. Weston, J. T. Hupp, D. A. Gómez-Gualdrón, T. Yildirim and O. K. Farha, *ACS Energy Lett.*, 2018, **3**, 748.
15. D. Banerjee, C. M. Simon, S. K. Elsaidi, M. Haranczyk and P. K. Thallapally, *Chem*, 2018, **4**, 466.
16. L. Jiao, Y. Wang, H.-L. Jiang and Q. Xu, *Adv. Mater.*, 2018, **30**, 1703663.
17. L. Zhu, X.-Q. Liu, H.-L. Jiang and L.-B. Sun, *Chem. Rev.*, 2017, **117**, 8129.

18. S. M. J. Rogge, A. Bavykina, J. Hajek, H. Garcia, A. I. Olivos-Suarez, A. Sepúlveda-Escribano, A. Vimont, G. Clet, P. Bazin, F. Kapteijn, M. Daturi, E. V. Ramos-Fernandez, F. X. Llabrés i Xamena, V. Van Speybroeck and J. Gascon, *Chem. Soc. Rev.*, 2017, **46**, 3134.
19. A. Dhakshinamoorthy, A. M. Asiri and H. Garcia, *Chem. Soc. Rev.*, 2015, **44**, 1922.
20. M. Kurmoo, *Chem. Soc. Rev.*, 2009, **38**, 1353.
21. B.-W. Qin, K.-C. Huang, Y. Zhang, L. Zhou, Z. Cui, K. Zhang, X.-Y. Zhang and J.-P. Zhang, *Chem. Eur. J.*, 2018, **24**, 1962.
22. G. Lu and J. T. Hupp, *J. Am. Chem. Soc.*, 2010, **132**, 7832.
23. L. E. Kreno, K. Leong, O. K. Farha, M. Allendorf, R. P. Van Duyne and J. T. Hupp, *Chem. Rev.*, 2012, **112**, 1105.
24. Z. Hu, B. J. Deibert and J. Li, *Chem. Soc. Rev.*, 2014, **43**, 5815.
25. J. Della Rocca, D. Liu and W. Lin, *Acc. Chem. Res.*, 2011, **44**, 957.
26. L. Wang, M. Zheng and Z. Xie, *J. Mater. Chem. B*, 2018, **6**, 707.
27. D. Samanta, S. Roy, R. Sasmal, N. D. Saha, P. K R, R. Viswanatha, S. S. Agasti and T. K. Maji, *Angew. Chem. Int. Ed.*, 2019, **0**.
28. Y. Liu, W. Hou, L. Xia, C. Cui, S. Wan, Y. Jiang, Y. Yang, Q. Wu, L. Qiu and W. Tan, *Chem. Sci.*, 2018, **9**, 7505.
29. Y. Yu, L. Lan and H. Cai, *J. Phys. Chem. C*, 2018, **122**, 96.
30. A. Carné, C. Carbonell, I. Imaz and D. Maspoch, *Chem. Soc. Rev.*, 2011, **40**, 291.
31. Y. Li, Y. Xu, W. Yang, W. Shen, H. Xue and H. Pang, *Small*, 2018, **14**, 1704435.
32. C. Yu, Y. Wang, J. Cui, D. Yu, X. Zhang, X. Shu, J. Zhang, Y. Zhang, R. Vajtai, Pulickel M. Ajayan and Y. Wu, *J. Mater. Chem. A*, 2018, **6**, 8396.
33. R. Wang, X.-Y. Dong, J. Du, J.-Y. Zhao and S.-Q. Zang, *Adv. Mater.*, 2018, **30**, 1703711.
34. S. Yang, L. Peng, E. Oveisi, S. Bulut, D. T. Sun, M. Asgari, O. Trukhina and W. L. Queen, *Chem. Eur. J.*, 2018, **24**, 4234.
35. G. Anandhababu, Y. Huang, D. D. Babu, M. Wu and Y. Wang, *Adv. Funct. Mater.*, 2018, **28**, 1706120.
36. R. Tang, S. Zhou, L. Zhang and L. Yin, *Adv. Funct. Mater.*, 2018, **28**, 1706154.

37. A. Jayakumar, R. P. Antony, J. Zhao and J.-M. Lee, *Electrochim. Acta*, 2018, **265**, 336.
38. R. V. Jagadeesh, K. Murugesan, A. S. Alshammari, H. Neumann, M.-M. Pohl, J. Radnik and M. Beller, *Science*, 2017, **358**, 326.
39. Y.-Z. Chen, R. Zhang, L. Jiao and H.-L. Jiang, *Coord. Chem. Rev.*, 2018, **362**, 1.
40. A. I. Cooper, *Adv. Mater.*, 2009, **21**, 1291.
41. L. Qin, G.-j. Xu, C. Yao and Y.-h. Xu, *Chem. Commun.*, 2016, **52**, 12602.
42. S. Roy, A. Bandyopadhyay, M. Das, P. P. Ray, S. K. Pati and T. K. Maji, *Journal of Materials Chemistry A*, 2018, **6**, 5587.
43. W. Lu, D. Yuan, D. Zhao, C. I. Schilling, O. Plietzsch, T. Muller, S. Bräse, J. Guenther, J. Blümel, R. Krishna, Z. Li and H.-C. Zhou, *Chem. Mater.*, 2010, **22**, 5964.
44. Q. Chen, D.-P. Liu, M. Luo, L.-J. Feng, Y.-C. Zhao and B.-H. Han, *Small*, 2014, **10**, 308.
45. P. Lindemann, M. Tsotsalas, S. Shishatskiy, V. Abetz, P. Krolla-Sidenstein, C. Azucena, L. Monnereau, A. Beyer, A. Gölzhäuser, V. Mugnaini, H. Gliemann, S. Bräse and C. Wöll, *Chem. Mater.*, 2014, **26**, 7189.
46. P. Ju, S. Wu, Q. Su, X. Li, Z. Liu, G. Li and Q. Wu, *J. Mater. Chem. A*, 2019, **7**, 2660.
47. M. Liu, B. Zhou, L. Zhou, Z. Xie, S. Li and L. Chen, *J. Mater. Chem. A*, 2018, **6**, 9860.
48. Y.-B. Zhou and Z.-P. Zhan, *Chemistry – An Asian Journal*, 2018, **13**, 9.
49. C. Zhang, Y. Qiao, P. Xiong, W. Ma, P. Bai, X. Wang, Q. Li, J. Zhao, Y. Xu, Y. Chen, J. H. Zeng, F. Wang, Y. Xu and J.-X. Jiang, *ACS Nano*, 2019, **13**, 745.
50. A. M. Khattak, H. Sin, Z. A. Ghazi, X. He, B. Liang, N. A. Khan, H. R. Alanagh, A. Iqbal, L. Li and Z. Tang, *J. Mater. Chem. A*, 2018, **6**, 18827.
51. S. Kitagawa, R. Kitaura and S.-i. Noro, *Angew. Chem. Int. Ed.*, 2004, **43**, 2334.
52. A. N. Khlobystov, A. J. Blake, N. R. Champness, D. A. Lemenovskii, A. G. Majouga, N. V. Zyk and M. Schröder, *Coord. Chem. Rev.*, 2001, **222**, 155.
53. M. Klimakow, P. Klobes, A. F. Thünemann, K. Rademann and F. Emmerling, *Chem. Mater.*, 2010, **22**, 5216.

54. A. Martinez Joaristi, J. Juan-Alcañiz, P. Serra-Crespo, F. Kapteijn and J. Gascon, *Cryst. Growth Des.*, 2012, **12**, 3489.

55. I. Thomas-Hillman, A. Laybourn, C. Dodds and S. W. Kingman, *J. Mater. Chem. A*, 2018, **6**, 11564.

56. S. M. Moosavi, A. Chidambaram, L. Talirz, M. Haranczyk, K. C. Stylianou and B. Smit, *Nat. Commun.*, 2019, **10**, 539.

57. C. Pettinari, F. Marchetti, N. Mosca, G. Tosi and A. Drozdov, *Polym. Int.*, 2017, **66**, 731.

58. E. A. Flügel, A. Ranft, F. Haase and B. V. Lotsch, *J. Mater. Chem.*, 2012, **22**, 10119.

59. L. E. Kreno, J. T. Hupp and R. P. Van Duyne, *Anal. Chem.*, 2010, **82**, 8042.

60. J. Liu, F. Sun, F. Zhang, Z. Wang, R. Zhang, C. Wang and S. Qiu, *J. Mater. Chem.*, 2011, **21**, 3775.

61. X. Zhang, M. A. Ballem, Z.-J. Hu, P. Bergman and K. Uvdal, *Angew. Chem. Int. Ed.*, 2011, **50**, 5729.

62. C. He, K. Lu and W. Lin, *J. Am. Chem. Soc.*, 2014, **136**, 12253.

63. A. Ray Chowdhuri, D. Bhattacharya and S. K. Sahu, *Dalton Trans.*, 2016, **45**, 2963.

64. J. Wang, J. D. Byrne, M. E. Napier and J. M. DeSimone, *Small*, 2011, **7**, 1919.

65. H. B. Na, I. C. Song and T. Hyeon, *Adv. Mater.*, 2009, **21**, 2133.

66. S. Furukawa, J. Reboul, S. Diring, K. Sumida and S. Kitagawa, *Chem. Soc. Rev.*, 2014, **43**, 5700.

67. G. Liang, J. Xu and X. Wang, *J. Am. Chem. Soc.*, 2009, **131**, 5378.

68. S. Vaucher, M. Li and S. Mann, *Angew. Chem. Int. Ed.*, 2000, **39**, 1793.

69. Z. Ni and R. I. Masel, *J. Am. Chem. Soc.*, 2006, **128**, 12394.

70. W.-J. Son, J. Kim, J. Kim and W.-S. Ahn, *Chem. Commun.*, 2008, DOI: 10.1039/B814740J, 6336.

71. N. Sikdar, M. Bhogra, Umesh V. Waghmare and T. K. Maji, *J. Mater. Chem. A*, 2017, **5**, 20959.

72. T. Tsuruoka, S. Furukawa, Y. Takashima, K. Yoshida, S. Isoda and S. Kitagawa, *Angew. Chem.*, 2009, **121**, 4833.

73. S. Jung and M. Oh, *Angew. Chem. Int. Ed.*, 2008, **47**, 2049.

74. W. J. Rieter, K. M. L. Taylor, H. An, W. Lin and W. Lin, *J. Am. Chem. Soc.*, 2006, **128**, 9024.

75. C. A. Kent, D. Liu, L. Ma, J. M. Papanikolas, T. J. Meyer and W. Lin, *J. Am. Chem. Soc.*, 2011, **133**, 12940.

76. V. M. Suresh, S. J. George and T. K. Maji, *Adv. Funct. Mater.*, 2013, **23**, 5585.

77. I. Imaz, D. Maspoch, C. Rodríguez-Blanco, J. M. Pérez-Falcón, J. Campo and D. Ruiz-Molina, *Angew. Chem. Int. Ed.*, 2008, **47**, 1857.

78. E. Hadjoudis and I. M. Mavridis, *Chem. Soc. Rev.*, 2004, **33**, 579.

79. H. Durr and H. B. Laurent, *Photochromism: Molecules and Systems*, Elsevier, 2003.

80. J. T. Foy, Q. Li, A. Goujon, J.-R. Colard-Itté, G. Fuks, E. Moulin, O. Schiffmann, D. Dattler, D. P. Funeriu and N. Giuseppone, *Nat. Nanotechnol.*, 2017, **12**, 540.

81. Y. Kamiya and H. Asanuma, *Acc. Chem. Res.*, 2014, **47**, 1663.

82. E. Orgiu and P. Samorì, *Adv. Mater.*, 2014, **26**, 1827.

83. Y. Wakayama, *Materials Nanoarchitectonics*, 2018, DOI: doi:10.1002/9783527808311.ch13.

84. Y. Ishiguro, R. Hayakawa, T. Yasuda, T. Chikyow and Y. Wakayama, *ACS Appl. Mater. Interfaces*, 2013, **5**, 9726.

85. M. Suda, R. Kato and H. M. Yamamoto, *Science*, 2015, **347**, 743.

86. L. Wang and Q. Li, *Chem. Soc. Rev.*, 2018, **47**, 1044.

87. J. Zhang, Q. Zou and H. Tian, *Adv. Mater.*, 2013, **25**, 378.

88. L. Wen, X. Hou, Y. Tian, F.-Q. Nie, Y. Song, J. Zhai and L. Jiang, *Adv. Mater.*, 2010, **22**, 1021.

89. K. Xiao, X.-Y. Kong, Z. Zhang, G. Xie, L. Wen and L. Jiang, *Journal of Photochemistry and Photobiology C: Photochemistry Reviews*, 2016, **26**, 31.

90. G. Xie, L. Wen and L. Jiang, *Nano Research*, 2016, **9**, 59.

91. J. Park, D. Feng, S. Yuan and H.-C. Zhou, *Angew. Chem.*, 2015, **127**, 440.

92. X.-D. Yang, C. Chen, Y.-J. Zhang, L.-X. Cai, B. Tan and J. Zhang, *Dalton Trans.*, 2016, **45**, 4522.

93. T. Murase, S. Sato and M. Fujita, *Angew. Chem. Int. Ed.*, 2007, **46**, 5133.

94. N. Yanai, T. Uemura, M. Inoue, R. Matsuda, T. Fukushima, M. Tsujimoto, S. Isoda and S. Kitagawa, *J. Am. Chem. Soc.*, 2012, **134**, 4501.

95. J. Park, D. Yuan, K. T. Pham, J.-R. Li, A. Yakovenko and H.-C. Zhou, *J. Am. Chem. Soc.*, 2012, **134**, 99.

96. J. W. Brown, B. L. Henderson, M. D. Kiesz, A. C. Whalley, W. Morris, S. Grunder, H. Deng, H. Furukawa, J. I. Zink, J. F. Stoddart and O. M. Yaghi, *Chem. Sci.*, 2013, **4**, 2858.

97. G. Granqvist Claes, *Journal*, 2008, **80**, 2489.

98. C. G. Granqvist, M. A. Arvizu, İ. Bayrak Pehlivan, H. Y. Qu, R. T. Wen and G. A. Niklasson, *Electrochim. Acta*, 2018, **259**, 1170.

99. S. Furukawa and J. Ashburne, *Chem*, 2016, **1**, 186.

100. J. Kim, G. K. Ong, Y. Wang, G. LeBlanc, T. E. Williams, T. M. Mattox, B. A. Helms and D. J. Milliron, *Nano Lett.*, 2015, **15**, 5574.

101. R. J. Mortimer, *Chem. Soc. Rev.*, 1997, **26**, 147.

102. N. Elool Dov, S. Shankar, D. Cohen, T. Bendikov, K. Rechav, L. J. W. Shimon, M. Lahav and M. E. van der Boom, *J. Am. Chem. Soc.*, 2017, **139**, 11471.

103. M. Lahav and M. E. van der Boom, *Adv. Mater.*, 2018, **30**, 1706641.

104. Y.-W. Zhong, *Electrochromic Materials and Devices*, 2013, DOI: doi:10.1002/9783527679850.ch6.

105. C. R. Wade, M. Li and M. Dincă, *Angew. Chem. Int. Ed.*, 2013, **52**, 13377.

106. C.-W. Kung, T. C. Wang, J. E. Mondloch, D. Fairen-Jimenez, D. M. Gardner, W. Bury, J. M. Klingsporn, J. C. Barnes, R. Van Duyne, J. F. Stoddart, M. R. Wasielewski, O. K. Farha and J. T. Hupp, *Chem. Mater.*, 2013, **25**, 5012.

107. Y.-X. Xie, W.-N. Zhao, G.-C. Li, P.-F. Liu and L. Han, *Inorg. Chem.*, 2016, **55**, 549.

108. T. Kyotani, T. Nagai, S. Inoue and A. Tomita, *Chem. Mater.*, 1997, **9**, 609.

109. H. Yang and D. Zhao, *J. Mater. Chem.*, 2005, **15**, 1217.

110. Z. Wu, P. A. Webley and D. Zhao, *J. Mater. Chem.*, 2012, **22**, 11379.

111. Y. Meng, D. Gu, F. Zhang, Y. Shi, H. Yang, Z. Li, C. Yu, B. Tu and D. Zhao, *Angew. Chem. Int. Ed.*, 2005, **44**, 7053.

112. Z. Xie, W. Xu, X. Cui and Y. Wang, *ChemSusChem*, 2017, **10**, 1645.

113. S. Dang, Q.-L. Zhu and Q. Xu, *Nature Reviews Materials*, 2017, **3**, 17075.

114. S. Gadipelli, W. Travis, W. Zhou and Z. Guo, *Energy Environ. Sci.*, 2014, **7**, 2232.

115. S. J. Yang, T. Kim, J. H. Im, Y. S. Kim, K. Lee, H. Jung and C. R. Park, *Chem. Mater.*, 2012, **24**, 464.

116. H.-L. Jiang, B. Liu, Y.-Q. Lan, K. Kuratani, T. Akita, H. Shioyama, F. Zong and Q. Xu, *J. Am. Chem. Soc.*, 2011, **133**, 11854.

117. R. Zhang, T. Zhou, L. Wang and T. Zhang, *ACS Appl. Mater. Interfaces*, 2018, **10**, 9765.

118. H. Yuan, S. A. A. A. Aljneibi, J. Yuan, Y. Wang, H. Liu, J. Fang, C. Tang, X. Yan, H. Cai, Y. Gu, S. J. Pennycook, J. Tao and D. Zhao, *Adv. Mater.*, 2019, **31**, 1807161.

119. W.-T. Koo, S.-J. Choi, S.-J. Kim, J.-S. Jang, H. L. Tuller and I.-D. Kim, *J. Am. Chem. Soc.*, 2016, **138**, 13431.

120. K. Jayaramulu, N. Kumar, A. Hazra, T. K. Maji and C. N. R. Rao, *Chem. Eur. J.*, 2013, **19**, 6966.

121. A. Indra, T. Song and U. Paik, *Adv. Mater.*, 2018, **30**, 1705146.

122. J. Lu, W. Zhou, L. Wang, J. Jia, Y. Ke, L. Yang, K. Zhou, X. Liu, Z. Tang, L. Li and S. Chen, *ACS Catal.*, 2016, **6**, 1045.

123. C. Vaalma, D. Buchholz, M. Weil and S. Passerini, *Nature Reviews Materials*, 2018, **3**, 18013.

124. Y. Li and H. Dai, *Chem. Soc. Rev.*, 2014, **43**, 5257.

125. J.-M. Fan, J.-J. Chen, Q. Zhang, B.-B. Chen, J. Zang, M.-S. Zheng and Q.-F. Dong, *ChemSusChem*, 2015, **8**, 1856.

126. Y. Wang, C. Wang, Y. Wang, H. Liu and Z. Huang, *J. Mater. Chem. A*, 2016, **4**, 5428.

127. T. Wang, Z. Kou, S. Mu, J. Liu, D. He, I. S. Amiinu, W. Meng, K. Zhou, Z. Luo, S. Chaemchuen and F. Verpoort, *Adv. Funct. Mater.*, 2018, **28**, 1705048.

128. Y.-J. Li, J.-M. Fan, M.-S. Zheng and Q.-F. Dong, *Energy Environ. Sci.*, 2016, **9**, 1998.

129. J. Xu, W. Zhang, Y. Chen, H. Fan, D. Su and G. Wang, *J. Mater. Chem. A*, 2018, **6**, 2797.

130. R. Bendi, V. Kumar, V. Bhavanasi, K. Parida and P. S. Lee, *Adv. Energy Mater.*, 2016, **6**, 1501833.

131. C. Qu, L. Zhang, W. Meng, Z. Liang, B. Zhu, D. Dang, S. Dai, B. Zhao, H. Tabassum, S. Gao, H. Zhang, W. Guo, R. Zhao, X. Huang, M. Liu and R. Zou, *J. Mater. Chem. A*, 2018, **6**, 4003.

132. Y. Xu, S. Jin, H. Xu, A. Nagai and D. Jiang, *Chem. Soc. Rev.*, 2013, **42**, 8012.

133. H. Bildirir, V. G. Gregoriou, A. Avgeropoulos, U. Scherf and C. L. Chochos, *Mater. Horizons*, 2017, **4**, 546.

134. L. Wang, Y. Zhang, L. Chen, H. Xu and Y. Xiong, *Adv. Mater.*, 2018, **30**, 1801955.

135. Catherine M. Aitchison, R. S. Sprick and A. I. Cooper, *J. Mater. Chem. A*, 2019, **7**, 2490.

136. F. Xu, X. Chen, Z. Tang, D. Wu, R. Fu and D. Jiang, *Chem. Commun.*, 2014, **50**, 4788.

137. Y. Xu, Z. Li, F. Zhang, X. Zhuang, Z. Zeng and J. Wei, *RSC Advances*, 2016, **6**, 30048.

138. Y. Zhi, S. Ma, H. Xia, Y. Zhang, Z. Shi, Y. Mu and X. Liu, *Appl. Catal., B*, 2019, **244**, 36.

139. Y. Liao, Z. Cheng, W. Zuo, A. Thomas and C. F. J. Faul, *ACS Appl. Mater. Interfaces*, 2017, **9**, 38390.

140. S. Bhattacharyya, D. Samanta, S. Roy, V. P. Haveri Radhakantha and T. K. Maji, *ACS Appl. Mater. Interfaces*, 2019, **11**, 5455.

141. C. Gu, Y. Chen, Z. Zhang, S. Xue, S. Sun, K. Zhang, C. Zhong, H. Zhang, Y. Pan, Y. Lv, Y. Yang, F. Li, S. Zhang, F. Huang and Y. Ma, *Adv. Mater.*, 2013, **25**, 3443.

142. D. F. Zeigler, S. L. Candelaria, K. A. Mazzio, T. R. Martin, E. Uchaker, S.-L. Suraru, L. J. Kang, G. Cao and C. K. Luscombe, *Macromolecules*, 2015, **48**, 5196.

143. P. M. DiCarmine, T. B. Schon, T. M. McCormick, P. P. Klein and D. S. Seferos, *J. Phys. Chem. C*, 2014, **118**, 8295.

144. Y. Liao, H. Wang, M. Zhu and A. Thomas, *Adv. Mater.*, 2018, **30**, 1705710.

145. K. Yuan, P. Guo-Wang, T. Hu, L. Shi, R. Zeng, M. Forster, T. Pichler, Y. Chen and U. Scherf, *Chem. Mater.*, 2015, **27**, 7403.

146. M. Shao, Q. Chang, J.-P. Dodelet and R. Chenitz, *Chem. Rev.*, 2016, **116**, 3594.

147. C. Song and J. Zhang, in *PEM Fuel Cell Electrocatalysts and Catalyst Layers: Fundamentals and Applications*, ed. J. Zhang, Springer London, London, 2008, DOI: 10.1007/978-1-84800-936-3_2, pp. 89.

148. R. L. Doyle and M. E. G. Lyons, in *Photoelectrochemical Solar Fuel Production: From Basic Principles to Advanced Devices*, eds. S. Giménez and J. Bisquert, Springer International Publishing, Cham, 2016, DOI: 10.1007/978-3-319-29641-8_2, pp. 41.

149. N. Mahmood, Y. Yao, J.-W. Zhang, L. Pan, X. Zhang and J.-J. Zou, *Adv. Sci.*, 2018, **5**, 1700464.

150. M. Chhetri, S. Maitra, H. Chakraborty, U. V. Waghmare and C. N. R. Rao, *Energy Environ. Sci.*, 2016, **9**, 95.

151. X. Wang, L. Yu, B. Y. Guan, S. Song and X. W. Lou, *Adv. Mater.*, 2018, **30**, 1801211.

152. T. Zhang, M.-Y. Wu, D.-Y. Yan, J. Mao, H. Liu, W.-B. Hu, X.-W. Du, T. Ling and S.-Z. Qiao, *Nano Energy*, 2018, **43**, 103.

153. J. Di, C. Yan, A. D. Handoko, Z. W. Seh, H. Li and Z. Liu, *Mater. Today*, 2018, **21**, 749.

154. Z. Zhu, H. Yin, C.-T. He, M. Al-Mamun, P. Liu, L. Jiang, Y. Zhao, Y. Wang, H.-G. Yang, Z. Tang, D. Wang, X.-M. Chen and H. Zhao, *Adv. Mater.*, 2018, **30**, 1801171.

155. B. C. Patra, S. Khilari, R. N. Manna, S. Mondal, D. Pradhan, A. Pradhan and A. Bhaumik, *ACS Catal.*, 2017, **7**, 6120.

156. S. Cui, M. Qian, X. Liu, Z. Sun and P. Du, *ChemSusChem*, 2016, **9**, 2365.

157. K. K. S. Saha, S. Sivakumar, R. G. S. Pala, *Journal of the Indian Institute of Science*, 2016, **96:4**, 325.

158. J. O. M. Bockris, *The Journal of Chemical Physics*, 1956, **24**, 817.

159. F. Song, L. Bai, A. Moysiadou, S. Lee, C. Hu, L. Liardet and X. Hu, *J. Am. Chem. Soc.*, 2018, **140**, 7748.

160. J. S. Kim, B. Kim, H. Kim and K. Kang, *Adv. Energy Mater.*, 2018, **8**, 1702774.

161. K. Huang, Y. Sun, Y. Zhang, X. Wang, W. Zhang and S. Feng, *Adv. Mater.*, 2018, **0**, 1801430.

162. J. Zhang, G. Chen, K. Müllen and X. Feng, *Adv. Mater.*, 2018, **30**, 1800528.

163. K. Gao, B. Wang, L. Tao, B. V. Cunning, Z. Zhang, S. Wang, R. S. Ruoff and L. Qu, *Adv. Mater.*, 2018, **0**, 1805121.

164. D. Wu, Q. Xu, J. Qian, X. Li and Y. Sun, *Chem. Eur. J.*, 2019, **25**, 3105.

165. B.-Q. Li, S.-Y. Zhang, B. Wang, Z.-J. Xia, C. Tang and Q. Zhang, *Energy Environ. Sci.*, 2018, **11**, 1723.

166. L. Lai, J. R. Potts, D. Zhan, L. Wang, C. K. Poh, C. Tang, H. Gong, Z. Shen, J. Lin and R. S. Ruoff, *Energy Environ. Sci.*, 2012, **5**, 7936.

167. M. Zeng, Y. Liu, F. Zhao, K. Nie, N. Han, X. Wang, W. Huang, X. Song, J. Zhong and Y. Li, *Adv. Funct. Mater.*, 2016, **26**, 4397.

168. M. S. Ahmed, B. Choi and Y.-B. Kim, *Sci. Rep.*, 2018, **8**, 2543.

169. A. Aijaz, J. Masa, C. Rösler, W. Xia, P. Weide, A. J. R. Botz, R. A. Fischer, W. Schuhmann and M. Muhler, *Angew. Chem. Int. Ed.*, 2016, **55**, 4087.

170. Y. Qian, Z. Hu, X. Ge, S. Yang, Y. Peng, Z. Kang, Z. Liu, J. Y. Lee and D. Zhao, *Carbon*, 2017, **111**, 641.

171. J. Zhang and L. Dai, *Angew. Chem. Int. Ed.*, 2016, **55**, 13296.

172. J.-S. Lee, S. Tai Kim, R. Cao, N.-S. Choi, M. Liu, K. T. Lee and J. Cho, *Adv. Energy Mater.*, 2011, **1**, 34.

173. J. Fu, D. U. Lee, F. M. Hassan, L. Yang, Z. Bai, M. G. Park and Z. Chen, *Adv. Mater.*, 2015, **27**, 5617.

174. M. Yu, Z. Wang, C. Hou, Z. Wang, C. Liang, C. Zhao, Y. Tong, X. Lu and S. Yang, *Adv. Mater.*, 2017, **29**, 1602868.

Chapter 2

Photo- and Electro-chromic Nanoscale Metal-Organic Framework

Abstract

In this chapter, a redox-active nanoscale metal organic framework (**NMOF**) has been synthesized by the coordination modulation approach. **NMOF** constitutes redox active N,N'-di(4-pyridyl)-1,4,5,8-naphthalenediimide (bpNDI) ligand which act as a pillar and biphenyl dicarboxlic acid (bpdc) ligand as a spacer. The ligands are connected by hepta coordinated cadmium(II) and dodecanoic acid as the modulator to restrict the size of MOF to nanoscale dimensions and thus 1-D tape like morphology is obatined. This forms an interpenetrated structure and the thus the donor acceptor system. The close spacial placement of donor (bpdc) and acceptor (bpNDI) helps in formation of long-lived charge-separated states of bpNDI by the transfer of electron transfer between the struts of interpenetrated structure, which is accompanied by the colour change and thus shows photochromic behaviour. Moreover, on the application of external potential, a colour change from yellow to dark brown was obtained due to the electrogenerated radical anion state of NDI and thus showing the electrochromic nature of **NMOF**. The electrogenerated dianion state is further stabilized by counter cations having different sizes and thus **NMOF** is shown to be a potential material for electrical energy storage. It is envisioned that the approach followed to form processable trifunctional **NMOF** is a step forward towards the coupling of photovoltaic and energy storage devices.

1. Introduction

Metal-organic frameworks (MOFs) are a class of organic-inorganic hybrid materials formed by the assembly of organic linkers and inorganic metal centers or clusters as node.[1-3] These materials possessing large surface area and crystallinity are promising materials for variety of applications such as gas storage and separation, sensing, self cleaning, photocatalytic water splitting and carbon dioxide reduction to value added fuels and many more.[2-10] Now-a-days, researchers are trying to exploit the use of MOFs in electronic devices such as organic light emitting diodes (OLEDs), solar cells, photochromic and electrochromic devices.[11-13] But a major drawback of MOFs is the lack of processability. To overcome this, one of the ways is downsizing the MOF to nanoscale or mesoscale. Nanoscale MOFs (**NMOFs)** are generally synthesized by chemically modulated methods[14], microwave assisted synthesis[15], surfactant mediated synthesis[16] and micro emulsion methods.[16] This leads to a good control over the size and the morphology without varying the desired chemical composition.[17] **NMOF**s have shown distinct performance in various applications such as energy storage, biological applications, catalysis and separation of small molecules.[18-20] Their high surface area, smaller diffusion barrier for adsorbates to the surface and permanent porosity allows facile substrate diffusion through the pores and thus leading to attractive applications.[21] But their potential in electrochemical devices is exploited only sporadically because of shortcomings, partly, due to the presence of redox inactive metal centers possessing d^0 or d^{10} configurations which will eventually lead to the poor charge transport within the framework. As a solution, use of redox active ligands not only improve the charge transport but also can show response towards various external stimuli such as application of potential.[22] The use of redox active ligands has been exploited for various applications in the field of organic electronics[23], energy storage devices[24] etc. Generally oxides of nickel or tungsten and Prussian blue analogs are used as the electrochromic materials.[25, 26] But these materials lack processability and cannot be tuned according to the requirements. As an alternative, Dinca *et al*. grew Zn-pyrazolate MOF thin films containing redox active naphthalene diimide (NDI) based ligands on FTO substrate which changed colour upon the application of potential.[22] Whereas, Dichtel *et al*. stabilized the electrogenerated NDI dianions by different cations and showed the application in electrical energy storage.[27] Apart from this, photochromic materials are widely used in photochromic displays[28], protection gears such as spectacles and many more. Photochromic materials involve the charge transfer between two molecular species which is triggered by light.[29] To achieve this, porous frameworks provide an edge over the conventional inorganic materials by providing a well defined space for the encapsulation of the chromophoric guest molecule that can undergo transformation in chemical state with light as the stimulus. But, this blocks the pore and prevents the use in various electrochemical applications which require free pores for easy and facile movement of counter ions in the framework. In this situation, well defined geometry of metal ions and the freedom to use different ligands helps to achieve ligand to ligand charge transfer. This requires the close placement of an electron donating and an electron accepting species that allows facile and complete electron transfer between the donor and the acceptor molecule such that the charge separated state is long lived in nature.[30] Recently, Han *et al*. utilized the charge transfer ability and redox activity of naphthalene diimide ligand upon its use in Zn-based MOF and thus showed photochromic nature with sunlight as stimuli and electrochromic nature with MOF thin films.[31] But still, the development of a trifunctional material possessing photochromism, electrochromism and cation dependence for energy storage is not well explored. The development of such trifunctional systems will be a step forward towards much needed application of a single photovoltaic device capable of storing the converted electrical energy.

Here, a trifunctional redox active nanoscale metal-organic framework (**NMOF**) has been successfully designed and synthesized utilizing the coordination modulation method. The obtained **NMOF** is highly processable and is able to show electrochromic as well as photochromic behavior and is found to be a potential material for energy storage applications. Herein, redox active naphthalene diimide (NDI) is functionalized with 4-aminopyridine to form N,N'-di(4-pyridyl)-1,4,5,8-naphthalenediimide (bpNDI) molecule. NDI has been used widely as n-type molecule, due to its electron accepting properties, in various photovoltaic devices, organic electronics, sensors etc.[32, 33] The presence of carbonyl groups in the molecule act as the electron acceptor and it has been shown that the reduced form can bind to different metal ions and thus can be used in energy storage devices.[27] Here, in **NMOF**, bpNDI ligand act as a pillar and biphenyl dicarboxlic acid (bpdc) ligand as a spacer along with hepta coordinated cadmium(II) and dodecanoic acid as the modulator to stop the crystallization process. This forms an interpenetrated structure and the thus the donor acceptor system. So with this a smart window can be devised which due to its photochromic properties can change its colour from light brown to dark brown. Moreover when it is coupled with a photovoltaic cell, will change its colour as well as store the energy which can be used later on for different applications and give back the transparent window. Scheme 1 shows the overview of the chapter.

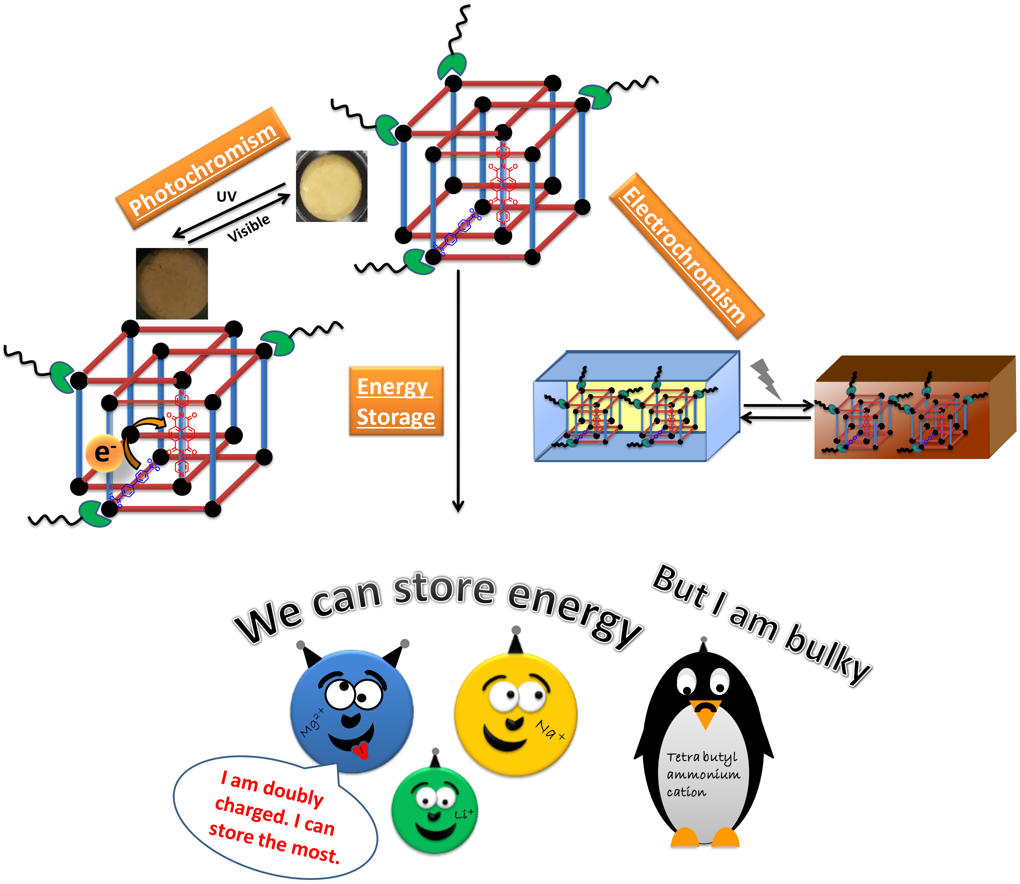

Scheme 1: Schematic showing overview of the chapter.

2. Experimental Section

2.1 Materials

$Cd(NO_3)_2.4H_2O$, biphenyldicarboxlic acid (bpdc), dodecanoinc acid (dda) and DMF were obtained from Sigma Aldrich Chemicals pvt. Ltd. and Spectrochem, and were used as it is without any further purification. Bipyridyl naphthalene diimide (bpNDI) was synthesized from 1,4,5,8-naphtalenetetracarboxlic dianhydride and 4-aminopyridine. All the anhydrous solvents were used as received.

2.2 Synthesis of bpNDI

For the synthesis of bpNDI, 1,4,5,8- napthalenetetracarboxlic dianhydride (1g, 3.7 mmol) and 4-aminopyridine (770 mg, 8.2 mmol) were added to the schlenk flask. 50 mL of anhydrous DMF was added to the reaction mixture under inert conditions. This was then refluxed at 155°C in an oil bath. After 12 hours, it was cooled to room temperature and then further cooled in ice bath for 1 hour. The slurry obtained was filtered and washed with chloroform and acetone. The obtained product was dried in vacuum. bpNDI was confirmed with ^{1}H NMR spectrum (Figure 1). ^{1}H NMR (400 MHz, DMSO-d_6) δ = 7.57 (d, 4H), 8.74 (s, 4H), 8.8 (d, 4H).

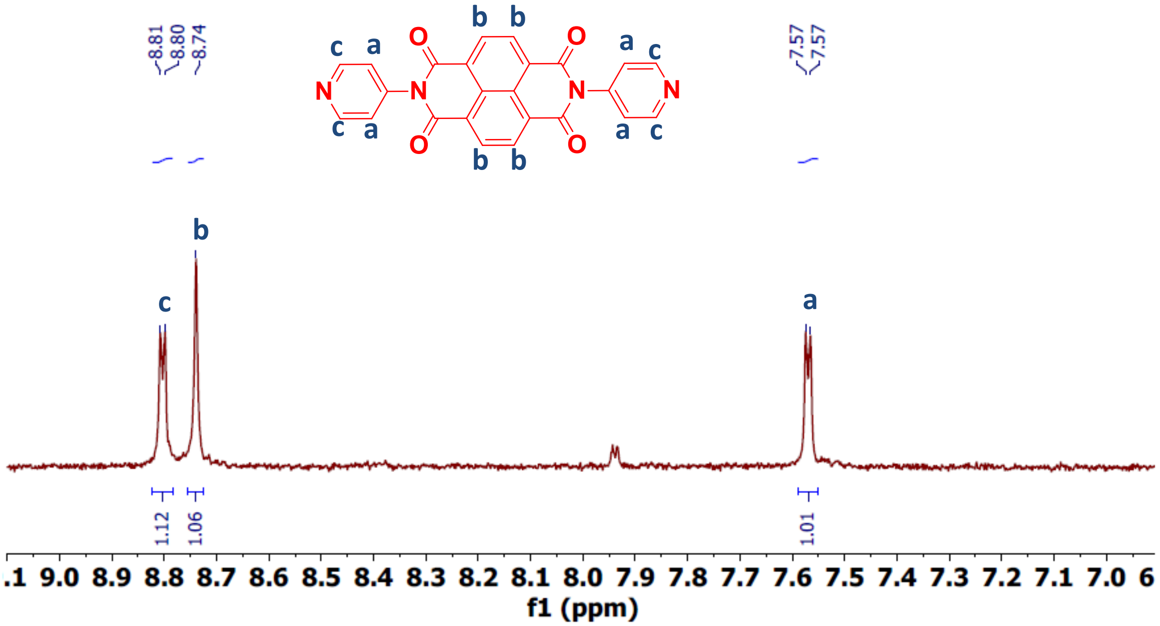

Figure 1: ^{1}H NMR of bpNDI ligand.

2.3 Synthesis of NMOF

To prepare **NMOF**, $Cd(NO_3)_2.4H_2O$ (0.1 mmol, 0.03 g), bpdc (0.1 mmol, 0.024g), dodecanoic acid (0.05 mmol, 0.010 g) and bpNDI (0.05 mmol, 0.210 g) were dissolved in 10 mL DMF in a 30 ml vial. The vial was sealed tightly with Teflon tape and was kept at 80 °C in an oil bath, without stirring, for 3 days. The mixture was then cooled to room temperature. The precipitate obtained was filtered and washed with DMF.

2.4 Physical Measurements

Infrared spectra (FT-IR) were obtained in transmittance mode by grinding the sample along with KBr and making its pellet using KBr press. For the measurements, Bruker FT-IR spectrophotometer was used. Thermogravemetric analysis (TGA) was performed by Mettler Toledo TGA 850 instrument by varying the temperature from 25 ^{o}C to 750 ^{o}C at the rate of 5 ^{o}C min^{-1} under nitrogen atmosphere. Powder X-Ray diffraction pattern was obtained using Bruker D8 discover and Cu-Kα radiation. The X-Ray tube was accelerated at 40 kV. 2ϴ was varied from 5^{o} to 50^{o} and the scan time was set to be 1 hour. Field emission scanning electron microscopy (FESEM) images were obtained by Lica S440I at an accelerating voltage of 10 kV under high vacuum by drop casting the dispersion of compound in ethanol onto cleaned a silicon wafer. Transmission emission microscopy images were captured using Jeol JEM 310 at the accelerating voltage of 10 kV. The sample was dispersed in ethanol and was drop casted onto a carbon coated grid. The electronic absorbance spectra were recorded in Perkin Elmer Lambda 750 UV-VIS-NIR Spectrometer. Solid state UV-Vis spectra were recorded in reflectance mode and the wavelength was varied from 800 nm to 250 nm. Hamamatsu C11924-201 torch light having a wavelength of 365 nm was placed in head to head position to solid state UV-Vis spectrometer sample holder. The reflectance spectrum was recorded at different intervals which were converted into absorbance data. ^{1}HNMR is recorded on a Bruker AV-400 spectrometer with chemical shifts reported as ppm.

2.5 Adsorption measurements

Porous nature of the sample was studied by the adsorption measurements using Quantachrome Quadrasorb instrument at 77 K for nitrogen and 195 K for carbon dioxide measurements. 170 mg of the sample was transferred into the sample cell and was degassed at 135 ^{o}C for 6 hours under the vacuum of 1x10^{-1} Pa for activation of **NMOF**. He gas was used to fill the chamber and make it free from the presence of nitrogen and carbon dioxide. Further all the operations during the measurement were computer controlled.

2.6 Electrochemical Measurements

Electrochemical measurements were done using Autolab PGSTAT12 potentiostat/galvanostat. Cyclic voltammetry curves were recorded by coating the dispersion of the sample onto the glassy carbon electrode. The glassy carbon electrode was polished by rubbing it onto the polishing cloth along with alumina powder (0.05 um mesh). The electrode was then rinsed with MilliQ water followed by ultrasonication in MilliQ water for about 10 seconds. The electrode was dried in open air and a mirror like shining surface was obtained. The ink was prepared by dispersing 2.5 mg of **NMOF** in 190 uL of ethanol along with 10 uL of Nafion solution (5 wt %, Aldrich). 6 uL of this dispersion was coated onto the pre cleaned glassy carbon electrode. Electrochemical measurements were carried out in a three electrode cell configuration using Ag/Ag^+ non aqueous electrode as the reference electrode, sample coated glassy carbon electrode as the working electrode and Pt coil as the counter electrode. Perchlorate salts of tetrabutylammonium, sodium, potassium and lithium were dissolved in dry acetonitrile possessing the concentration of 0.1 M as the electrolyte. The electrolyte was degassed by purging Ar gas for 20-25 min before starting the experiment.

2.7 UV-Vis Spectroelectrochemistry

UV-Vis spectroelectrochemical measurements were done using preconfigured portable JAZ extended UV-Vis spectrophotometer JAZ-EL200-XR1. The spectrum was recorded in plastic cuvette placed in the holder between the source and the detector. The source and detector were connected to the cuvette holder using optical fibers. Light and dark spectra were recorded before the recording of the spectra. For the application of the potential CHI760E electrochemical workstation was used in three electrode configuration with Ag/Ag^+ non aqueous as the reference electrode, Pt coil as the counter electrode and indium tin oxide (ITO) electrode was used with conducting copper tape contact as the working electrode. 20 uL of the above used dispersion was drop casted onto the clean ITO and dried in open air. 0.1 M of tetrabutylammonium hexafluorophosphate was used as the electrolyte and was purged with argon gas before the experiment.

2.8 Electrical Conductivity

Electrical conductivity measurements were done using Keitley 2400 sourcemeter. 60 uL of the above used dispersion was drop casted onto the clean glass slides of size 1x1 cm^2. The central portion of the glass slides was masked with Teflon. For proper ohmic electrical contacts, aluminum metal was deposited onto the slides by physical vapour deposition technique. The I-V curve was obtained with the sourcemeter. Further, the above used lamp was used to shine the light onto the glass slides in head to head orientation and the electrical conductivity was recorded at different intervals.

3. Results and Discussion

3.1. Characterization

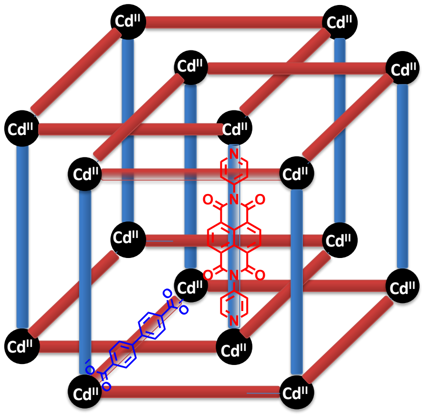

Figure 2: Schematic showing the structure of bulk MOF.

As reported, MOF [{Cd(bpdc)(bpNDI)}.4.5H_2O.DMF]$_n$ is a redox active twofold interpenetrated 3-D porous framework (figure 2).[30] This is formed by the solvothermal method by the formation of the a 2D rhombic network by bpdc linker. This network is bipillared by bpNDI to form a 3-D framework structure along with hepta coordinated cadmium(II) centre. This being an interpenetrated structure, has parallel alignment of bpNDI linkers and a close proximity with bpdc as a strut of another entangled net. It is shown by EPR spectra that electron transfer takes place from bpdc to bpNDI and thus forms a charge separated state. But this being a bulk MOF is not processable in nature and thus limiting its use in devices etc. To overcome this problem, crystal downsizing of MOFs has been carried out by coordination modulation method. Thus, use of dodecanoic acid (dda) having carboxylate as the similar functional group as in the linker bpdc is used as a modulator. **NMOF** is synthesized by dissolving Cd(NO_3).4H_2O, bpdc, dda and bpNDI in DMF under solvothermal condition in a glass vial for three days. The precipitate formed were filtered and washed with DMF. Presence of the peaks corresponding to bpNDI in FT-IR spectrum (Figure 3) of **NMOF** showed the presence of bpNDI in the framework.

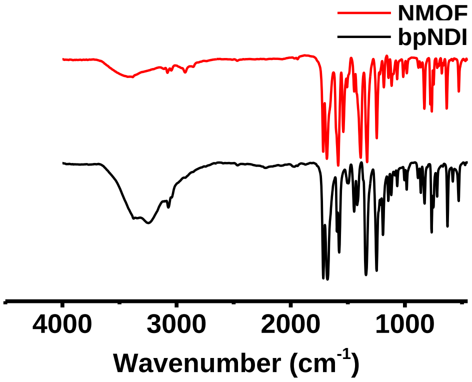

Figure 3: IR spectrum of bpNDI linker and **NMOF**.

Sharp peaks in powder X-ray diffraction of **NMOF** (Figure 4a) showed high crystallinity of **NMOF** and are in good accordance with the simulated pattern obtained from the bulk MOF. This showed that the **NMOF** retains the original crystal structure as of the bulk MOF. Thermogravimetric analysis (Figure 4b) showed the initial decrease in the weight upto 150 °C which might be due to the loss of solvent molecules. Further the framework was found to be stable till 315 °C followed by degradation of the framework at high temperature.

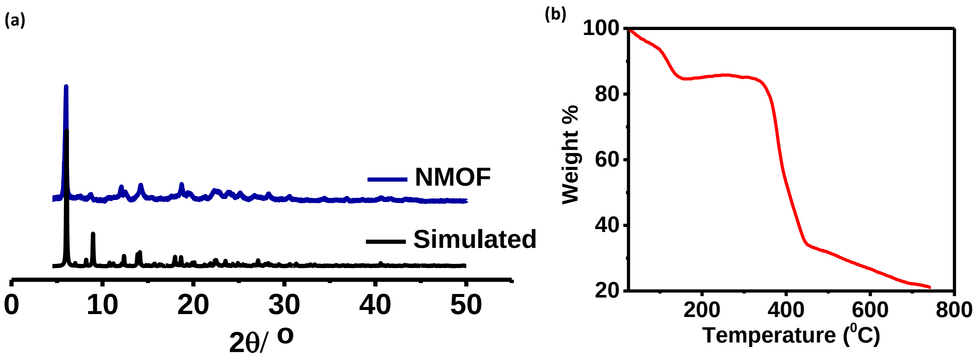

Figure 4: (a) Simulated and obtained PXRD pattern; (b) Thermogravimetric analysis (TGA) of **NMOF**.

To study the porosity of the framework, adsorption study was carried out. It was found that the framework did not show any N_2 uptake (Figure 5a). The presence of C=O in bpNDI and the quadrapole nature of CO_2 molecules motivated us to study the CO_2 uptake of the framework. This showed a typical type 1 curve (Figure 5b) with the maximum uptake of 62.7 ml/g which corresponded to the Langmuir surface area (obtained from CO_2 adsorption isotherm) of 282.341 m^2/g.

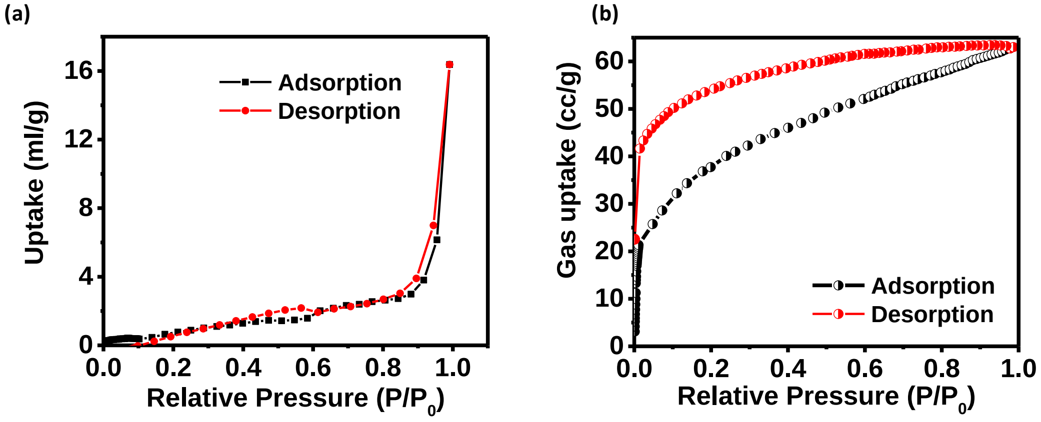

Figure 5: (a) N_2 adsorption curve; (b) CO_2 adsorption curves of **NMOF**.

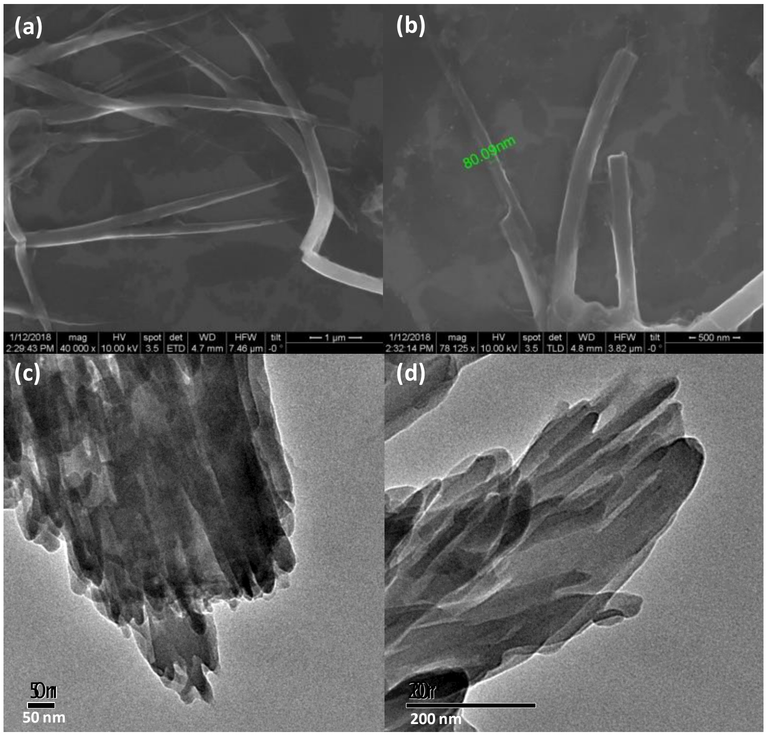

Figure 6: (a,b) FESEM images; (c,d) TEM images of **NMOF**.

The morphology of the obtained **NMOF** was studied by field emission scanning electron microscope (FESEM) and transmission electron microscope (TEM). These images showed small tape like structures protruding out from a bigger branch (Figure 6a-d). This proves that the formation of the **NMOF** happens when the further crystallization of the MOF structure stops due to the single sided functionalization of the modulator dda.

3.2. Electrochemical and Optical Properties

The CV of **NMOF** was recorded in anhydrous acetonitrile with tetrabutylammonium hexaflorophophate ($TBAPF_6$) as the supporting electrolyte (Figure 7). As Cd(II) forms a d^{10} system is redox inactive in nature and thus only redox active species in the system is bpNDI which contributes to all the faradic processes. Two reduction peaks were observed at -0.840 V and -1.295 V corresponding to the one electron reduction of NDI / NDI$^{\bullet-}$ and NDI$^{\bullet-}$ / NDI^{2-}. Also two oxidation peaks at -1.143 V and -0.685 V obtained showing the one electron oxidation of NDI^{2-} / NDI$^{\bullet-}$ and NDI$^{\bullet-}$/ NDI.

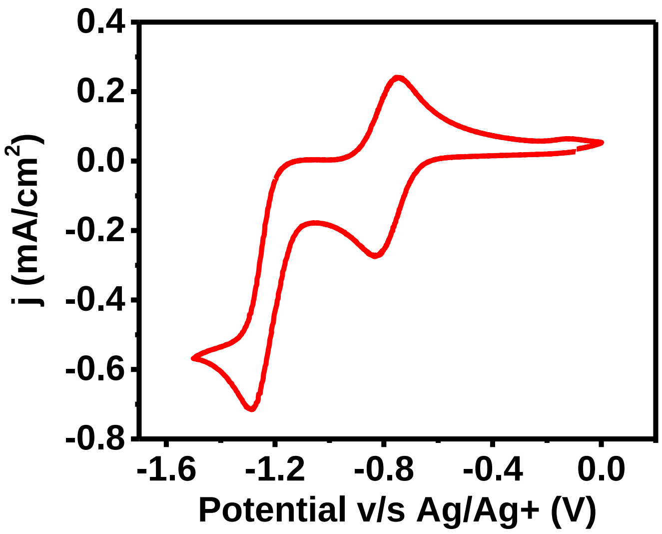

Figure 7: Cyclic voltammetry curve of **NMOF** showing different redox peaks.

Further to use **NMOF** as a potential material for an electrochromic device, **NMOF** was drop casted onto the ITO substrate which acted as the working electrode along with non aqueous Ag/Ag^+ as the reference electrode and Pt coil as the counter electrode (Figure 8). In situ absorbance spectrum of the coated film was recorded while cycling the potential from 0 V to -1 V and back to 0 V at the rate 50 mV/s in 0.1 M concentration of **TBAPF$_6$** in anhydrous acetonitrile. As prepared film showed absorbance maxima at 356 nm and 376 nm initially. It was observed that the two peaks at 471 nm and 604 nm appeared at potential -0.840 V which corresponded to the formation of NDI$^{\bullet-}$. This was followed by the colour change to dark brown.

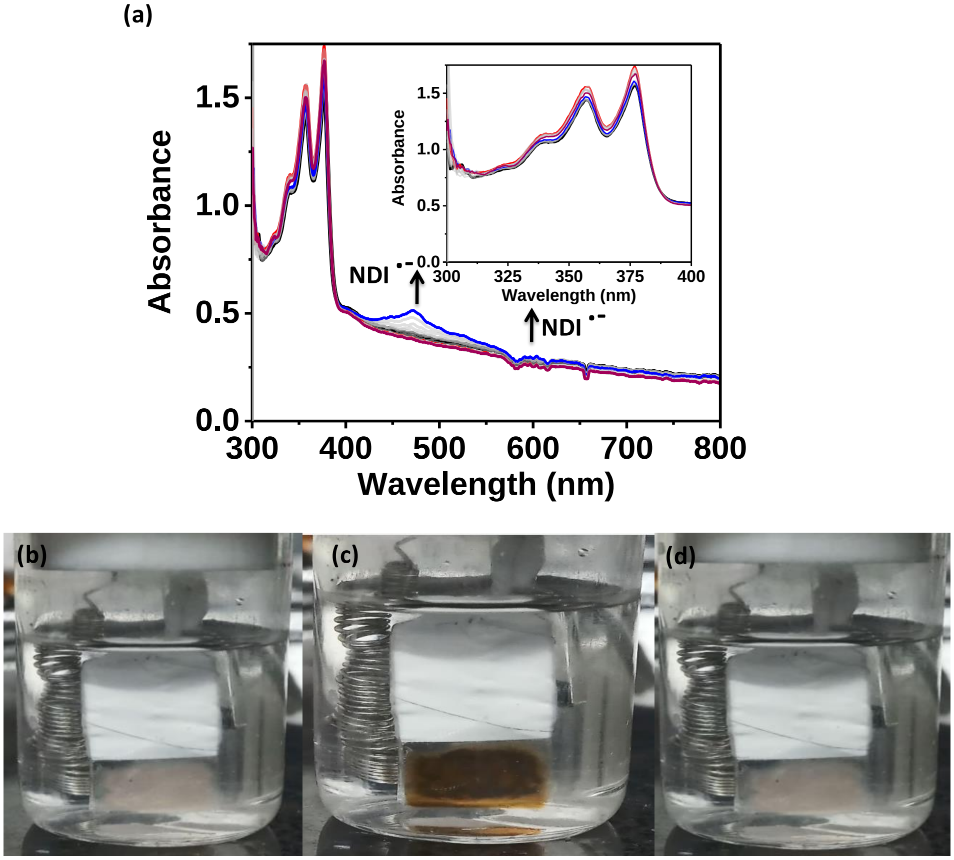

Figure 8: (a) Spectroelectrochemical spectra of **NMOF**; Optical images of **NMOF** coated on ITO (b) before the experiment; (c) on formation of NDI$^{\bullet-}$; (d) on formation of NDI.

This process was completely reversible in nature as shown by the absorbance spectra and the corresponding images (Figure 8b-d). Due to the presence of a donor and an acceptor, the photochromic behavior of was also examined. As expected, on shining the light of 365 nm, colour changed from yellow to brown, as shown in Figure 9a. To study the colour change, UV-Vis spectrum was recorded at various time intervals. It is observed that **NMOF** absorbs in range 300 nm to 400 nm in its ground state. On shining the light for very small duration, new bands start to appear at 485 nm and 602 nm due to the electron transfer from bpdc to bpNDI ligand and thus the formation of NDI $^{\bullet-}$ as in Figure 9b. This is also confirmed by the results obtained from the spectroelectrochemistry experiments. The peaks in the range of 300-400 nm are observed due to the π-π* and n- π* transitions in the NDI core.[30] It can be seen that intensity of peaks at 485 nm and 602 nm on shining the light for longer duration, thus indicating the conversion of more fraction of sample in its charge separated state.

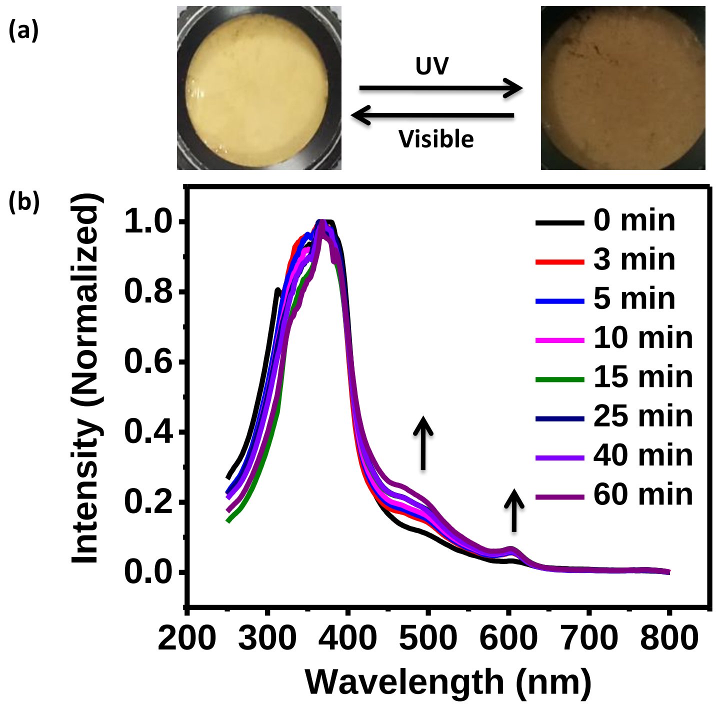

Figure 9: (a) Optical images of **NMOF** before and after shining light; (b) UV-Vis spectra recorded at different intervals.

3.3. Electrical Properties

As **NMOF** possessed a redox active ligand which is converted to a radical anion in its charge separated state on shining light, we envisioned that this on binding with the metal centre would create a path for the electron transfer through the **NMOF**. So, the intrinsic conductivity of **NMOF** was studied by coating the sample onto the pre cleaned glass slide and making the ohmic contacts with aluminium. It was observed that **NMOF** possessed an initial conductance of 1.24×10^{-12} S in its neutral state (Figure 10). But on shining light for 60 min, when enough of the sample was in charge separated state, the conductance increased to 16 times from its initial value to 2.06×10^{-11} S. This increase in the electronic conductivity confirmed the fact that the material in its charge separated state allows faster electron transfer. The proposed electron transfer mechanism is through the bpNDI ligands and the metal centre on the application of the external bias. It has been shown that the presence of Fe(II), having d^6 electronic configuration, possesses high energy valence electrons and lower activation energies is found to be unique to posses large intrinsic electrical conductivity.[34, 35] Here, the presence of Cd(II), possessing d^{10} configuration, is expected to provide a large amount of resistance to the electron flow and thus the low intrinsic conductivity of the framework.

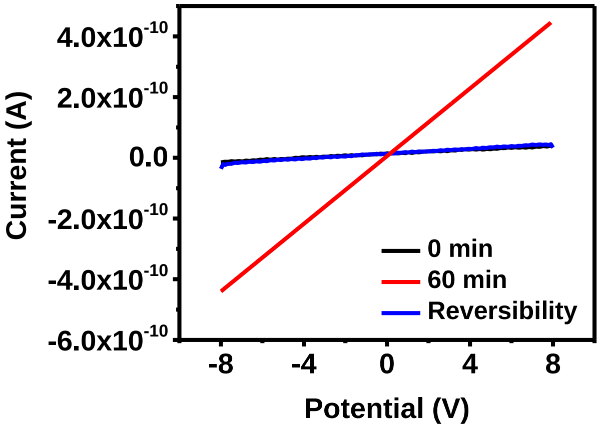

Figure 10: I-V curve before (black) and after (red) shining light. The reversibility curve (blue) resembles the 0 min (black) curve.

3.4. Stabilization of Electrochemically Reduced NDI With Different Counter Cations

As NDI can be converted into radical anion and dianion states on application of potential, we thought to study the interaction of different counter cations with reduced forms of NDI by varying the supporting electrolyte. As it is well known that MOFs generally exhibit electron hopping mechanism and thus the charge transfer within the MOF takes place through the diffusion of the electrons.[36] To balance this charge the counter cation from the electrolyte is required. Thus this counter cation must diffuse through the material. So, **NMOF** possessing porosity, high surface area and closely spaced NDI ligands allows facile diffusion of the counter cation through the material and thus helps to stabilize the reduced forms. Moreover, this being insoluble in nature will help to increase the cycling stability. Here, various counter cations such as tetrabutylammonium cation (TBA$^+$), lithium cation (Li$^+$), potassium cation (K$^+$) and magnesium cation (Mg^{2+}) as their perchlorate salts are used as the supporting electrolyte and the CV was recorded in dry acetonitrile (Figure 11).

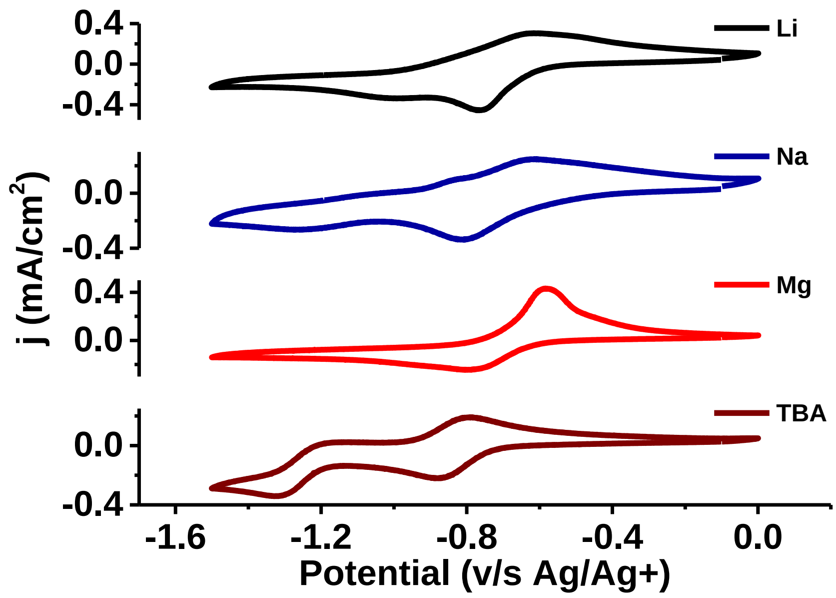

Figure 11: CV of **NMOF** in presence of different counter cations.

It was observed that the due to the large size of TBA$^+$ two reduction peaks corresponding to the formation of NDI$^{\cdot -}$ and NDI^{2-} and two oxidation peaks corresponding to reversible process were observed at -0.87 V, -1.30 V and -1.21 V, -0.80 V respectively. The reduction potentials in case of Li$^+$ and Mg$^+$ were shifted to positive potentials due to the ionic interactions of the reduced NDI with the cation as shown in Table 1. This is due to the smaller size and the different charge densities of these cations. But in the case of Mg $^{2+}$, both the reduction and oxidation peaks merge into a single peak. The second reduction peak is shifted largely by 0.54 V thus showing more stabilization of the dianion species. This leads to more energy storage due to the divalent nature of the magnesium.

Table 1: Reduction potentials of **NMOF** in presence of different counter cations.

Cation	E_{Red1}(V)	E_{Red2}(V)	ΔE_{Red1}(V)	ΔE_{Red2}(V)
TBA^+	-0.87	-1.32	-	-
Li^+	-0.76	-1.00	0.11	0.32
Na^+	-1.81	-1.25	0.06	0.07
Mg^{2+}	-0.78	-0.78	0.09	0.54

4. Conclusion

In conclusion, nanoscale redox active donor acceptor metal organic framework (**NMOF**) was designed and synthesized. The control over tape like morphology was achieved by using a monodentate ligand (dodecanoic acid) as the modulator. **NMOF** was found to exhibit photochromism on shining light due to the close proximity and struct to struct electron transfer from donor linker to acceptor pillar. The process was reversible and the charge separated state was found to be long lived. **NMOF** also found to possess reversible electrochromic behavior due to the presence of redox active bipyridyl naphthalene diimide (bpNDI) ligand which can undergo colour change on varying its redox state. Moreover, the porous nature and crystallininty of **NMOF** helped in smooth diffusion of various counter cations, possessing different sizes and charge density, through the pores and thus stabilize the reduced state of bpNDI. The shift in the reduction potentials on varying the counter cation shows different extent of stabilization of the reduced state of naphthalene diimide and thus makes this a suitable material for energy storage applications.

5. References

1. H. Furukawa, K. E. Cordova, M. O'Keeffe and O. M. Yaghi, *Science*, 2013, **341**, 1230444.
2. H.-C. Zhou, J. R. Long and O. M. Yaghi, *Chem. Rev.*, 2012, **112**, 673.
3. H.-C. J. Zhou and S. Kitagawa, *Chem. Soc. Rev.*, 2014, **43**, 5415.
4. H. Wang, W. P. Lustig and J. Li, *Chem. Soc. Rev.*, 2018, **47**, 4729.

5. W. Ling, G. Liew, Y. Li, Y. Hao, H. Pan, H. Wang, B. Ning, H. Xu and X. Huang, *Adv. Mater.*, 2018, **30**, 1800917.
6. M. Liu, L. Tie, J. Li, Y. Hou and Z. Guo, *J. Mater. Chem. A*, 2018, **6**, 1692.
7. H. Li, Y. Sun, Z.-Y. Yuan, Y.-P. Zhu and T.-Y. Ma, *Angew. Chem. Int. Ed.*, 2018, **57**, 3222.
8. S. Kampouri, T. N. Nguyen, C. P. Ireland, B. Valizadeh, F. M. Ebrahim, G. Capano, D. Ongari, A. Mace, N. Guijarro, K. Sivula, A. Sienkiewicz, L. Forró, B. Smit and K. C. Stylianou, *J. Mater. Chem. A*, 2018, **6**, 2476.
9. D.-H. Nam, O. S. Bushuyev, J. Li, P. De Luna, A. Seifitokaldani, C.-T. Dinh, F. P. García de Arquer, Y. Wang, Z. Liang, A. H. Proppe, C. S. Tan, P. Todorović, O. Shekhah, C. M. Gabardo, J. W. Jo, J. Choi, M.-J. Choi, S.-W. Baek, J. Kim, D. Sinton, S. O. Kelley, M. Eddaoudi and E. H. Sargent, *J. Am. Chem. Soc.*, 2018, **140**, 11378.
10. S. Zhang, L. Li, S. Zhao, Z. Sun, M. Hong and J. Luo, *J. Mater. Chem. A*, 2015, **3**, 15764.
11. I. Mjejri, C. M. Doherty, M. Rubio-Martinez, G. L. Drisko and A. Rougier, *ACS Appl. Mater. Interfaces*, 2017, **9**, 39930.
12. D. Y. Lee, I. Lim, C. Y. Shin, S. A. Patil, W. Lee, N. K. Shrestha, J. K. Lee and S.-H. Han, *J. Mater. Chem. A*, 2015, **3**, 22669.
13. M. Gutiérrez, C. Martin, K. Kennes, J. Hofkens, M. Van der Auweraer, F. Sánchez and A. Douhal, *Adv. Opt. Mater.*, 2018, **6**, 1701060.
14. T. Tsuruoka, S. Furukawa, Y. Takashima, K. Yoshida, S. Isoda and S. Kitagawa, *Angew. Chem. Int. Ed.*, 2009, **48**, 4739.
15. S. H. Jhung, J. H. Lee, J. W. Yoon, C. Serre, G. Férey and J. S. Chang, *Adv. Mater.*, 2007, **19**, 121.
16. W. Lin, W. J. Rieter and K. M. L. Taylor, *Angew. Chem. Int. Ed.*, 2009, **48**, 650.
17. S. Furukawa, J. Reboul, S. Diring, K. Sumida and S. Kitagawa, *Chem. Soc. Rev.*, 2014, **43**, 5700.
18. K. Lu, T. Aung, N. Guo, R. Weichselbaum and W. Lin, *Adv. Mater.*, 2018, **30**, 1707634.

19. K. Ni, G. Lan, C. Chan, B. Quigley, K. Lu, T. Aung, N. Guo, P. La Riviere, R. R. Weichselbaum and W. Lin, *Nat. Commun.*, 2018, **9**, 2351.
20. F.-L. Li, Q. Shao, X. Huang and J.-P. Lang, *Angew. Chem.*, 2018, **130**, 1906.
21. E. A. Flügel, A. Ranft, F. Haase and B. V. Lotsch, *Journal of Materials Chemistry*, 2012, **22**, 10119.
22. C. R. Wade, M. Li and M. Dincă, *Angew. Chem. Int. Ed.*, 2013, **52**, 13377.
23. A. Bandhopadhyay and A. J. Pal, *J. Phys. Chem. B*, 2003, **107**, 2531.
24. J. Lv, Y.-X. Tan, J. Xie, R. Yang, M. Yu, S. Sun, M.-D. Li, D. Yuan and Y. Wang, *Angew. Chem. Int. Ed.*, 2018, **57**, 12716.
25. L. Shen, L. Du, S. Tan, Z. Zang, C. Zhao and W. Mai, *ChemComm*, 2016, **52**, 6296.
26. L. Hedley, L. Porteous, D. Hutson, N. Robertson and J. O. Johansson, *J. Mater. Chem. C*, 2018, **6**, 512.
27. C. R. DeBlase, K. Hernández-Burgos, J. M. Rotter, D. J. Fortman, D. dos S. Abreu, R. A. Timm, I. C. N. Diógenes, L. T. Kubota, H. D. Abruña and W. R. Dichtel, *Angew. Chem. Int. Ed.*, 2015, **54**, 13225.
28. Y. Yang, L. Guan and G. Gao, *ACS Appl. Mater. Interfaces*, 2018, **10**, 13975.
29. M.-S. Wang, G. Xu, Z.-J. Zhang and G.-C. Guo, *ChemComm*, 2010, **46**, 361.
30. N. Sikdar, K. Jayaramulu, V. Kiran, K. V. Rao, S. Sampath, S. J. George and T. K. Maji, *Chem. Eur. J.*, 2015, **21**, 11701.
31. Y.-X. Xie, W.-N. Zhao, G.-C. Li, P.-F. Liu and L. Han, *Inorg. Chem.*, 2016, **55**, 549.
32. H. I. Kim, M.-J. Kim, K. Choi, C. Lim, Y.-H. Kim, S.-K. Kwon and T. Park, *Adv. Energy Mater.*, 2018, **8**, 1702872.
33. P. M. Sonar, H. D. Pham, X. Li, W. Li, S. Manzhos and A. K. K. Kyaw, *Energy Environ. Sci.*, 2019, DOI: 10.1039/C8EE02744G.
34. L. Sun, C. H. Hendon, S. S. Park, Y. Tulchinsky, R. Wan, F. Wang, A. Walsh and M. Dincă, *Chem. Sci.*, 2017, **8**, 4450.
35. L. S. Xie, L. Sun, R. Wan, S. S. Park, J. A. DeGayner, C. H. Hendon and M. Dincă, *J. Am. Chem. Soc.*, 2018, **140**, 7411.
36. B. A. Johnson, A. Bhunia, H. Fei, S. M. Cohen and S. Ott, *J. Am. Chem. Soc.*, 2018, **140**, 2985.

Chapter 3

MOF Derived Co_3O_4@Co/NCNT Nanocomposite for Electrochemical Hydrogen Evolution, Flexible Zinc-Air Batteries and Overall Water Splitting

Abstract

Towards the goal of clean and sustainable environment, the development of a trifunctional electrocatalyst is a boon for energy storage and conversion devices such as regenerative fuel cells and metal air batteries. In this chapter, an already known MOF derived core-shell bifunctional electrocatalyst, **Co_3O_4@Co/NCNT**, is found to be an active electrocatalyst for hydrogen evolution reaction (HER) along with oxygen reduction reaction (ORR) and oxygen evolution reaction (OER). Detailed theoretical calculations proved nitrogen atom in nitrogen doped carbon nanotubes (NCNT) as the binding site for proton and thus proving **Co_3O_4@Co/NCNT** to be active for HER. Further, the bifunctionality of **Co_3O_4@Co/NCNT** towards ORR and OER helped in fabricating an electrically rechargeable Zn-air battery with high power density. Also, an all solid-state flexible and wearable battery with **Co_3O_4@Co/NCNT** as cathode and electrodeposited Zn on carbon fiber cloth as anode was shown to withstand its performance even under stressed conditions. Finally, the material being trifunctional in nature was used both as an anode and cathode material for the electrolysis of water which was powered by the Zn-air batteries with **Co_3O_4@Co/NCNT** as the cathode material. It is believed that the development of a trifuntional catalyst would help in wide commercialization of regenerative fuel cells.

1. Introduction

On the journey to find clean and sustainable alternatives to fossil fuels, hydrogen economy has emerged as the decades-long dream of researchers. But major challenges in achieving this dream are the production of hydrogen from clean and green sources, and the storage of the produced hydrogen gas. The challenge of storage of hydrogen gas has been achieved, to a large extent, by the development of highly porous materials possessing large surface areas such as metal-organic frameworks (MOFs).[1-3]To overcome the challenge of hydrogen production, photocatalytic and electrocatalytic water splitting is found as a solution to produce high purity hydrogen gas without many side reactions.[4-7] Electrocatalytic hydrogen evolution involves the reduction of protons to molecular hydrogen on the application of potential. Various noble metals catalysts such as Pt/C are still regarded as the state of art catalysts.[8] But these being highly expensive cannot be commercialized. As an alternative, various metal phosphides[9, 10], dichalcogenides[11, 12] or 2-D materials[13] have been developed. On the other hand, development of cheap and safe energy conversion and energy storage devices, such as fuel cells and metal-air batteries, is another rate determining step in achieving the goal of green economy. Oxygen reduction reaction (ORR) and oxygen evolution reaction (OER) are required for electrically rechargeable battery but these are kinetically sluggish reactions which restricts its use in metal air batteries. [14] Many state of art catalysts such as RuO_2 and IrO_2 can be used but their cost and scarcity restrict their use. Thus, the development of efficient and rechargeable metal air batteries for sustainable energy conversion and storage requires the development of cheap, non-noble metal and stable bifunctional catalysts capable of both oxygen reduction (ORR) and oxygen evolution reaction (OER) with low onset potentials and fast kinetics.[15] As the technology is advancing, the demand for flexible batteries is increasing for their use in smart clothes, on body sensors etc. On the other hand, the combination of OER and HER is essential for the development of efficient water electrolyses.[16] So the development of an efficient trifunctional catalyst is very important.

Various transition metal phosphides[17, 18], transition metal nitrides[19], transition metal oxides,[20] transition metal doped layered double hydroxides[21, 22], and heteroatoms such as boron[23, 24]sulphur[25, 26] and phosphorous[27] doped nitrogen containing 2-D materials are found out to be potential materials as bi-functional electrocatalysts for oxygen reactions. Moreover, transition metal doped in nitrogen doped metal free carbons such as carbon nanotubes, graphene layers have been proved to possess bifunctionality for both ORR and OER and thus shown to be stable and efficient cathode materials for zinc air batteries.[28] But these materials lack porosity which is essential for the formation of efficient gas diffusion cathode for Zn-air batteries. This is overcome by using porous metal-organic frameworks (MOFs) as the precursors for the synthesis of heteroatom doped carbon nanostructures and thus controlling the morphology. Various MOF derived bifunctional materials are reported for Zn-air batteries cathode possessing high power density.[29, 30] Recent reports show the encapsulation of Co in nitrogen doped CNTs (NCNT) or nanorods, obtained by pyrolyzing MOF at high temperature and different atmosphere, possess better activities than the non porous materials.[31] Similarly, MOF derived materials are also proved to be active for HER.[32] Recently, Yan et. al. showed crystalline/amorphous Co/Co_3O_4 core/shell 3-D nanosheets as efficient electrocatalysts for HER.[33] So embedding the Co/Co_3O_4 core/shell along with the graphitized or CNT matrix would be a good approach to develop a trifunctional catalyst. In another report, Jia et. al systematically demonstrated the defects obtained on removal of heteroatoms from graphene and thus the development of a trifuncional electrocatalyst.[34] This is required because the use of different catalysts for ORR, OER and HER would make the configuration of air batteries and water electrolyzers very difficult.

Herein, an already reported,[35] MOF derived core-shell **Co_3O_4@Co** moiety encapsulated in N doped carbon nanotubes (NCNT) is shown to be an active and stable electrocatalyst for hydrogen evolution reaction in acidic medium with low overpotential. As the material is already shown to be bifunctional in nature, towards both ORR and OER possessing low onset potentials with high efficiency and stability, is used as a cathode material in zinc air batteries possesing high power density. Moreover, for the development of flexible, light weight, wearable and knittable Zn-Air battery, carbon fibre cloth was chosen as the current collector. For the fabrication of anode, Zn was electrochemically deposited onto the carbon fibre cloth whereas; **Co_3O_4@Co/NCNT** on carbon fibre cloth was used as the cathode. The solid state gel was used as the electrolyte and the separator for the fabrication of the wearable battery. The battery was successfully tested for its knittable, foldable behavior and was shown to withstand the hole test. Finally, to show the practical application, three wearable batteries were connected in series to brightly light up an LED. Further, **Co_3O_4@Co/NCNT** being trifunctional in nature was not only used as a cathode and anode material in water electrolyzer but was also shown to split water to H_2 and O_2 in the electrolyzer powered by the Zn-air battery fabricated from the same material. Scheme 1 shows the overview of the chapter.

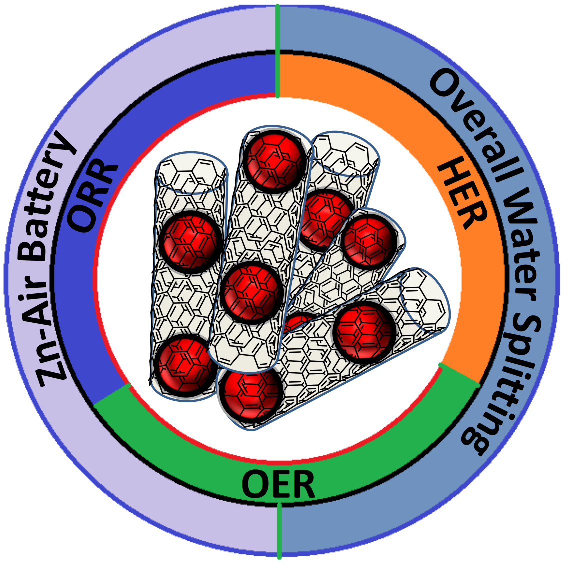

Scheme 1: Schematic describing overview of the chapter.

2. Experimental Section

2.1 Materials

All the desired chemicals and solvents were purchased from Sigma-Aldrich and were used without any further purification. $ZnSO_4.7H_2O$ and KCl used for electrodeposition were purchased from SD Fine Chemicals and Merck & Co. respectively.

2.2 Synthesis of Co_3O_4@Co/NCNT

Core-shell **Co_3O_4@Co/NCNT** was synthesized according to the known procedure[35]. In brief, MOF $\{[Co(bpe)_2(N(CN)_2].(N(CN)_2).5(H_2O)\}_n$ was synthesized by making a solution of $Co(NO_3)_2.6H_2O$ (291.03 mg) and $Na(N(CN)_2)$ (106.8 mg) in 15 mL of distilled water. Another solution of 1,2-bis(4-pyridyl)ethane (bpe) (220 mg) was mixed in 5 mL of ethanol. Then, bpe solution was added to the aqueous dicyanamide and $Co(NO_3)_2.6H_2O$

solution and stirred for 20 min. The pink precipitates formed were filtered and washed with copious amount of water ethanol mixture. The obtained MOF (800 mg) was carbonized in alumina boat under H_2/Ar (5% H_2 in 95 % Ar) flow. Temperature was raised to 800 ^{o}C at the rate of 5 ^{o}C/min and the temperature was maintained for 4 hours. The sample was cooled to room temperature. For the formation of Co_3O_4 shell, the carbonized sample was calcined in air at 250 ^{o}C (rate of heating is 5 ^{o}C/min)for 2 hours.

2.3 Physical Measurements

Powder X-ray diffraction of the sample was studied using Bruker D8 discover instrument by varying the 2θ from 10^{o} to 80^{o}. Raman spectrum was recorded using Jobin Yvon LabRam HR spectrometer with 632 nm He-Ne laser.

2.4 Computational Details

Spin-polarized density functional theory (DFT) based calculations were done by Quantum Espresso 5.2.0, using the plane wave basis of energy cut off 30 Ry, Rappe Rabe Kaxirus Joannopoulas ultrasoft pseudopotentials and the generalized gradient approximation parameters by Perdew, Burke & Ernzerhof (GGA-PBE) for exchange-correlation functional. A rectangualar supercell of carbon nanotube (CNT) containing 127 atoms of (20x20x17.2) Å has been taken, which is periodic in z-direction only. 1x1x4 uniform k-point mesh is considered to sample the whole system and 1x1x12 k-point for the projected density of states (pDOS) calculations. The atoms are allowed to be relaxed fully under the convergence threshold of 10^{-4} eV on total energy and 10^{-3} eV on forces on each atom.

2.5 Electrochemical Measurements

All the electrochemical measurements were done using Autolab PGSTAT-12 Potentiostat/Galvanostat connected with Metrohm RDE-2 rotor. HER experiments were done using rotating disc electrode (RDE) and various voltametery techniques. Glassy carbon rotating disc electrode was polished by rubbing it gently on the polishing cloth along with alumina powder of 0.05 um. This was then rinsed with copious amount of Milli Q water and was sonicated in Milli Q water for approximately 10 sec. The electrode was dried in open air for 1 hour and made ready for the coating. The catalytic ink was prepared by dispersing 1 mg of **Co_3O_4@Co/NCNT** in 98 µL of Milli Q water and 98 µL of isopropanol (IPA) along with 5 µL of Nafion solution (5wt%, Sigma- Aldrich). This was sonicated for an hour to make a uniform dispersion. 4 uL of this dispersion was dropcasted onto the clean glassy carbon electrode and dried in open air for about an hour. All the electrochemical measurements were done in three electrode system using Ag/AgCl (3M KCl) as the reference electrode; **Co_3O_4@Co/NCNT** coated glassy carbon RDE as the working electrode and Pt coil as the counter electrode. 0.5 M H_2SO_4 was used as the electrolyte and was purged with Ar for 30 minutes to degass the electrolyte. For all the measurements, RDE was rotated at the speed of 1600 RPM to prevent the accumulation of hydrogen gas bubbles evolved onto the electrode surface. All the measurements were carried out at room temperature.

2.6 Zn-Air Battery Tests

All the zinc-air battery tests were carried out in two electrode configuration. The above dispersion was coated onto the carbon fiber paper having an area of 1 cm^2 such that the effective loading was equivalent to 1 mg/cm^2. Zinc foil was used as the anode and **Co_3O_4@Co/NCNT** coated carbon fiber paper as the gas diffusion layer and the cathode. For the rechargeable battery, 6M KOH and 0.2 M zinc acetate was used as the electrolyte. All the solutions were purged with high purity O_2 gas before the measurements.

2.7 Wearable Zn-Air Battery

Wearable Zn-Air battery was fabricated by using carbon fiber cloth as flexible electrodes along with polyvinyl alcohol-polyethylene oxide (PVA-PEO) gel electrolyte as well as a separator. For the anode, electrochemical deposition of zinc was carried out in two electrode configuration by using carbon fiber cloth as the working electrode and high purity Zn foil as both counter and reference electrode. 1 M of $ZnSO_4.7H_2O$ and 1 M of KCl in Milli Q water was used as the electrolyte. Electrochemical deposition of zinc was performed by passing the current equivalent to -10 mA/cm^2 for 90 min. For the fabrication of cathode, above prepared dispersion of **Co_3O_4@Co/NCNT** was coated onto carbon fiber cloth such that the amount of loading is equivalent to 1 mg/cm^2. PVA-PEO gel electrolyte was prepared by adding 1g of polyvinyl alcohol(PVA) and 0.1 g of polyethylene oxide(PEO) to 10 mL of water under stirring for 15 min followed by heating at 95 ^oC along with stirring. After a clear solution was obtained 1 mL of 18 M KOH was added to the hot solution and stirring was continued for another 30 min. The hot transparent solution was then poured into a petridish and was cooled down to -3 °C for 1 hour followed by 1 hour cooling at 0 °C. Then this was brought to room temperature. For the fabrication of wearable battery, PVA-PEO gel was sandwiched between the anode and the cathode.

3. Results and Discussion:

As reported, $\{[Co(bpe)_2(N(CN)_2].(N(CN)_2).5(H_2O)\}_n$ is three dimensional two-fold interpenetrated MOF containing dicyanamide $[(N(CN)_2]$ and bpe (1,2-bis(4-pyridyl)ethane) ligands.[35] Phase purity of as synthesized MOF was confirmed by PXRD (Figure 1a) Carbonization of the framework lead to the formation of core-shell Co_3O_4@Co nanoparticles which were found to be encapsulated in nitrogen doped carbon nanotubes (NCNT). The formation of N doped graphitic matrix, metallic Co, Co_3O_4, Co-N_4 and $Co(CO)_4$ moities were found out from the XPS studies.[35] The phase purity of the as synthesized **Co_3O_4@Co/NCNT** sample was studied by PXRD and Raman spectrum.

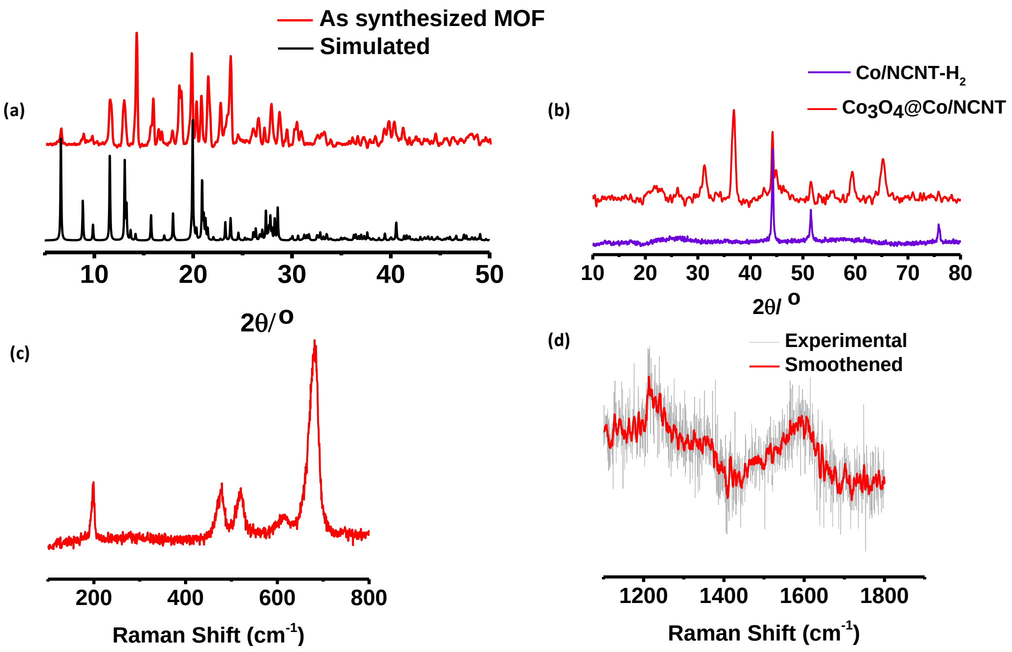

Figure 1: (a) PXRD pattern of the as synthesized MOF and simulated pattern; (b) PXRD patterns of product obtained after carbonization **(Co/NCNT-H_2)** and **Co_3O_4@Co/NCNT;** (c,d) Raman spectra of **Co_3O_4@Co/NCNT.**

The peaks obtained at 44.3°, 51.5°, 75.85° in **Co/NCNT-H_2** correspond to the crystalline phase of Co whereas, peaks at 31.24°, 36.8°, 44.3°, 51.5°, 59.4°, 65.27° and 75.8° and a broad peal at 26° show the formation of **Co_3O_4@Co/NCNT** (Figure 1b). **Co_3O_4@Co/NCNT** was further evaluated by the Raman spectra (Figure 1c,d) which showed characteristic D band and G band. Apart from this, bands at 199, 478, 520, 612, 681 cm^{-1} correspond to the spinel phase of Co_3O_4.[35]

3.1 Electrocatalytic studies:

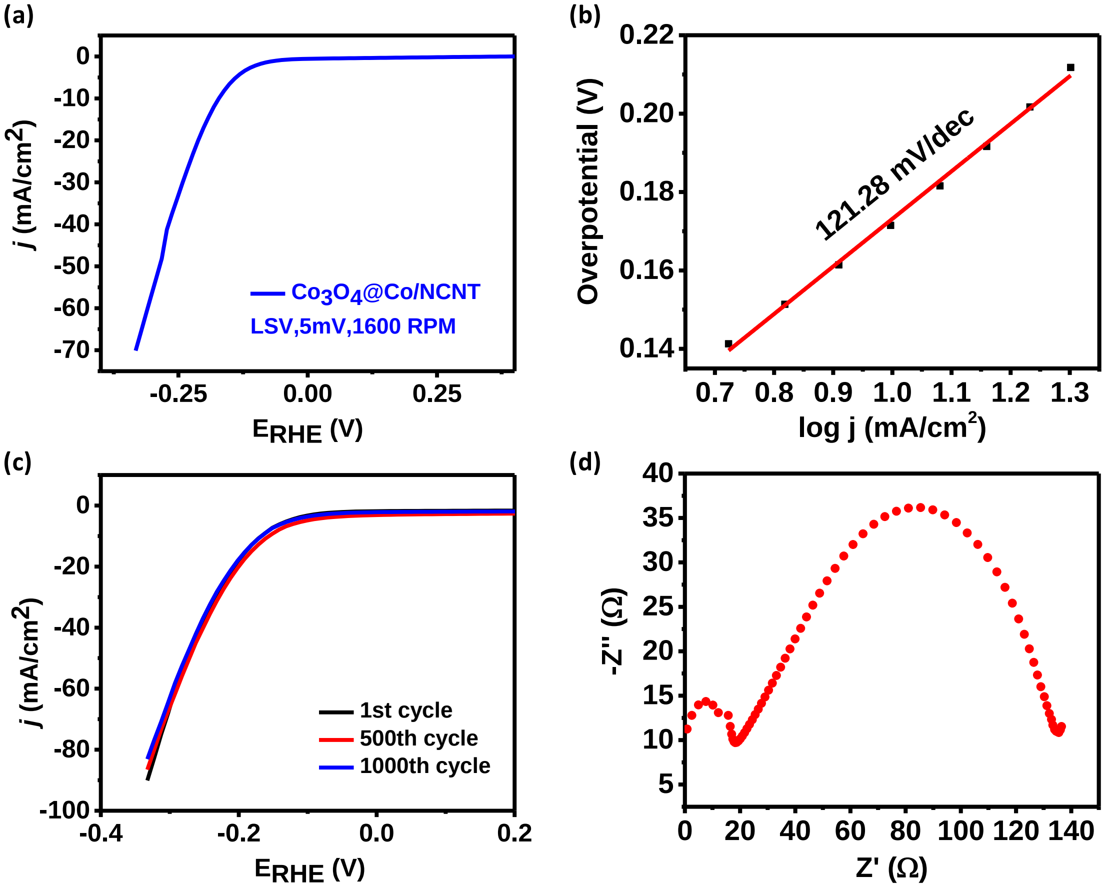

Figure 2: (a) LSV showing HER activity of **Co_3O_4@Co/NCNT;** (b) Tafel Plot; (c) Cycling stability; (d) Electronic impedance spectrum.

The potential of the as synthesized sample **Co_3O_4@Co/NCNT** for electrocatalytic hydrogen evolution reaction was studied by coating the sample on glassy carbon electrode in three electrode configuration with Ag/AgCl (3M KCl) as the reference electrode in 0.5 M

H_2SO_4. LSV curves were obtained at the scan rate of 5 mV/sec. All the potentials were converted to reversible hydrogen electrode (RHE) as the reference electrode. LSV curves showed a sharp increase in the cathodic current density on application of negative potential which showed the beginning of HER (Figure 2a). The onset of 81.9 mV for **Co_3O_4@Co/NCNT** was obtained. The extent of polarization on passing current and the efficiency of the catalyst is determined by an important parameter known as overpotential which is generally measured at a current density of 10 mA/cm^2. Low overpotential of 171 mV was obtained for **Co_3O_4@Co/NCNT**. The detailed mechanism and the rate determining step for electrochemical hydrogen evolution can be understood from the tafel slope. Butler-Volmer equation is used to derive the tafel equation and the final form of which can be represented as

$$\eta = a + blog\left(\frac{i}{i_0}\right)$$

Where η is the overpotential, i and i_0 are the current and exchange current density respectively, 'b' corresponds to the tafel slope and 'a' is the constant. The kinetics of the reaction is inversely proportional to the tafel slope. Generally the electrochemical HER can proceed through three different mechanisms which is indicated by the tafel slope.

1) $H^+ + \ cat \ + \ e^- \rightarrow cat - H^* \quad (Volmer\ reaction, Tafel\ slope = 120\ mV/dec)$

2) $cat - H^* + \ e^- \rightarrow M + H_2 \quad (Heyrovsky\ reaction, Tafel\ slope = 40\ \ mV/dec)$

3) $2[cat - H^*] \rightarrow 2M + \ H_2 \quad (Tafel\ reaction, Tafel\ slope = 30\ \ mV/dec)$

Where H* is the chemically adsorbed proton on the active site of the catalyst (cat). The Volmer reaction shows the electrochemical adsorption of H^+ onto the catalytic species and is the foremost step. The reaction can proceed through any of the two other steps depending on the value of obtained tafel slope. The Heyrovsky reaction is the rate determining step if tafel slope of 40 mV/dec is obtained. Whereas, the tafel slope of 30 mV/dec indicates the Tafel reaction to be the rate determining step. If the tafel slope of 120 mV/dec is obtained, the Volmer reaction is the slowest step irrespective of the mechanism followed for the hydrogen evolution reaction. The other important parameter obtained from tafel equation is the exchange current density. It can be understood as the current density at an equilibrium potential of the reaction. It should be noted that higher the exchange current density, better is the catalyst. Thus, the tafel slope of 121.28 mV/dec obtained from the tafel plot (Figure 2b) indicates the volmer reaction to be the slowest and high current density of 1.035×10^{-3} A/cm^2 was obtained. Further, a good electrocatalyst should have stability. So, to check the stability of **Co_3O_4@Co/NCNT** multiple LSV cycles were recorded. After 1000 cycles of LSV, very less decrease in current density of 7.7% was observed (Figure 2c). This proves the high stability of **Co_3O_4@Co/NCNT** in acidic medium. Further to find out the active catalytic site in **Co_3O_4@Co/NCNT**, theoretical calculations were performed. Recently, Dang et.al showed that nitrogen doping in carbon matrix along with the transition metals encapsulated in it, promotes hydrogen adsorption due to synergistic effects and thus the hydrogen evolution reaction. Here nitrogen was found out to be binding site for the proton for HER to occur.[36] So to study the binding site in **Co_3O_4@Co/NCNT**, various theoretical calculations were performed. Since the hydrogen evolution reaction (HER) activity of a catalyst in the acidic medium can directly be correlated to the free energy change of the H adsorption (ΔG), the catalytic activity of various systems with respect to ΔG were compared. The electronic adsorption energies at 0 K temperature were obtained through the DFT calculations while the zero point energy correction (ZPE) and entropic effect at finite temperature (300K) were considered from the data of previous reported paper on similar kind of structures. To model such systems, the N substitution from 3.08% to 7.66% was varied with a variance of 1.52%, along with Co-N_4 moiety in all the systems. Since in experimental XPS spectra, there was an additional peak corresponding to the metallic Co, single Co atom and a tetrahedron cluster of 4-Co's inside the CNT ring were considered. As such Co- tetrahedra have been shown to be an important component of HER. To find the binding site for proton, H-adsorption on all the sites in this CNT-CoN_4-Co_4-N_x complexes was explicitly considered. Interestingly, it was found that when the N concentration is small to moderate, the active site for H-adsorption is on Co atom. In fact, Co atom continues to be the active site till N concentration reaches an optimum value. Beyond N concentration of 4.62%, it was found that the active site for H-adsorption changed from Co-site to N-site. A corresponding table (Table 1) with H-adsorption energy, free energy changes as a function of N concentration is given. As can be seen, the free energy change and the adsorption energy change while going from low N concentration to high N concentration, is quite drastic and thus goes from endothermic to exothermic adsorption. Since experimentally also the HER was achieved with high N concentration, it is inferred that the active sites for the HER are the N atoms in the CoN_4 moiety.

Table 1: Showing H-adsorption energy, free energy changes as a function of N concentration

	H on Co (eV)	H on N (eV)	ZPE-TS (eV)	ΔG-Co (eV)	ΔG-N (eV)
10N[Co4]	0.2096731972	-0.4369150467	0.37	0.5796731972	-0.06691504666
8N[Co4]	0.1813813957	0.002482743975	0.37	0.5513813957	0.372482744
6N[Co4]	0.1179395549	0.7123463426	0.37	0.4879395549	1.082346343
4N[Co4]	0.1850802463	0.7407136462	0.37	0.5550802463	1.110713646
4N[no-Co4]	0.1607288236	0.7228595348	0.37	0.5307288236	1.092859535

Further, to study the HER kinetics, electrochemical impedance spectroscopy (EIS) was performed by varying the frequency from 500 kHz to 10 Hz with the AC voltage of 5 mV (Figure 2d). The nyquist plot showed two semicircles which are indicative of two time constant behavior. This type of behavior is generally shown by the core shell materials.[33] As evident from the tafel slope, adsorption of the proton onto the N atom of NCNT is the slowest step. The low frequency semicircle shows the high resistance of 133.7 Ω which can be correlated with the hydrogen adsorption onto the electrode surface to form the proton adsorbed species. Whereas, the high frequency semicircle corresponds to the low resistance of 23 Ω which may be due to the charge transfer resistance. The low charge transfer resistance is likely due to the synergistic interaction between the conductive and metallic Co core and semiconducting Co_3O_4 shell. The high catalytic activity of **Co_3O_4@Co/NCNT** may be due to the less charge transfer resistance. This is also due to the high intrinsic conductivity of NCNT.

As reported, **Co_3O_4@Co/NCNT** was proved to be a potential material to be a bifunctional catalyst for both oxygen reduction and oxygen evolution reaction.[35] For ORR, **Co_3O_4@Co/NCNT** showed an onset of 0.9 V v/s RHE with an overpotential of 0.88 V and a lower Tafel slope of 61mV/dec. From K-L plot, it was found that **Co_3O_4@Co/NCNT** followed 4 electron transfer process. Further from RRDE plot, only 1% of H_2O_2 was calculated. For OER, **Co_3O_4@Co/NCNT** achieved a current density of 10 mA/cm^2 at a potential of 1.61 V which is superior to the benchmark catalysts, RuO_2 and IrO_2, having a potential of 1.64 V and 1.69 V v/s RHE, at the same current density. Also, the lower Tafel slope 58.7 mV/dec showed much faster kinetics than RuO_2, IrO_2, Pt/C having the Tafel slopes of 78.6, 80.7 and 147.8 mV/dec respectively. The low overpotential difference between ORR (current density of -1 mA/cm^2) and OER (current density of 10 mA/cm^2) was 0.73 V and thus proving the bifunctional activity of **Co_3O_4@Co/NCNT**.

3.2 Zinc Air Batteries:

The low onset potential of **Co_3O_4@Co/NCNT** and superior performance towards ORR and OER motivated us to use **Co_3O_4@Co/NCNT** as the cathode material in Zn-air batteries. For the rechargeable battery, 6 M KOH along with 0.2 M zinc acetate was used as the electrolyte along with Zn foil as the anode.

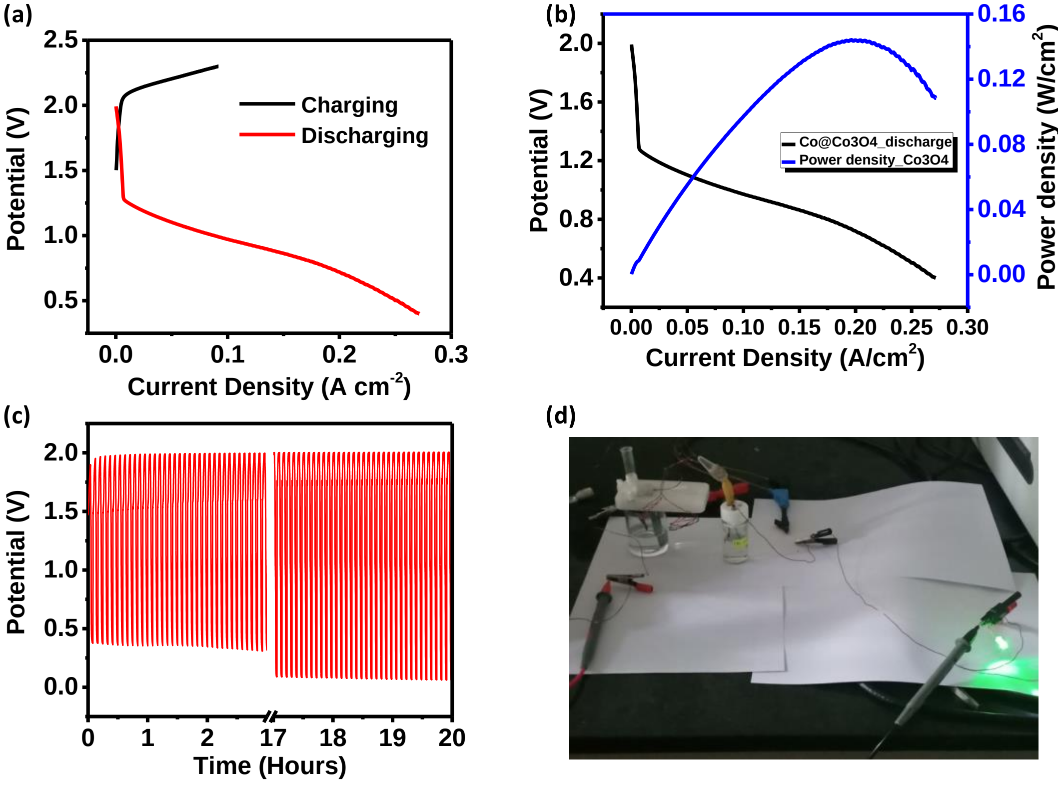

Figure 3: (a) Galvanodynamic charge-discharge curve; (b) Power density curve; (c) Cycling stability at 5mA/cm^2; (d) Optical image showing glowing bright green LED powered by two Zn-air batteries in series.

High open circuit potential of ~1.35 V was obtained on fabricating the battery. The battery showed high current density of 200 mA/cm^2 and high power density of 144 mW/cm^2 (Figure 3a,b). Motivated by the good initial performance of **Co_3O_4@Co/NCNT** as the cathode material, the robustness of **Co_3O_4@Co/NCNT** in Zn-air batteries was studied by galvanostatic charge discharge (Figure 3c). The cycling stability was performed at a current density of 5 mA/cm^2 for 20 hours. This showed that the difference between the charged and discharged potential changed by 0.2 V after cycling for 24 hours. This change may be due to the use of single electrode for both charging and discharging the battery and thus the carbon oxidation during OER which may cause the loss of active sites.[23, 29] But the key challenge is the realization of these lab scale devices to the macroscopic world. So various applications of zinc air batteries with **Co_3O_4@Co/NCNT** as cathode material are shown. To fulfill the energy requirements, the cells can be joined in series or parallel to obtain the required voltage or the current. So as a demonstration two cells were joined in series to light up a bright green LED as shown in the Figure 3d. As the demand of flexible and wearable electronics is rising at a fast pace, there is need to develop robust, reliable, low cost and wearable energy storage devices with high performance. So as an another application, to fill the gap between the laboratory scale and materialistic world, here, to the best of our knowledge, we first time show the application of zinc air batteries as a wearable battery with MOF derived porous material as cathode. This was realized by the development of both the anode and cathode as the flexible electrodes and by using PVA-PEO gel electrolyte instead of the liquid electrolyte in conventional Zn-air batteries. Flexible zinc electrode, as an anode, was fabricated onto a conducting carbon cloth by the electrodeposition of zinc (Figure 4b) from a zinc metal foil at a current density of -10 mA/cm^2. The electrodeposited zinc metal was characterized by PXRD and was compared to the PXRD pattern of the blank carbon paper and the simulated pattern (Figure 4a). The phase purity of electrodeposited zinc was confirmed as all the peaks matched with zinc base peaks (PDF:04-0831). The sharp peak at 2θ value of 18.16^o and a broad peak at 25.68^o corresponded to that of the carbon cloth. Further, **Co_3O_4@Co/NCNT** was coated onto another carbon cloth. The PVA-PEO gel electrolyte was sandwiched between the anode and cathode. Thus, the PVA-PEO gel acted both as the electrolyte as well as the separator between the two electrodes. This gave the OCP of 0.8 V as shown in Figure 4c). To demonstrate the wearable nature of the battery, various tests such as tailoring test, flexible nature and hole test were performed. Figure 4d shows the tailoring test in which the battery was sewed with the thread but maintaining the nature of the battery and showing the OCP of 0.67 V. The small decrease in the voltage of the battery is assumed to be due to the short circuit during the tailoring test as metallic needle was used for the experiment.

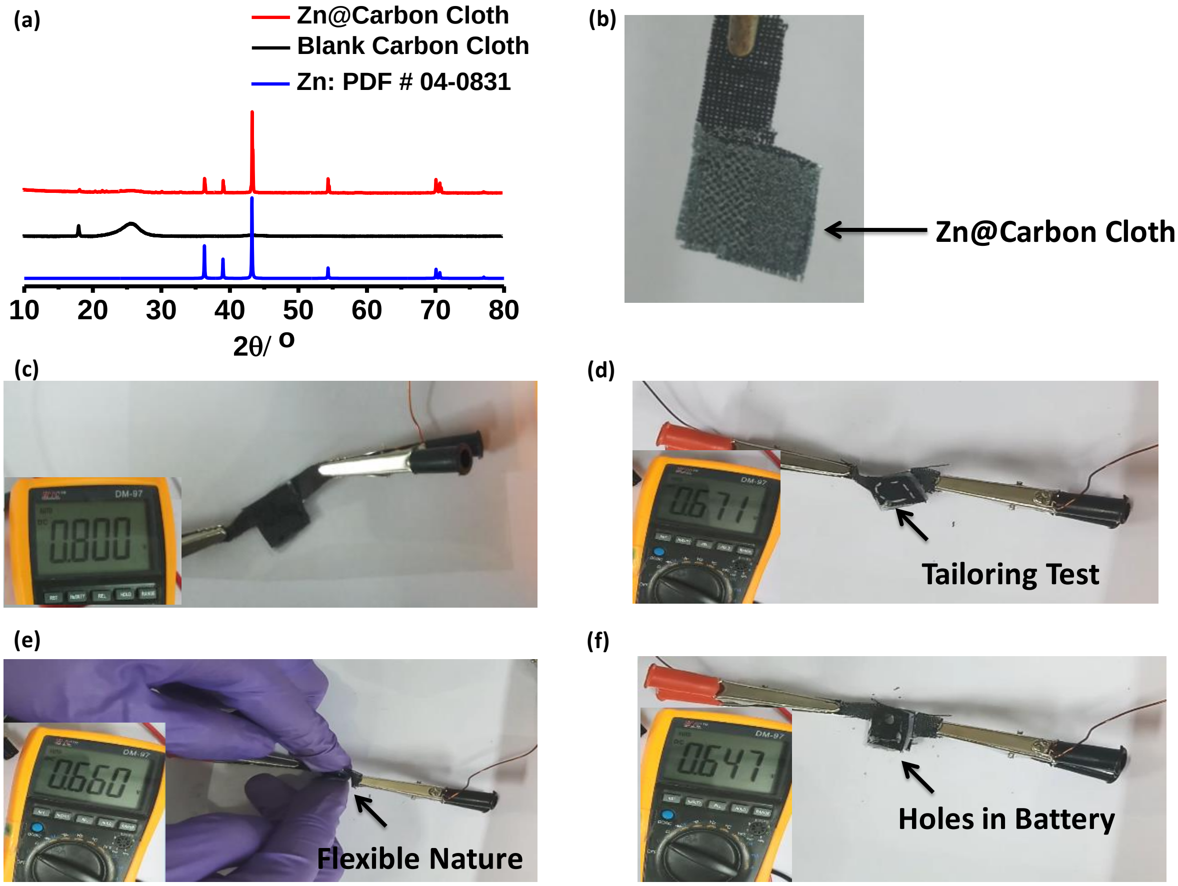

Figure 4: (a) PXRD pattern of electrochemically coated Zn, blank carbon cloth and simulated pattern of Zn; (b) Optical image of electrochemically deposited Zn; (c) Optical image showing the OCP of wearable battery on just fabrication of the battery; (d) Tailoring test; (e) Flexible nature; (f) Hole test. (inset in all the images shows the OCP after the test is performed.

The stitched battery was then made to undertake the flexibility test (Figure 4e). The battery was bent by more than 90°. The bent battery showed almost the same OCP as of the previous test. Moreover, to show that the battery can be cut and casted into different shapes, hole test was performed (Figure 4f). For this test, holes were made into the battery with a paper punch. It was seen that the battery retained almost its original performance even after the incorporation of the holes in the battery. To show realization of the battery performance under stressed conditions and fulfill the energy requirements, three batteries were folded at an angle of approximately 140^o and connected in series to successfully light up a standard green LED as shown in Figure 5.

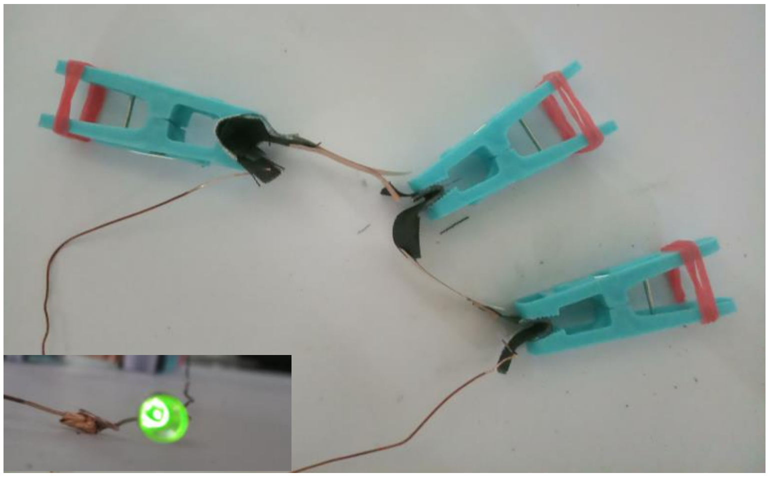

Figure 5: Optical image of glowing LED powered by three flexible wearable batteries under stressed condition, connected in series.

3.3 Self-Powered Overall Water Splitting

As shown, **Co_3O_4@Co/NCNT** is a trifunctional catalyst, to study its application in overall water splitting, a two compartment (H-type) cell was used as the water electrolyser (Figure 6) by using **Co_3O_4@Co/NCNT** as both water oxidation catalyst (anode material) in 0.1 M KOH and water reduction catalyst (cathode material) in 0.5 M H_2SO_4. The two compartments were separated by a proton exchange membrane (Nafion117).[37]As the OCP of a single zinc-air battery was found out to ~1.35 V, which was not sufficient to drive the water splitting reaction. So two zinc-air batteries (fabricated above), with the **Co_3O_4@Co/NCNT** as the cathode material, were connected in series (resulting in potential difference of 2.7 V) to power the water electrolyzer and thus the self-powered overall water splitting (Figure 6a). To study the efficiency of the system, LSV was recorded in two electrode configurations by coating **Co_3O_4@Co/NCNT** onto two glassy carbon electrodes (Figure 6b). The maximum current density of 14 mA/cm^2 was found at the potential of 2.3 V beyond which the graph saturated because of the formation of bubbles on the surface of the electrode. So, excitingly, a non noble metal, highly conducting NCNT doped core/shell trifunctional catalyst was proved to be a potential material for the use in water electrolyzers and thus the efficient water splitting as shown in Figure 6c.

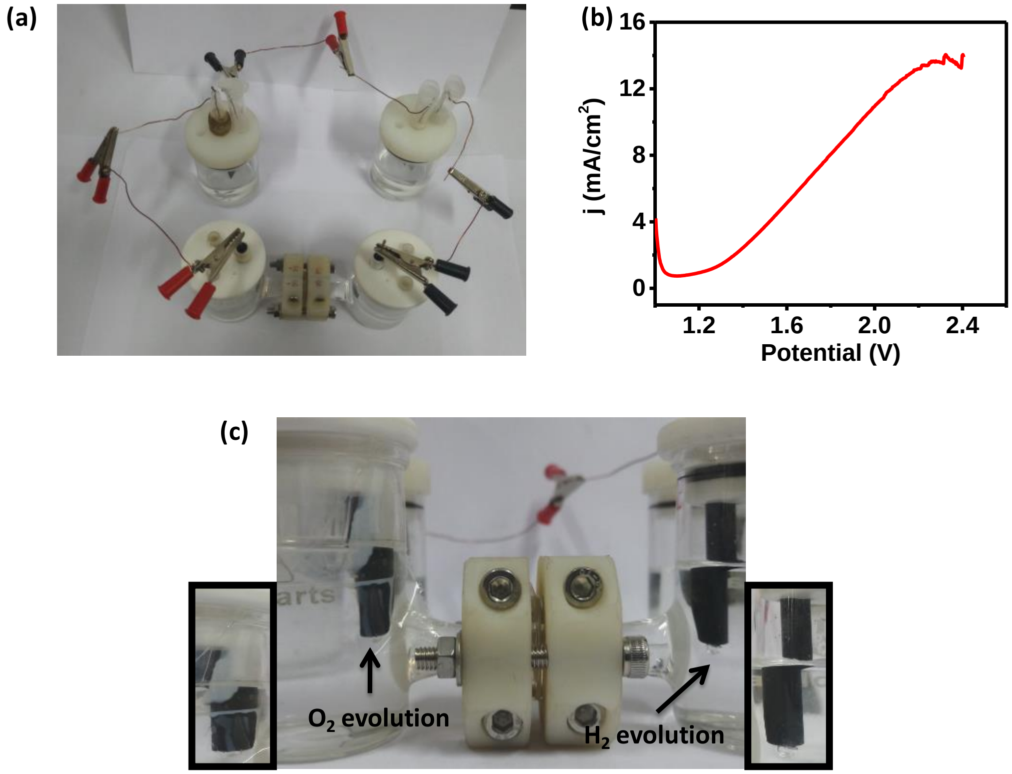

Figure 6: (a) Optical image showing two Zn-air batteries connected to water elctrolyser; (b)LSV curve obtained in two electrode configuration of water electrolyser with **Co_3O_4@Co/NCNT** as both anode and cathode; (c) Optical image showing H-type cell as water electrolyser and showing the evolution of O_2 and H_2 gas (side images show the magnified images of the gas evolved on two electrodes).

4. Conclusion

In conclusion, herein we report core-shell Co_3O_4@Co encapsulated in nitrogen doped carbon nanotubes(NCNT) as an efficient electrocatalyst for hydrogen evolution reaction with low onset and overpotential. The material was already known to possess bifunctionality for ORR and OER. **Co_3O_4@Co/NCNT** was proved to be an efficient material for Zn-air battery with high power density of 140 mW/cm^2 and high stability. Moreover, an all solid-state wearable battery was successfully fabricated by the chemical electrodeposition of Zn onto the carbon cloth along with PVA/PEO gel with 18 M KOH as the electrolyte and separator. The wearable battery retained its OCP even under the extremely stressed conditions. This being a trifunctional material was used as the catalyst for water oxidation and reduction in water electrolyser, which was powered by the Zn-air battery fabricated by utilizing **Co_3O_4@Co/NCNT** as the cathode material.

5. References

1. B. Panella, M. Hirscher, H. Pütter and U. Müller, *Adv. Funct. Mater.*, 2006, **16**, 520.
2. S. S. Han, W.-Q. Deng and W. A. Goddard Iii, *Angew. Chem. Int. Ed.*, 2007, **46**, 6289.
3. Y. H. Hu and L. Zhang, *Adv. Mater.*, 2010, **22**, E117.
4. X. Wang, K. Maeda, A. Thomas, K. Takanabe, G. Xin, J. M. Carlsson, K. Domen and M. Antonietti, *Nat. Mater.*, 2008, **8**, 76.
5. Q. Lu, Y. Yu, Q. Ma, B. Chen and H. Zhang, *Adv. Mater.*, 2016, **28**, 1917.
6. Y. Shi and B. Zhang, *Chem. Soc. Rev.*, 2016, **45**, 1529.
7. Q. Zhang, W. Wang, J. Zhang, X. Zhu, Q. Zhang, Y. Zhang, Z. Ren, S. Song, J. Wang, Z. Ying, R. Wang, X. Qiu, T. Peng and L. Fu, *Adv. Mater.*, 2018, **30**, 1707123.
8. H. Zhang, L. Yu, T. Chen, W. Zhou and X. W. Lou, *Adv. Funct. Mater.*, 2018, **28**, 1807086.
9. J. Kibsgaard, C. Tsai, K. Chan, J. D. Benck, J. K. Nørskov, F. Abild-Pedersen and T. F. Jaramillo, *Energy Environ. Sci.*, 2015, **8**, 3022.
10. M.-Q. Wang, C. Ye, H. Liu, M. Xu and S.-J. Bao, *Angew. Chem. Int. Ed.*, 2018, **57**, 1963.
11. D. Y. Chung, J. W. Han, D.-H. Lim, J.-H. Jo, S. J. Yoo, H. Lee and Y.-E. Sung, *Nanoscale*, 2015, **7**, 5157.
12. H. Wang, C. Tsai, D. Kong, K. Chan, F. Abild-Pedersen, J. K. Nørskov and Y. Cui, *Nano Res.*, 2015, **8**, 566.
13. C. N. R. Rao and M. Chhetri, *Adv. Mater.*, 2018, **0**, 1803668.
14. P. Gu, M. Zheng, Q. Zhao, X. Xiao, H. Xue and H. Pang, *J. Mater. Chem. A*, 2017, **5**, 7651.
15. X. Liu, L. Wang, P. Yu, C. Tian, F. Sun, J. Ma, W. Li and H. Fu, *Angew. Chem. Int. Ed.*, 2018, **57**, 16166.

16. A. Sivanantham, P. Ganesan, L. Estevez, B. P. McGrail, R. K. Motkuri and S. Shanmugam, *Adv. Energy Mater.*, 2018, **8**, 1702838.
17. Y. Lian, H. Sun, X. Wang, P. Qi, Q. Mu, Y. Chen, J. Ye, X. Zhao, Z. Deng and Y. Peng, *Chem. Sci.*, 2019, **10**, 464.
18. F. Yu, H. Zhou, Y. Huang, J. Sun, F. Qin, J. Bao, W. A. Goddard, S. Chen and Z. Ren, *Nat. Commun.*, 2018, **9**, 2551.
19. X. L. Tian, L. Wang, B. Chi, Y. Xu, S. Zaman, K. Qi, H. Liu, S. Liao and B. Y. Xia, *ACS Catal.*, 2018, **8**, 8970.
20. P. Tan, B. Chen, H. Xu, W. Cai, W. He, M. Liu, Z. Shao and M. Ni, *Small*, 2018, **14**, 1800225.
21. D. Zhou, Z. Cai, X. Lei, W. Tian, Y. Bi, Y. Jia, N. Han, T. Gao, Q. Zhang, Y. Kuang, J. Pan, X. Sun and X. Duan, *Adv. Energy Mater.*, 2018, **8**, 1701905.
22. J. Xie, H. Qu, F. Lei, X. Peng, W. Liu, L. Gao, P. Hao, G. Cui and B. Tang, *J. Mater. Chem. A*, 2018, **6**, 16121.
23. Y. Guo, P. Yuan, J. Zhang, Y. Hu, I. S. Amiinu, X. Wang, J. Zhou, H. Xia, Z. Song, Q. Xu and S. Mu, *ACS Nano*, 2018, **12**, 1894.
24. T. V. Vineesh, M. P. Kumar, C. Takahashi, G. Kalita, S. Alwarappan, D. K. Pattanayak and T. N. Narayanan, *Adv. Energy Mater.*, 2015, **5**, 1500658.
25. Z. Xiao, G. Xiao, M. Shi and Y. Zhu, *ACS Appl. Mater. Interfaces*, 2018, **10**, 16436.
26. L. Li, L. Song, H. Guo, W. Xia, C. Jiang, B. Gao, C. Wu, T. Wang and J. He, *Nanoscale*, 2019, **11**, 901.
27. R. Li, Z. Wei and X. Gou, *ACS Catal.*, 2015, **5**, 4133.
28. M. Zeng, Y. Liu, F. Zhao, K. Nie, N. Han, X. Wang, W. Huang, X. Song, J. Zhong and Y. Li, *Adv. Funct. Mater.*, 2016, **26**, 4397.
29. T. Wang, Z. Kou, S. Mu, J. Liu, D. He, I. S. Amiinu, W. Meng, K. Zhou, Z. Luo, S. Chaemchuen and F. Verpoort, *Adv. Funct. Mater.*, 2018, **28**, 1705048.
30. I. S. Amiinu, X. Liu, Z. Pu, W. Li, Q. Li, J. Zhang, H. Tang, H. Zhang and S. Mu, *Adv. Funct. Mater.*, 2018, **28**, 1704638.
31. Y. Li, B. Jia, Y. Fan, K. Zhu, G. Li and C.-Y. Su, *Adv. Energy Mater.*, 2018, **8**, 1702048.

32. J. Liu, D. Zhu, C. Guo, A. Vasileff and S.-Z. Qiao, *Adv. Energy Mater.*, 2017, **7**, 1700518.
33. X. Yan, L. Tian, M. He and X. Chen, *Nano Lett.*, 2015, **15**, 6015.
34. Y. Jia, L. Zhang, A. Du, G. Gao, J. Chen, X. Yan, C. L. Brown and X. Yao, *Adv. Mater.*, 2016, **28**, 9532.
35. N. Sikdar, B. Konkena, J. Masa, W. Schuhmann and T. K. Maji, *Chem. Eur. J.*, 2017, **23**, 18049.
36. J. Deng, P. Ren, D. Deng, L. Yu, F. Yang and X. Bao, *Energy Environ. Sci.*, 2014, **7**, 1919.
37. J. Yin, P. Zhou, L. An, L. Huang, C. Shao, J. Wang, H. Liu and P. Xi, *Nanoscale*, 2016, **8**, 1390.

Chapter 4

Realization of Bifunctional (ORR and OER) Electrocatalytic Activities by In-Situ Stabilization of Co Nanoparticles in Electroactive Conjugated Microporous Polymer

Abstract

The development of a bifunctional electrocatalyst for energy storage and conversion is among the holy grails of chemistry. This chapter discusses the design, synthesis and application of a redox-active donor-acceptor conjugated microporous polymer (CMP) **TPA-NDI** which consists of tris(4-ethynylphenyl)amine (**TPA**) as the node and dibromo-napthalenediimide (**NDI**) as the linker. **TPA-NDI** possessed bifunctional electrocatalytic activities which include oxygen reduction (ORR) and hydrogen evolution reactions (HER). Further, cobalt nanoparticles were in-situ stabilized in **TPA-NDI** polymer. The nanocomposite **Co@TPA-NDI** acts as an efficient water oxidation catalyst (OER). The bifunctional (ORR and OER) electrocatalytic activities of **Co@TPA-NDI** CMP were further exploited as a cathode material for Zn-air batteries. Moreover, the presence of HER and OER helped to perform overall water splitting reaction which was powered by the two Zn-air batteries fabricated from the **Co@TPA-NDI** as the cathode. DFT studies showed nitrogen as the binding site for proton to show HER activity. To further elucidate the mechanism of HER, another CMP was designed and synthesized which lacked nitrogen and thus did not show HER activity. It is believed that the approach followed to develop a fully conjugated bifunctional organic porous material, possessing good stability, will open up a new branch of bifunctional materials not only for Zn-air batteries but in general all metal-air batteries and water electrolysis.

1. Introduction:

The world population is increasing day by day and so does the energy requirement.[1-3] In this scenario, it is the need of the hour to develop energy generation and storage devices as an alternative to the fossil fuels such as fuel cells, efficient and safe batteries.[3-5] Li-ion batteries are being used widely on commercial basis but have certain disadvantages such as limited availability of lithium, high cost and safety concerns.[6, 7] As an alternative to this, in recent years, metal-air batteries were developed which are attractive candidates for future electric vehicles. Zinc metal being abundant in nature, having low cost[7-9] and environment friendly[10, 11] is a good option to utilize as an anode material in metal air batteries. So the Zn-Air batteries are expected to be next generation energy storage devices.[8] For the development of electrically rechargeable Zn-air battery, a bi-functional material capable of both oxygen evolution and oxygen reduction reaction is required.[12] The state-of-the-art materials such as Pt/C and IrO_2 for oxygen reduction reaction (ORR) and oxygen evolution reaction (OER) catalysts respectively, can be employed as the cathode materials. But their high cost and scarcity limits their use for large scale application.[13, 14] ORR, in which the molecular oxygen is being converted to OH^-, is a kinetically sluggish reaction which limits its utilization in daily life applications.[15] So to improve its kinetics, many noble metal-based catalysts have been developed. The opposite reaction of ORR is OER, which involves the breaking of the O-H bond and the formation of O=O, is also very important reaction for electrically recharging the battery.[16] Thermodynamically, 1.23 V v/s RHE is required to carry out this reaction, but practically it is a more energy consuming process and requires much more potential.[17] So to reduce the overpotential, development of cheap, efficient and robust catalyst is important. Many MOF derived materials and B, N and non-noble metal doped carbon materials are being used as a bifunctional catalyst for Zn- air batteries.[8, 18-20] But these materials lack porosity which is essential for the construction of the air cathode. So development of porous materials with large surface area, possessing bi-functionality and thus being used as air cathode in metal air batteries would be a good start. The porous nature of the material will allow the diffusion of oxygen to and back from the catalytic sites. As the need for flexible and wearable electronics is rising day by day, there is a strong need for the development of a flexible battery. The material can be coated onto a flexible conducting substrate along with solid electrolyte, and thus lead to the development of all solid state flexible battery.[21-23] On the other hand, water-alkali electrolyser requires oxygen evolution and hydrogen evolution reaction (HER) simultaneously on both the electrodes. This would lead to development of green, renewable source of energy.[24] Developing a metal free catalyst capable of ORR and HER, and upon in-situ nanoparticles stabilization for ORR and OER is among the holy grails in chemistry to research upon.

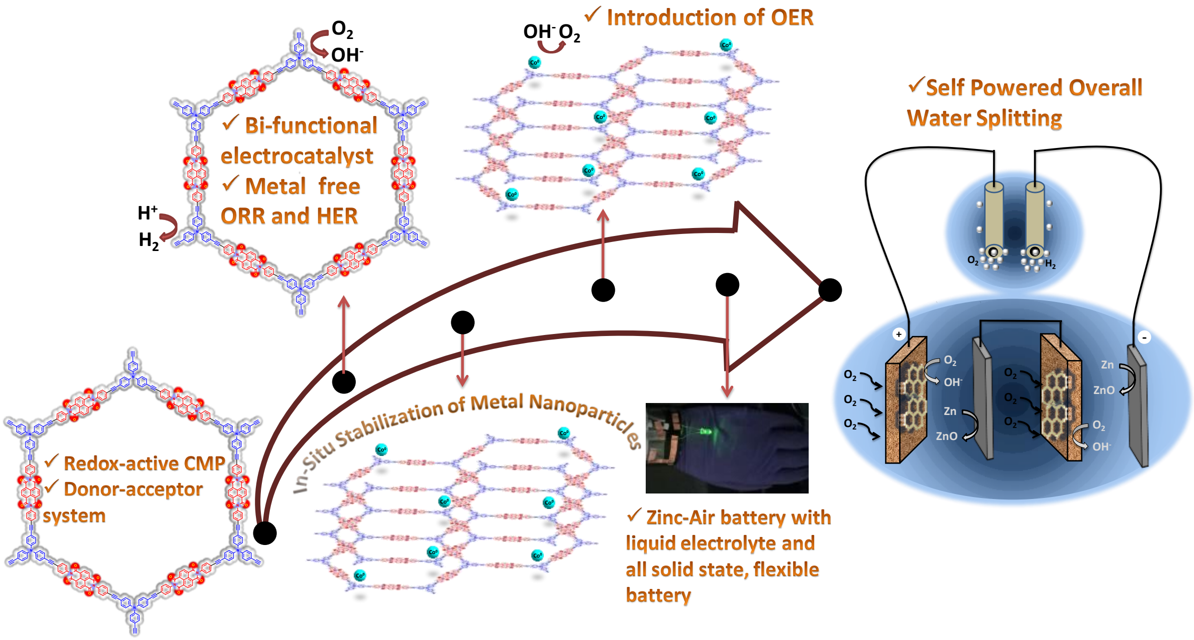

Scheme 1: Schematic showing overview of the chapter.

Keeping in mind the need of such catalyst for Zn-air batteries and overall water splitting, here, conjugated microporous polymer is uniquely designed in order to achieve the desired properties. The design included the redox active donor tris(4-ethynylphenyl)amine (**TPA**) and acceptor dibromonapthalenediimide (**NDI**) molecules as node and spacer respectively which being fully π- conjugated provided a conducting structure required for the electrocatalysis. This being formed by the C-C coupling reactions, provide rigid framework and permanent porosity (**TPA-NDI**). Moreover, **TPA** was carefully chosen as a donor moiety because the closely spaced N atoms acted as an oxygen and proton binding site for ORR and HER activity respectively, as revealed by DFT calculations. So this introduces **TPA** containing materials as a new class of materials for HER. Moreover **TPA-NDI** could also provide a good platform for in-situ metal reduction and stabilization of nanoparticles to develop **Co@TPA-NDI** nanocomposite material. **Co@TPA-NDI** CMP possessed all the requirements needed for the metal air battery. So a primary and mechanically rechargeable, and a secondary Zn-air battery was successfully constructed with assynthesized and cobalt doped CMPs, respectively. Further, **TPA-NDI** and **Co@TPA-NDI** were used as anode and cathode materials, respectively in water electrolyzer powered by two Zn-air batteries fabricated above and thus showing self powered overall water splitting. Scheme 1 shows the overview of the chapter.

2. Experimental Section

2.1. Materials

All the chemicals were purchased from Sigma- Aldrich or TCI and were used without any further purification. All the solvents were dried using standard procedures.

2.2. Synthesis

2.2.1 Synthesis of Tris(4-ethynylphenyl)amine (TPA)

TPA was prepared by the Sonogashira coupling reaction between tris(4-bromophenyl)amine (2g, 4.14mmol) and trimethylsilylacetylene (4.87 g, 49.68 mmol) using $Pd(PPh_3)_2Cl_2$ (0.873 g, 1.24 mmol) and CuI (0.224 g, 2.48 mmol) as catalyst in 10 mL of triethylamine and 30 mL of dry THF in inert atmosphere. The mixture was stirred at 75 ^{o}C for 12 hours. The mixture was cooled to room temperature. To ensure the coupling on all three sides of **TPA**, $Pd(PPh_3)_2Cl_2$ (0.290g, 0.414mmol), CuI(0.075g, 0.828 mmol) and trimethylsilylacetylene (3.5 mL, 24.84 mmol) were again added to the above reaction mixture. This was again stirred at 75 ^{o}C for 12 hours. The trimethylsilyl protected product was purified by column chromatography (Eluent: 100% PE), followed by the desilylation by K_2CO_3 in 10 mL of methanol. The desilylated product was again purified by column chromatography to obtain the pure product. The product was characterized by ^{1}H NMR spectrum (Figure 1). Yield: 60 %; ^{1}H NMR (400 MHz, $CDCl_3$) δ = 3.05 (s, 3H), 7 (d, 6H), 7.38 (d, 6H).

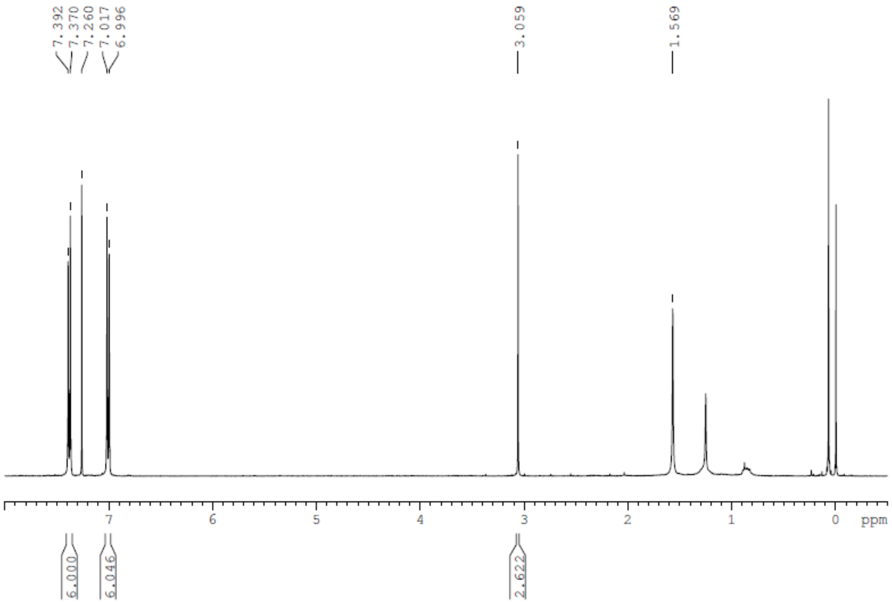

Figure 1: ^{1}H NMR spectrum of **TPA**.

2.2.2 Synthesis of Dibromonaphthalenediimide (NDI)

Dibromonaphthalenediimide (**NDI**) was prepared by the reaction of naphthalene diimide(500 mg, 1.86 mmol) with 4-bromoaniline(653.7 mg, 3.8 mmol) by stirring at 140 ^oC using dry DMF as a solvent overnight. The reaction was done under inert conditions. After the completion of the reaction, the flask was brought at room temperature and then cooled in the water-ice bath for precipitation to occur. The reaction mixture was filtered out and washed with a small amount of chloroform and acetone. The product was dried in vacuum. The product was characterized by ^{1}H NMR spectrum (Figure 2). Yield: 80%. ^{1}H NMR (400 MHz, DMSO-d_6) δ = 7.45 (d, 4H), 7.77 (d, 4H), 8.72 (s, 4H).

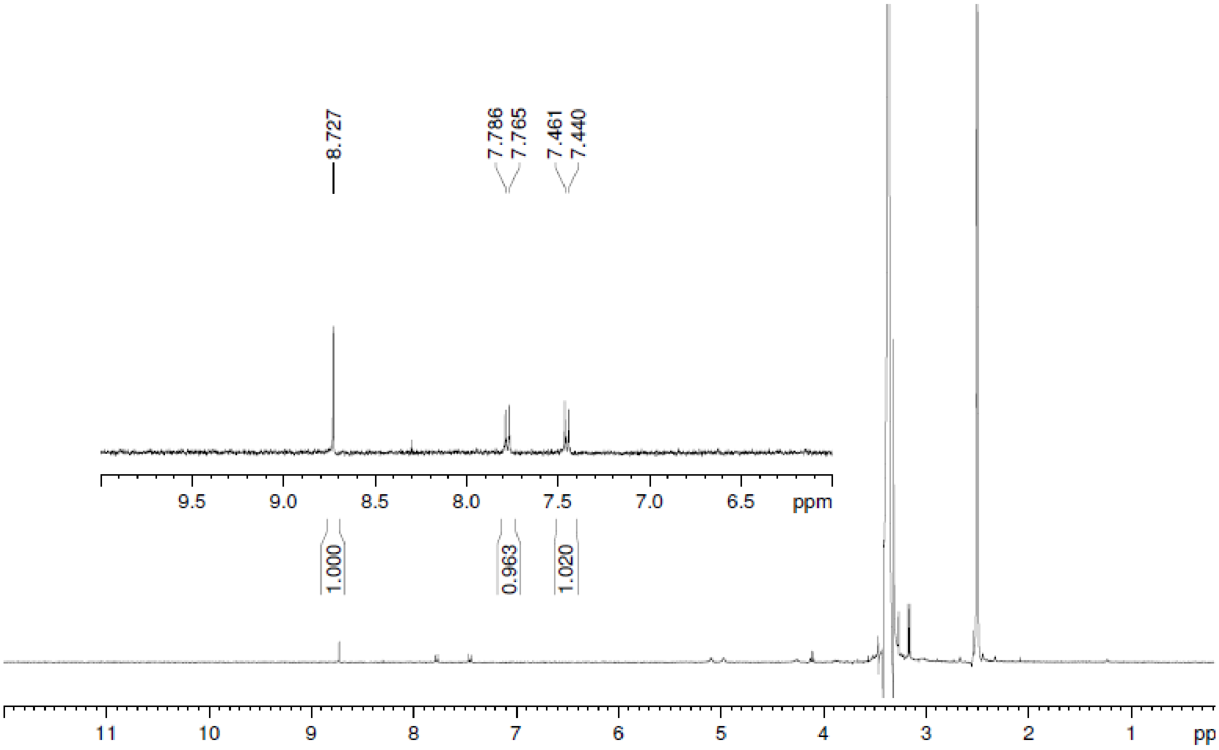

Figure 2: ^{1}H NMR spectrum of **NDI**.

2.2.3 Synthesis of TPA-NDI conjugated microporous polymer

TPA and **NDI** were further used in the preparation of CMP (**TPA-NDI**), using the Sonogashira coupling reaction. **TPA** (29 mg, 0.09 mmol) was reacted with **NDI** (77.77mg, 0.135 mmol) using 8 mg of Pd(0), 3 mg of CuI, 5 mL of dry DMF and 1.5 mL of triethylamine in inert atmosphere. The reaction mixture was stirred at 140 ^oC for 48 hours. The product formed was filtered out and washed with ethanol and acetone. The product was purified by Soxhlet extraction in THF, chloroform and methanol for one day in each solvent. Further to remove the presence of unreacted **NDI** and Pd, **TPA-NDI** polymer was stirred in DMF for 3 days at 60 ^oC changing the DMF solution after every 24 hours. This was then filtered and washed well with ethanol and acetone.

2.2.4 In-situ Stabilization of Cobalt Nanoparticles:

2.5 mg of $CoCl_2.H_2O$ was dissolved in 10 mL of acetonitrile. 10 mg of the activated **TPA-NDI** polymer was added and stirred overnight at room temperature. This was then washed twice with 10 mL of acetonitrile in order to remove the excess of unreacted Co salt. The obtained product was dried at 60 ^{o}C.

2.2.5 Synthesis of 1,3,5-triethnylbenzene (TBA)

1,3,5-tribromobenzene (2g, 6.3 mmol) was reacted with trimethylsilylacetylene (**TMSA**)(10.72 ml, 75.6 mmol) along with catalysts $Pd(PPh_3)Cl_2$ (1.32g, 1.89 mmol) and CuI (0.719 g, 3.78 mmol) in deoxygenated and dry THF (35 mL) and triethylamine (11.66 mL) at 75 ^{o}C for 12 hours. After 12 hours the reaction was cooled to room temperature. To ensure the coupling on all the three sides of TBA, 1/3 rd of the catalysts and 5-7 ml of **TMSA** were added. The same was repeated again after 12 hours. The product was purified by column chromatography and then desilylated with K_2CO_3 in methanol. It was again purified by column chromatography after the desilylation. The product was characterized by ^{1}H NMR spectrum (Figure 3). Yield: 55 %; ^{1}H NMR (400 MHz, $CDCl_3$) δ = 3.1 (s, 3H), 7.56 (s, 3H).

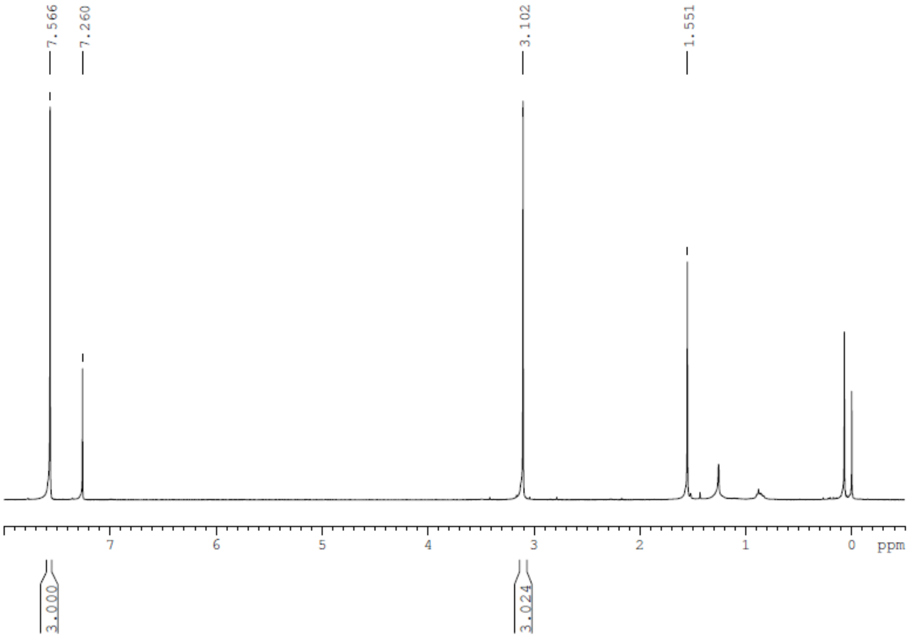

Figure 3: ^{1}H NMR spectrum of **TBA**.

2.2.6 Synthesis of TBA-NDI Conjugated Microporous Polymer:

TBA (13.5 mg, 0.09 mmol) was made to react with **NDI** (77.77 mg, 0.135 mmol) in the presence of 8mg Pd(0) catalyst, 3mg CuI and degassed anhydrous DMF/ethylamine in the ratio of 5/1.5 at 140 °C for 48 hours. After 48 hr of reaction, the reaction mixture was filtered and washed with ethanol and acetone. It was purified by soxhlation process using THF as a solvent for 2 days and chloroform for 1 day. No colour change in the solvent was observed.

2.3 Physical Measurements

Infrared spectra were recorded in transmittance mode by making KBr pellets in Bruker FT-IR spectrophotometer. The thermal stability was measured with Mettler Toledo TGA 850 instrument in N_2 atmosphere and at a scan rate of 5 °C/min and the temperature was varied from 25 °C to 700 °C. Powder X-Ray diffraction of the sample was studied using Bruker D8 discover instrument by varying 2ϴ from 3^o to 60^o. Morphological analysis were performed using Lica-S440I Field Emission Scanning Electron Microscope (FESEM) by drop casting dispersion of the samples in ethanol onto the silicon wafer and captured under high vacuum with an accelerating voltage of 10 kV. The TEM images were captured using JEOL-JEM 3010 microscope at an acceleration voltage of 300 kV and coating the dispersion of the samples on the carbon coated copper grid. Solid state ^{13}C cross-polarization magnetic angle spinning (CP/MAS) NMR spectrum was measured on a Jeol ECX400 spectrometer at a MAS rate of 8 kHz and a CP contact time of 3 ms. ^1H-NMR is recorded on a Bruker AV-400 spectrometer with chemical shifts reported as ppm.

2.4 Adsorption Measurements

Porous nature of the CMPs was studied by adsorption measurements using Quantachrome IQ^2 instrument at 77 K for N_2 and 195 K for CO_2. 100 mg-110 mg of the samples were transferred into an adsorption cell and degassed at 135 °C under a vaccum of $1x10^{-1}$ Pa to empty the pores of the polymer. Helium gas was used to evacuate the chamber and make the system free from any N_2 present. Further all the operations were computer controlled.

2.5 Computational Details

All density functional theory (DFT) computations were performed using Gaussian09 program package.[25] For this, we chose two different model systems, namely model 1 and model 2. Model 1 consists of an **NDI** and a **TPA** unit, whereas model 2 possesses only an

NDI unit. Ground-state geometry optimizations were carried out utilizing B3LYP hybrid functional in conjugation with 6-31+G* basis set. Grimme's d3 dispersion was also used to tackle weak interactions.[26, 27] All the optimized geometries were further verified by frequency analysis. HSEH1PBE/6-31+G* method was employed to evaluate molecular orbital energies.[28] Quadratic convergence (QC) was used for self-consistence field (SCF) calculation in all cases because SCF convergence failed without QC.

2.6 Electrochemical Measurements

Electrochemical measurements were carried out using Autolab PGSTAT12 potentiostat/galvanostat along with Metrohm RDE-2 rotator. The electrochemical activity of the samples were studied using the rotating disc electrode (RDE) and rotating ring disc electrode (RRDE) voltammetery techniques. The glassy carbon rotating disc electrode was polished by rubbing it onto the polishing cloth along with alumina powder (0.05 um mesh). The electrode was then rinsed with MilliQ water followed by ultrasonication in MilliQ water for about 10 second. The electrode was dried in open air and a mirror like shining surface was obtained. The catalytic ink was prepared by dispersing 2.5 mg of compound, 2.5 mg of Vulcan C, 490 uL of IPA and 490 uL of water along with 20 uL of Nafion (5 wt %, Sigma Aldrich). This was then sonicated for about an hour. 5uL of the prepared ink was coated onto the cleaned glassy carbon electrode surface and was dried for 2 hours in the open atmosphere. For ORR and OER, 0.1 M KOH solution was prepared as an electrolyte. All the measurements were done in three electrode configuration with Hg/HgO(1M NaOH) as the reference electrode and the Pt coil as the counter electrode. For OER, the electrolyte was purged with Ar for 30-45 min to remove all the dissolved oxygen. The CV and LSV were recorded at a scan rate of 50 mV/sec and 1600 rpm. For ORR, a CV was recorded in Ar purged electrolyte at a scan rate of 50 mV/sec. To show the ORR catalytic activity, the solution was saturated with oxygen. A CV was recorded at a scan rate of 50mV/sec showing the ORR peak. Further LSV curves were recorded at a scan rate of 10 mV/sec and at different rotation speeds. The RRDE voltammogram was recorded by coating 8 uL of the above dispersion ink on the disc to record the amount of H_2O_2 produced. To calculate the number of electrons involved in the reduction process Koutecký–Levich (K–L) equation was used:

$$\frac{1}{j} = \frac{1}{j_L} + \frac{1}{j_K}$$

$$\frac{1}{j} = \frac{1}{B\omega^{1/2}} + \frac{1}{j_K}$$

$$B = 0.62nFC_0(D_0)^{2/3}\nu^{-1/6}$$

$$j_K = nFkC_0$$

where, j correspond to the measured current density, j_K and j_L correspond to the kinetic and diffusion-limited current densities, ω corresponds to the angular frequency of the RDE in radians per second, n is the number of electrons involved in the reaction, F is the Faraday constant (96485 C mol^{-1}), D_0 is the diffusion coefficient of O_2 in the electrolyte (1.93×10^{-5} $cm^2 s^{-1}$), ν is the kinematic viscosity of the electrolyte (1.01×10^{-2} $cm^2 s^{-1}$), C_0 is the concentration of O_2 in the electrolyte (1.26×10^{-6} mol cm^{-3}) and k is the electron transfer rate constant. To calculate the number of electrons and the amount of H_2O_2 formed during ORR rotating ring disk electrode (RRDE) voltammetry was used which is based on the ratio of the disk and the ring current as shown in the equations given below. For the RRDE experiments, the ring electrode was held at a potential of 0.8 V to oxidize hydrogen peroxide.

$$n_e = \frac{4|I_D|}{|I_D| + \frac{|I_R|}{N}}$$

$$\%H_2O_2 = \frac{\frac{I_R}{N}}{I_D + \frac{I_R}{N}} \times 200$$

Where, N = 0.2678 is the collection efficiency, I_D is the Faradaic disk current, and I_R is the Faradaic ring. For HER 0.5 M H_2SO_4 solution was used as an electrolyte along with Ag/AgCl as the reference electrode and the Pt as the counter electrode. Electrochemical impedance spectroscopy was recorded at the corresponding open circuit potential using an AC perturbation of 10 mV in the frequency range from 300 kHz to 10 Hz. All the recorded potentials were converted to the potentials w.r.t RHE. All the measurements were carried out at room temperature.

2.7 Zinc-Air Battery Tests:

Zn- Air battery was tested in a two electrode system. For the primary battery, catalyst ink was prepared by mixing 2 mg of **TPA-NDI**, 2 mg of Vulcan C in 245 µL of water, 245 µL of IPA and 10 µL of Nafion(5 wt %, Sigma-Aldrich). Effectively 1 mg/cm^2 of the sample was coated on the carbon fiber paper. For the secondary battery, same amount of **Co@TPA-NDI** was used. Zn foil was used as an anode and the **TPA-NDI** (or **Co@TPA-NDI**) as the cathode. For the primary battery 6 M KOH was used as the electrolyte and for the secondary battery, 6 M KOH and 0.2 M Zinc acetate dihydrate was used as the electrolyte. All the solutions were purged completely with O_2 before any measurement.

2.8 Preparation of flexible Zinc air battery:

For the preparation flexible Zn air battery, **Co@TPA-NDI** was coated onto the carbon cloth. PVA/PEO gel was used as an electrolyte. For this, 1g PVA (polyvinyl alcohol) and 0.1g PEO (polyethylene oxide) were dissolved in 10 ml of water at 95 ^{o}C. When the polymers were completely soluble, 1 mL of 18 M KOH was added dropwise along with continuous stirring and heating. The temperature was maintained at 95 ^{o}C for 60 min. The mixture was casted into a petri dish and kept at -3 ^{o}C for 45 min followed by 0 ^{o}C for 60 min. Then it was brought at room temperature and used as it is. For the fabrication of flexible battery, PVA/PEO gel was sandwiched between the carbon cloth and the zinc foil. Copper tape was used to make the terminals.

3. Results and Discussion

3.1 Characterization of TPA-NDI:

As synthesized **TPA-NDI** conjugated microporous polymer (CMP) was characterized with FT-IR, ^{13}C cross polarization magic angle spinning NMR spectroscopy, PXRD, TGA, N_2 and CO_2 adsorption isotherms, FESEM and TEM. FT-IR spectra showed a weak peak at 2164.5 cm^{-1} which corresponded to C≡C bond stretching frequency (Figure 4b). Also a medium intensity band is at 3266.8 cm^{-1} corresponding to ≡C-H was not observed which indicated the presence of **TPA** in **TPA-NDI**.

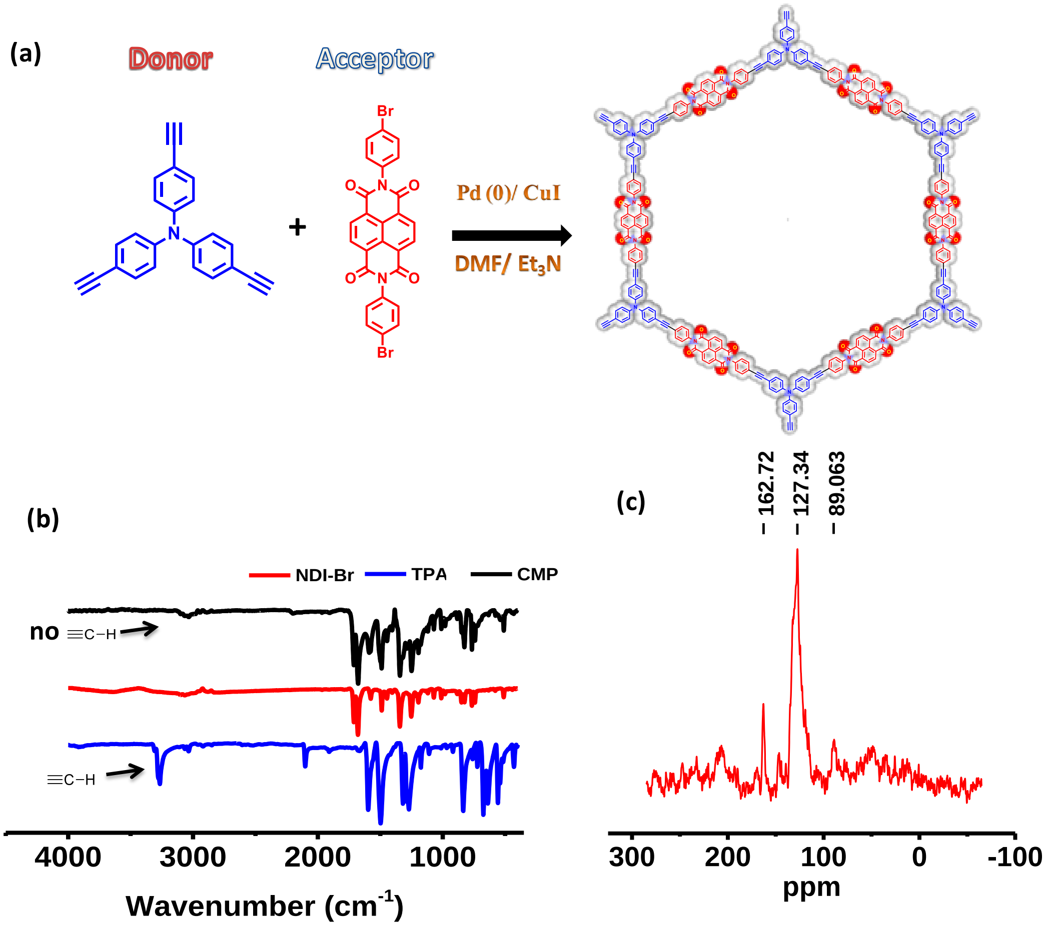

Figure 4: (a) Synthetic scheme; (b) FT-IR spectra (c) ^{13}C Solid state NMR of TPA-NDI.

This was also proved from solid state NMR (Figure 4c) which showed the peaks at 89.06 ppm, 127.34 ppm and 162.72 ppm which corresponded to the acetylene carbon, the aromatic core and the carbonyl carbon respectively and thus confirmed the formation of the desired framework. The PXRD pattern was obtained (Figure 5a) and showed the amorphous nature of the CMP with a broad and low-intensity peak at 2ϴ of 23.21° which corresponded to an interlayer spacing of 3.83 Å. This showed the π-π stacking between the layers of the CMP. Further, TGA profile (Figure 5b) of the as-synthesized CMP, **TPA-NDI** showed that it is stable up to 300°C without any significant weight loss. To study the porosity of the formed framework, **TPA-NDI** was degassed at 135 °C for 6 hours followed by N_2 adsorption at 77K.

This showed a typical type I curve (Figure 5c) with the maximum uptake of 188 cc/g of N_2 and BET surface area was calculated to be 290.649 m^2/g. A step in the desorption curve indicated the microporous and meseoporous nature of the pore in CMP. The pore size distribution by non-linear DFT method showed two types of pores are present having the pore width as 1.19 nm and 4 nm. It can be assumed that the smaller pore is due to the inter layer packing in the CMP.

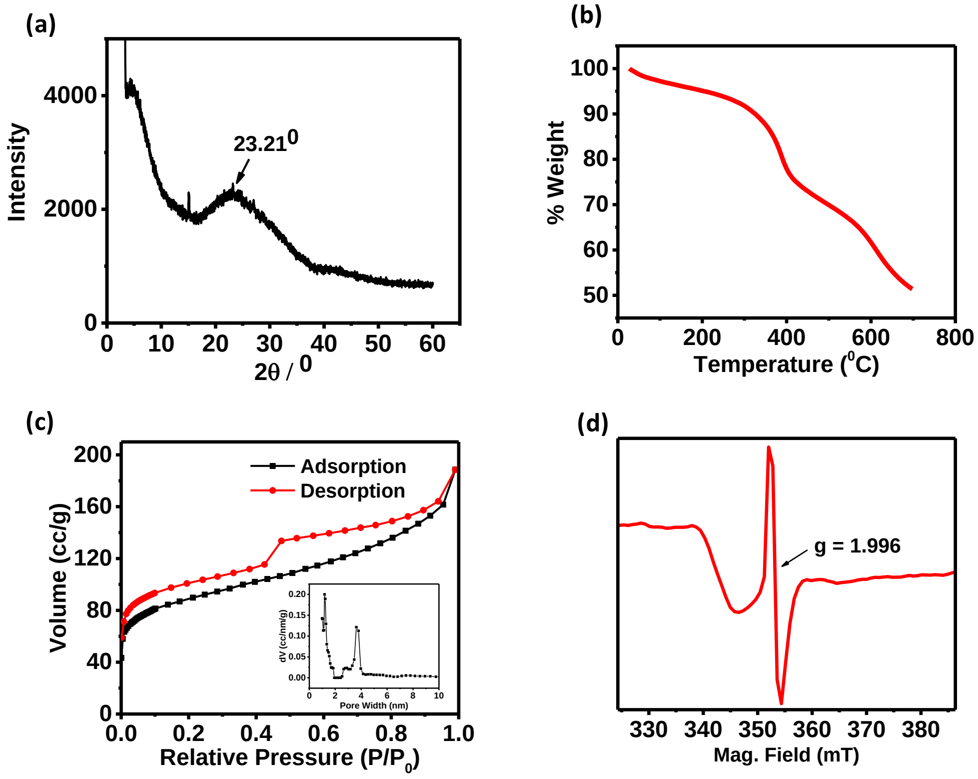

Figure 5: (a) PXRD pattern; (b) TGA analysis; (c) N_2 adsorption at 77 K (inset:pore size distribution); (d) EPR spectrum of **TPA-NDI**.

Due to the presence of tris(4-ethynylphenyl)amine in the framework, we investigated the CO_2 adsorption (Figure 6) at 273 K and it showed an uptake of 30.96 cc/g.

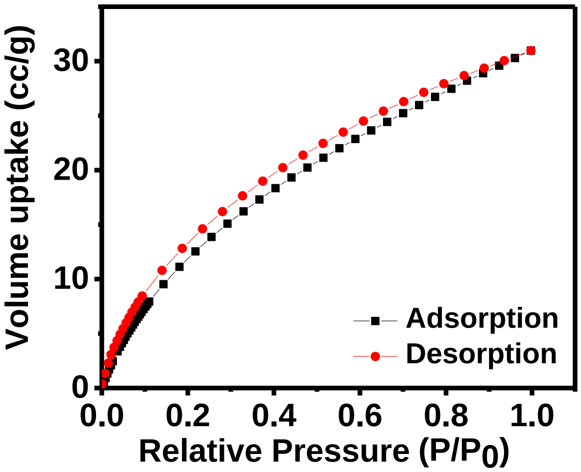

Figure 6: CO$_2$ adsorption isotherm at 195 K.

To understand the morphology of **TPA-NDI**, FESEM and TEM images were recorded. Both showed the sheet liked morphology stacked one upon the other with random orientation (Figure 7a-d).

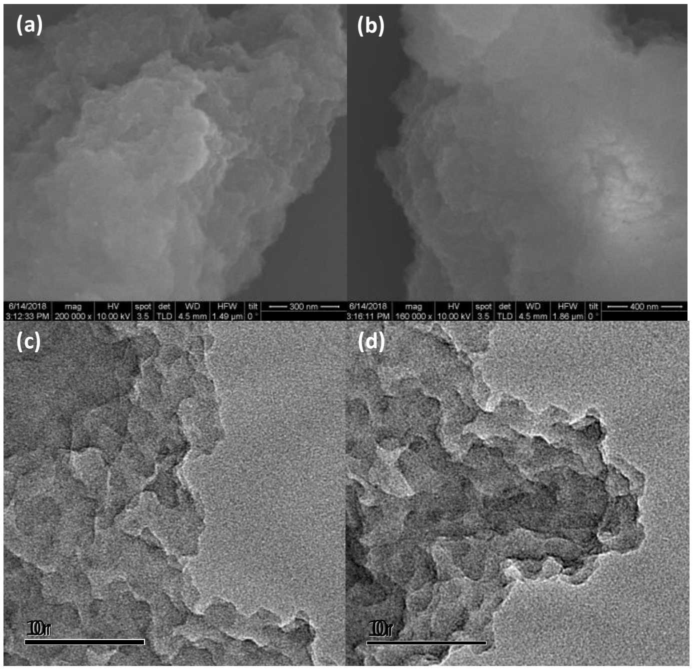

Figure 7: (a,b) FESEM images; (c,d) TEM images of **TPA-NDI** CMP.

Focusing more on the design of the framework, it can be seen that tris(4-ethynylphenyl)amine can act as a donor molecule due to the presence of the electron-rich nitrogen in the molecule. Whereas, the naphthalene diimide (**NDI**) can act as a very good acceptor due to the presence of the carbonyl groups present in it. So NDI can be reduced to radical anion and the dianion following the 1e$^-$ and 2e$^-$ reduction respectively. The formation of donor acceptor pair was confirmed by EPR studies (Figure 5d). The g value of 1.996 indicated the existence of charge separated state in the polymer. Moreover, the framework is fully conjugated, it can help in the electron delocalization throughout the molecule.

3.2 Characterization of TBA-NDI

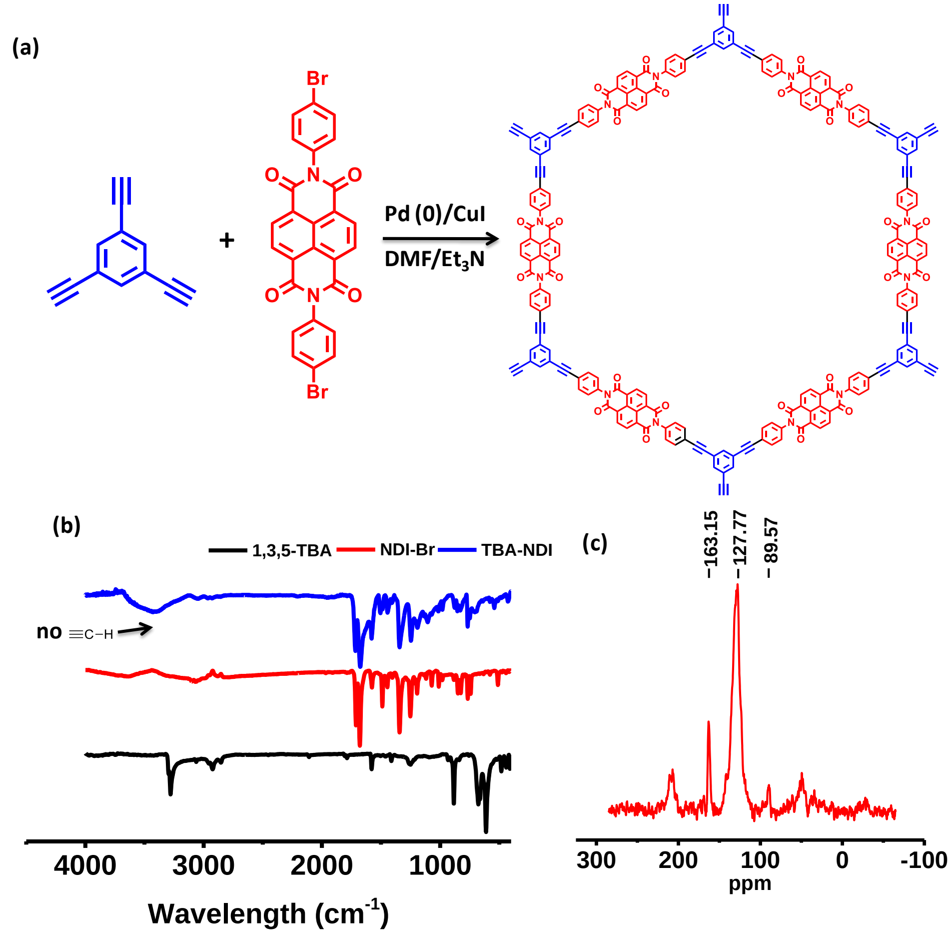

Figure 8: (a) Schematic of **TBA-NDI** CMP; (b) FT-IR spectra; (c) ^{13}C solid state NMR of **TBA-NDI** CMP.

Another CMP **TBA-NDI** was synthesized as shown in Figure 8a. **TBA-NDI** lacks the donor part and thus does not form the donor acceptor pair. The CMP was characterized by

^{13}C cross polarization magic angle spinning NMR spectroscopy, IR, TGA, PXRD, N_2 adsorption studies, FESEM and TEM images.

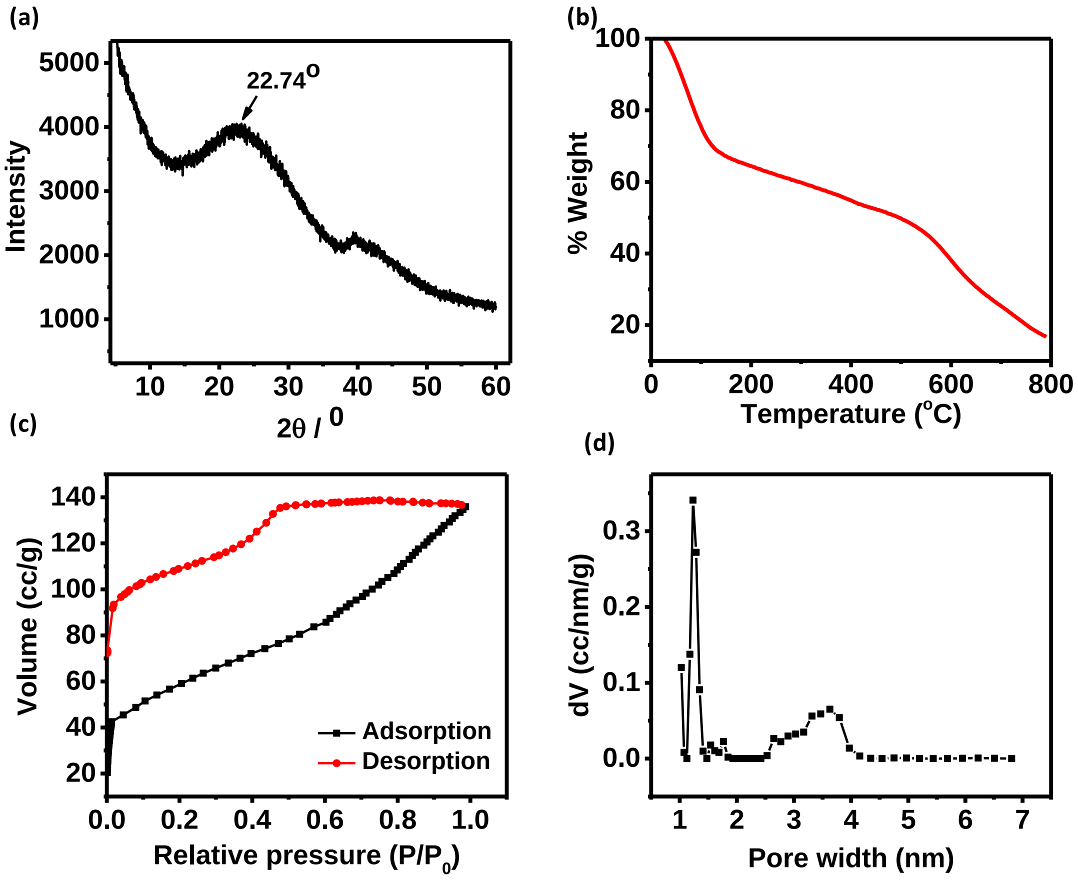

Figure 9: (a) PXRD pattern; (b) TGA curve; (c) N_2 adsorption isotherm at 77 K; (d) Pore size distribution of **TBA-NDI** CMP.

IR spectrum (Figure 8b) showed a peak at 3280 cm^{-1} which corresponds to ≡C-H was missing in **TBA-NDI** polymer and indicated that **TBA** is a part of the framework. ^{13}C solid state NMR (Figure 8c) lead to the confirmation by peaks at 89.57 ppm, 127.77 ppm and 163.15 ppm which corresponds to the acetylene carbons, the aromatic core and the carbonyl carbons respectively. PXRD showed a broad peak, showing amorphous nature, at a 2Θ value of 22.74^{o} and thus corresponded to the interlayer spacing of 3.90 Å (Figure 9a). TGA showed that there was weight loss of about 30% upto 120 ^{o}C which may be due to the loss of solvent molecules. Further it was found stable upto 520 ^{o}C. The polymer showed an uptake of 135.9 cc/g of N_2 at 77K with the surface area of 204.166 m^{2}/g in the BET range. Pore size distribution by NLDFT method showed both the mesopore and the micropore being present in the sample and thus gave the pore width of 1.23 nm and 3.62 nm. The morphology was studied with FESEM and TEM images (Figure 10 a-d). FESEM and TEM images showed layered nature of the compound which were stacked one upon the other in a random orientation.

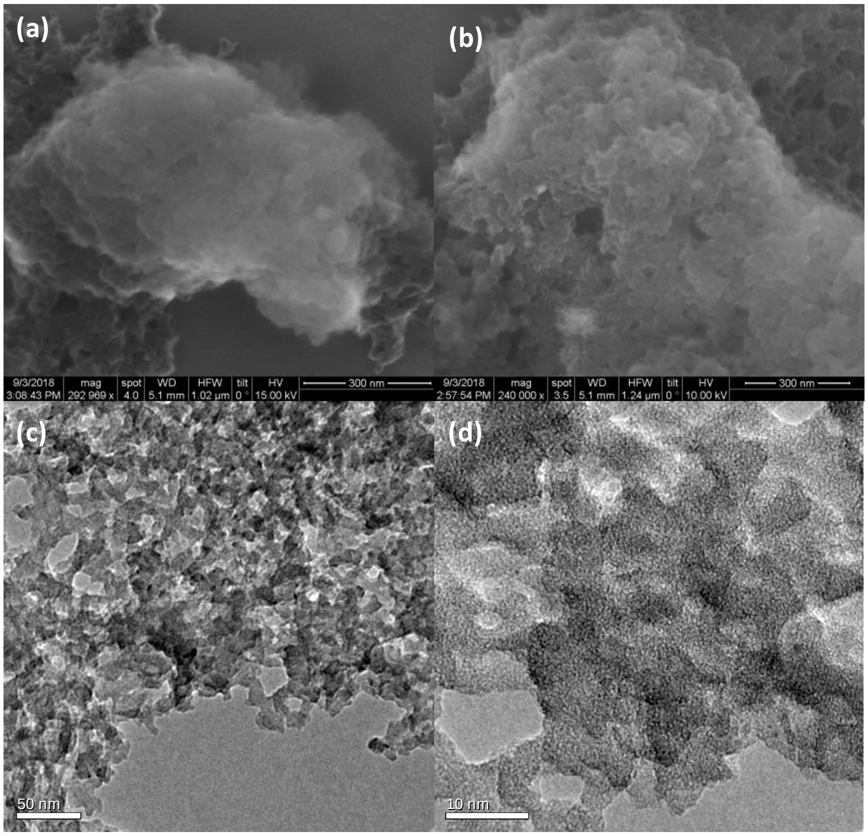

Figure 10: (a,b) FESEM images; (c,d) TEM images of **TBA-NDI** CMP.

3.3 Electrochemical activity

The CV of **TPA-NDI** was recorded in anhydrous acetonitrile along with tetrabutylammonium hexaflorophosphate (TBAPF$_6$) as a supporting electrolyte. CV showed two peaked at -0.93 V and -1.27 V, thus indicating the formation of NDI$^{\cdot -}$ and NDI^{2-} (Figure 11). This showed that **NDI** preserved its electron accepting behavior even on being the part of the polymer. Thus, observing the above characteristics in the framework, its electrocatalytic activity towards oxygen reduction reaction(ORR) was investigated.

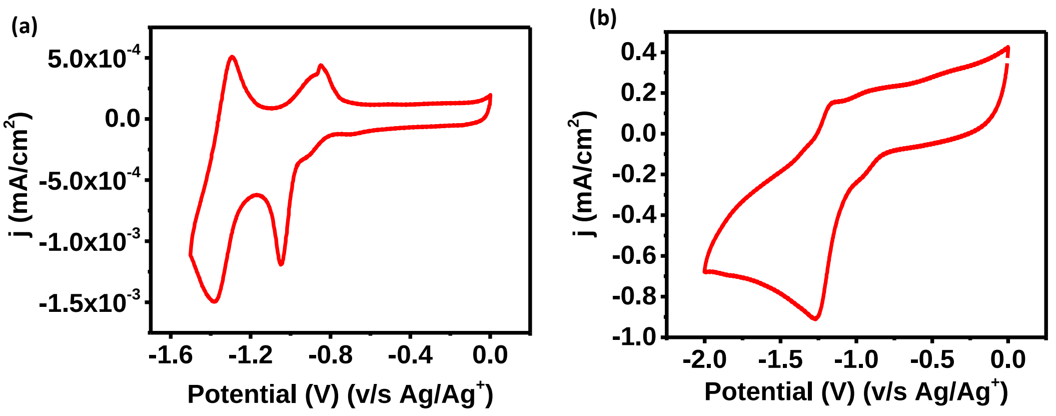

Figure 11: (a) CV of **NDI-Br**; (b) CV of **TPA-NDI** CMP.

3.4 Oxygen Reduction Reaction of TPA-NDI:

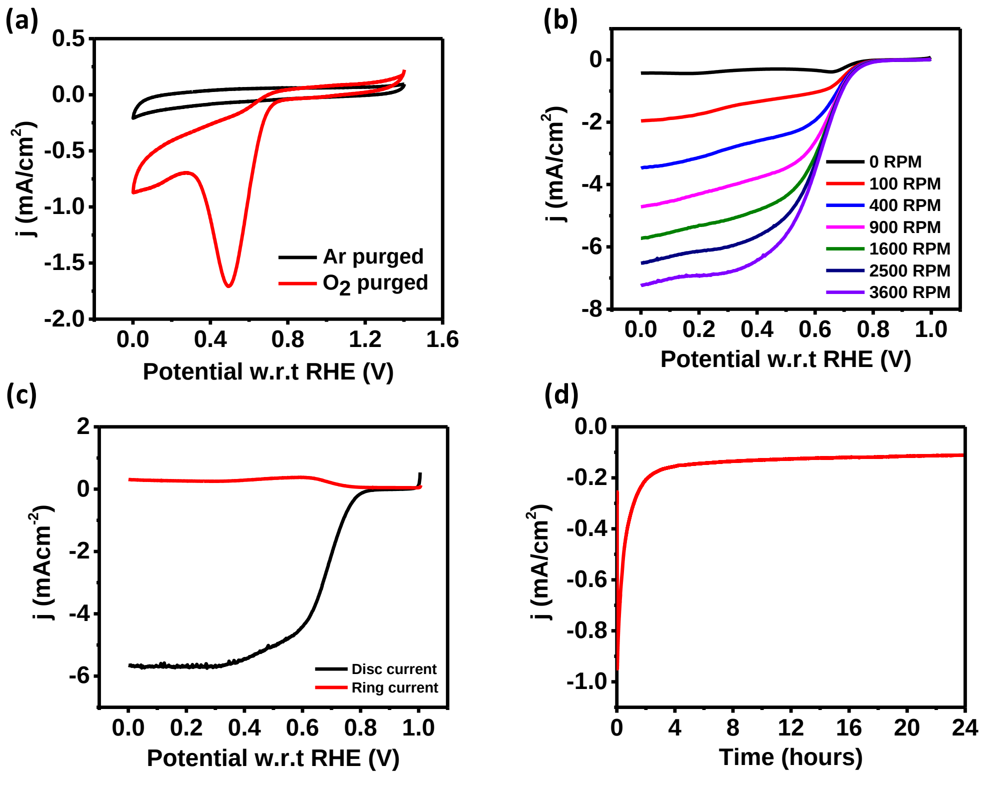

Figure 12: (a) CV in Ar saturated and O_2 saturated KOH; (b) LSV curves at different rotation speeds; (c) RRDE curve; (d) Chronoamperometry plot showing the stability; of **TPA-NDI** CMP.

The CV was performed in 0.1 M KOH in both Ar and O_2 atmosphere. No peak was observed in CV obtained under the Ar atmosphere but an oxygen reduction peak was observed in the oxygen atmosphere (Figure 12a). It was observed that this gave a maximum current density of -5.75 mA/cm^2 at 1600 RPM (onset at 0.86V) at a scan rate of 10 mV/s. A current density of -1 mA/cm^2 was obtained at 0.690 V which is comparable to the already reported values.[29] The current density increased as the rotation speed was increased. K-L plots proved the 4 electron transfer process. RRDE also showed 4 electron transfer process (n≈ 3.4) and 28% H_2O_2 was produced (Figure 12c & 13a). To check the stability of the electrocatalytic activity, chronoamperometry test was performed for 24 hours. It showed no significant decrease in current density even after 24 hours which showed its high stability (Figure 12d). To find the charge transfer resistance, the Nyquist plot was recorded (Figure 13b). The charge transfer resistance (R_{ct}) of the electrode-electrolyte was found out to be 81.4 Ω. The low charge transfer resistance is expected to be the reason for high electrocatalytic of CMP.

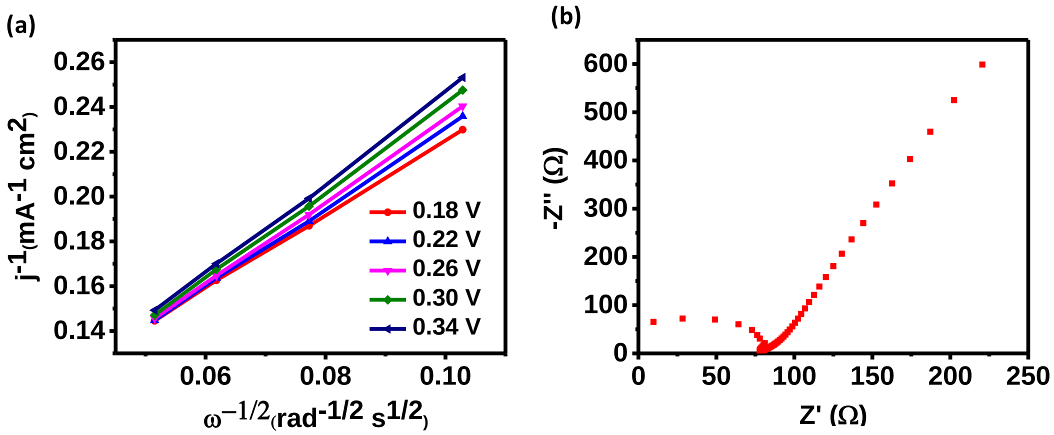

Figure 83: (a) K-L plot; (b) Nyquist Plot of **TPA-NDI** CMP.

3.5 In-situ Stabilization of Cobalt in TPA-NDI(Co@TPA-NDI)

To introduce the OER activity into **TPA-NDI** framework in-situ stabilization of Co nanoparticles was carried out without using any extra reducing agent and capping agent (Figure 14). The nitrogen present in **TPA** framework provided a binding site for Co. On binding of Co with the nitrogen of **TPA** species, the electron transfer takes place from the electron rich nitrogen to Co(II) and thus converting into cobalt nanoparticles.

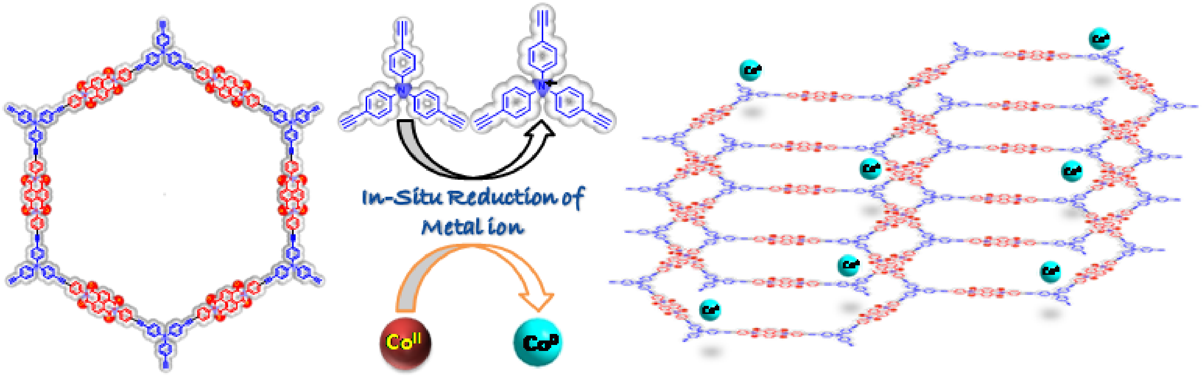

Figure 94: Schematic of in-situ stabilization of Co(II) to Co nanoparticles.

According to stoichiometric ratio two electrons are needed for the formation of Co nanoparticles, so the close proximity of the nitrogen atoms in the framework leads to the stabilization of the cobalt between the nitrogen rich sites. This framework **Co@TPA-NDI** was characterized by XPS, elemental analysis (EDX), FESEM and TEM.

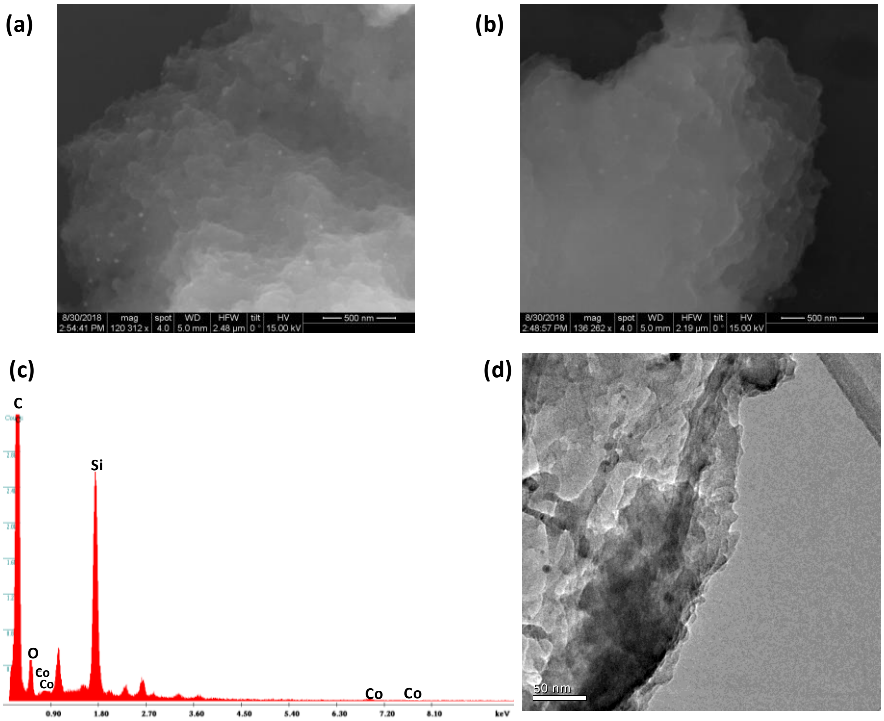

Figure 105: (a,b) FESEM images; (c) EDX spectrum showing presence of cobalt nanoparticles; (d) TEM image of **Co@TPA-NDI** CMP.

FESEM and TEM images showed layered morphology with the metal particles doped in between the layers of the polymer (Figure 15). The presence of cobalt nanoparticles was confirmed by EDX spectrum. The amount of Co nanoparticles was found out by Inductively Coupled Plasma Atomic Emission Spectroscopy (ICP-AES) and was found out to be 3.2 wt%.

3.6 Electrocatalytic activity of Co@TPA-NDI

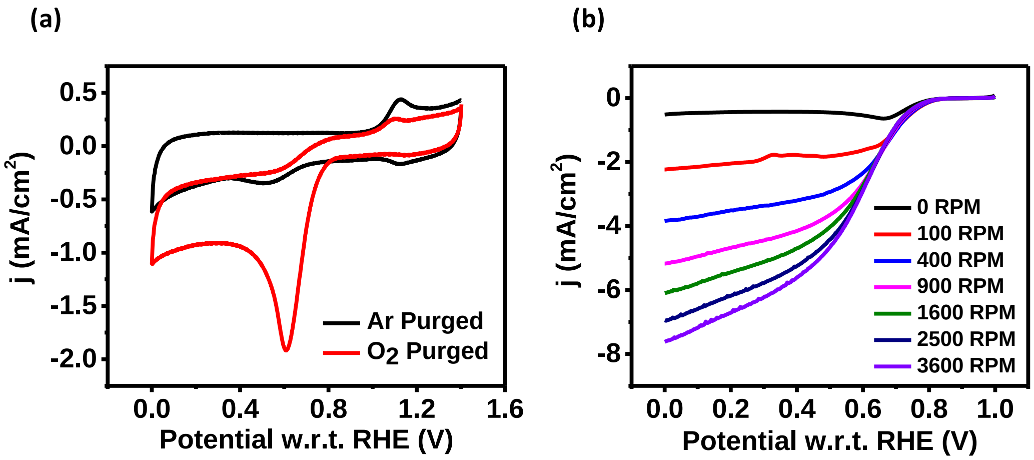

Figure 116: ORR (a) CV; (b) LSV of **Co@TPA-NDI**.

There was no significant change in the ORR catalytic behavior of the compound (Figure 16), but it showed a fair OER catalysis in 0.1 M KOH as an electrolyte (Figure 17). LSV and CV were recorded and it showed the current density of 13.7 mA/cm^2 at 1.82 V. The electrode was rotated at 1600 RPM to prevent the accumulation of evolved oxygen bubbles at the electrode surface. The onset was found out to be 1.57 V with a small overpotential of 340 mV (w.r.t thermodynamic water oxidation potential) and a Tafel slope of 113.43 mv/dec. Another parameters to demonstrate the efficiency of the catalyst are roughness factor (RF) and electrochemically active surface area (EASA).[30] RF is defined as the ratio between EASA and geometric surface area (**GSA**). So RF directly influences the catalytic activity. To find EASA, CV was recorded in the capacitive region at various scan rates. As, $i_C = \nu C_{DC}$, where, i_C stands for double layer charging current, ν represents the scan rate and C_{DL} is electrochemical double layer capacitance.[31]

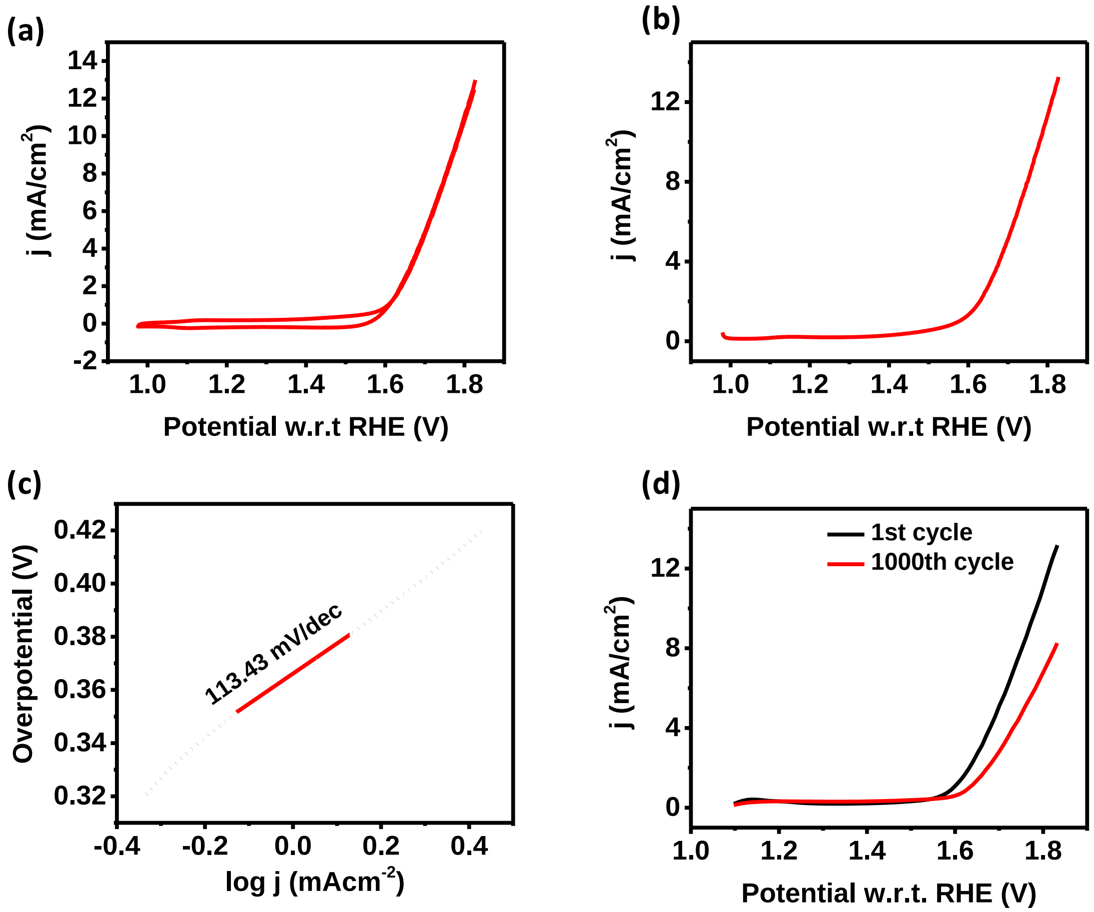

Figure 127: (a) CV; (b) LSV; (c) Tafel plot; (d) Cycling stability of Co@TPA-NDI CMP during oxygen evolution reaction.

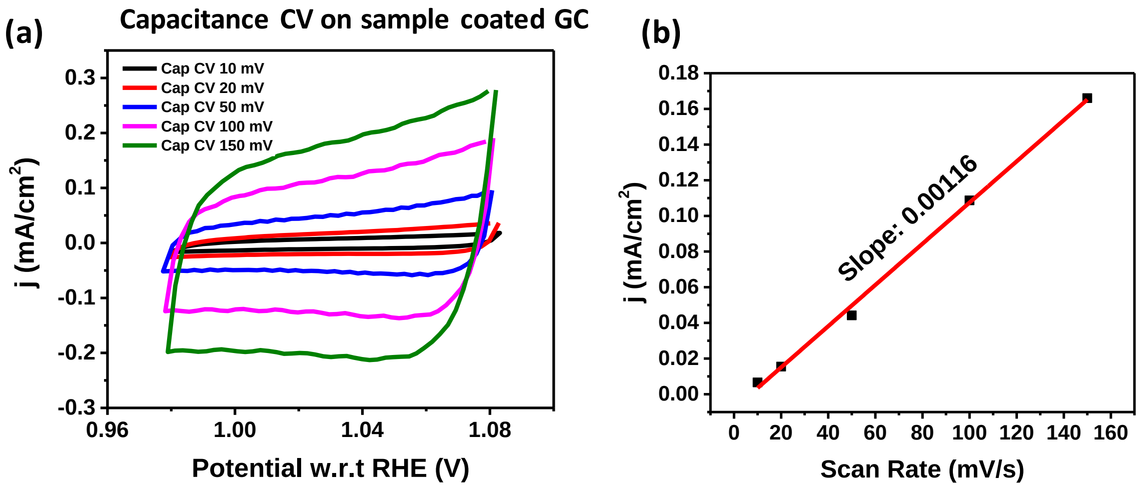

Figure 13: (a) Capacitance CV of **Co@TPA-NDI** CMP on GC; (b) corresponding current density v/s scan rate plot.

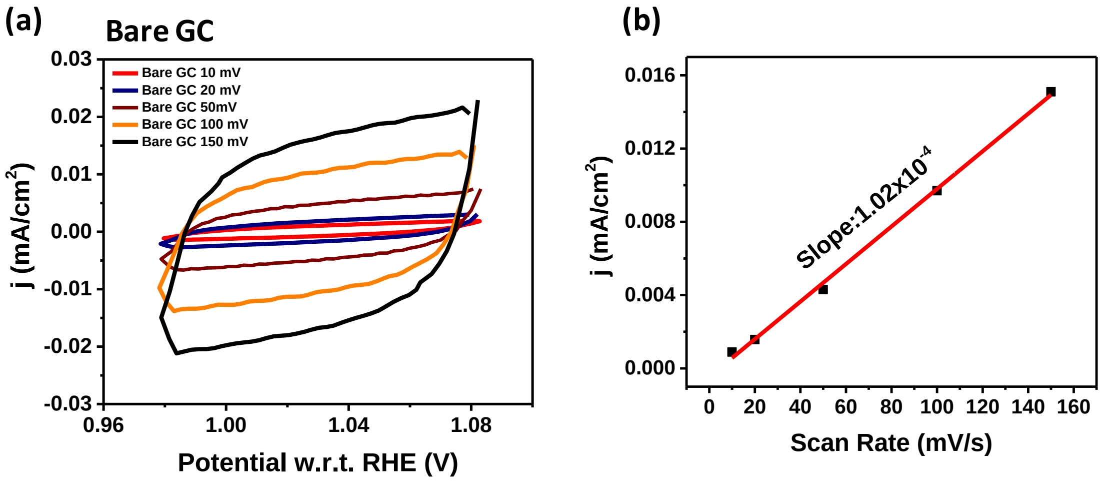

Figure 14: (a) Capacitance CV of Bare GC; (b) corresponding current density v/s scan rate plot.

So, the plot between the current density and the scan rate was obtained to find the double layer capacitance for both bare glassy carbon electrode (C_{bare}) and the sample coated electrode (C_{cat}) (Figure 18 & 19). EASA is the ratio of C_{cat} to C_{bare}. Thus the electrochemical active surface area (EASA) was found out to be 11.37. The roughness factor was calculated by the dividing of **EASA** and the geometrical surface area of the electrode and was found out to be 160.93.

3.7 Application in Zinc-Air Battery

As **TPA-NDI** showed good ORR activity, we tried constructing a primary battery. On loading 1 mg/cm^2 of the sample on the carbon paper, and using 6 M KOH as the electrolyte along with a zinc foil as the counter electrode, the open circuit voltage was found out to be ≈ 1.3 V. Galvanodynamic discharge curve showed the current density of 56 mA/cm^2 when the battery was discharged to 0.2 V thus giving the power density of 18.631 mW/cm^2. An LED was also successfully lit using the two cells in series and a 100 Ω resistance, which lasted up to 44-46 hours. The battery was recharged to the same open circuit voltage by replacing the corroded Zn foil and the electrolyte solution and thus showing the robust nature of the catalyst in 6 M KOH solution. Further, the stability of the battery was examined by withdrawing 5 mA/cm^2 continuously for three hours (Figure 20b) showing no significant drop in the battery voltage.

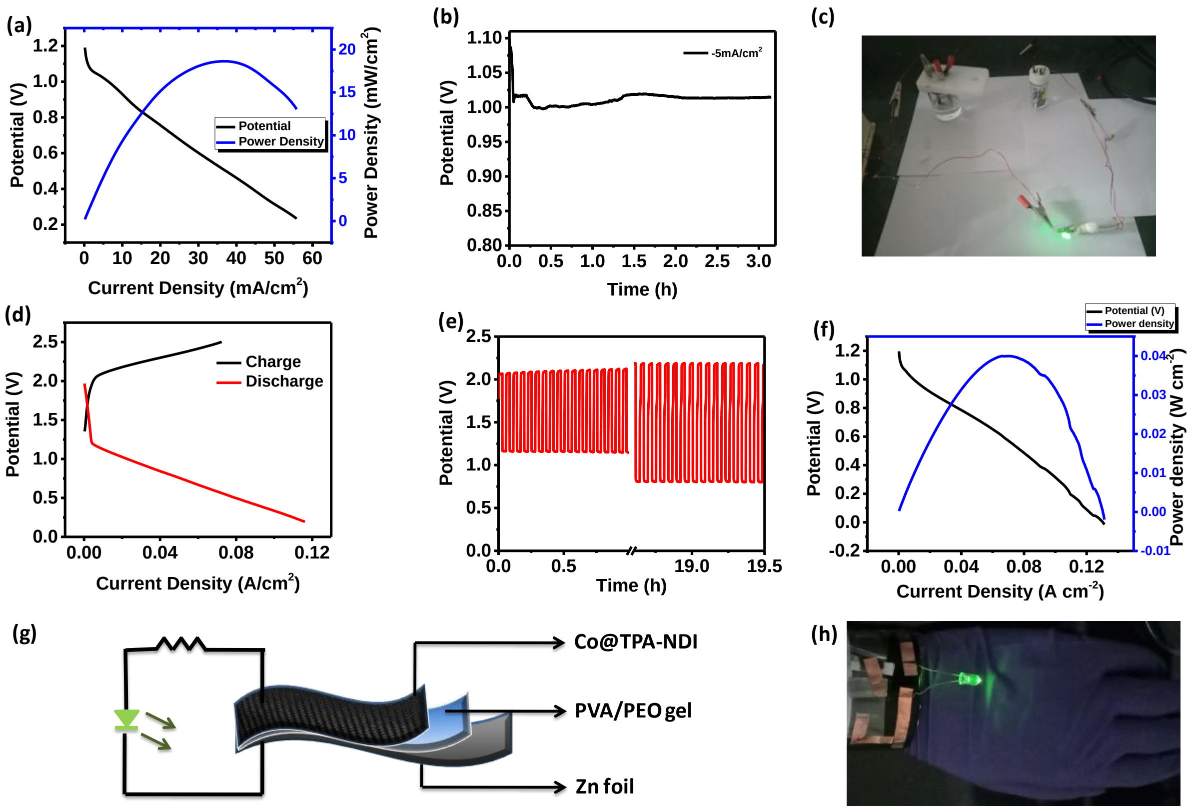

Figure 20: (a) Galvanodynamic discharge curve; (b) Stability at -5mA/cm2; (c) Image showing a glowing LED using **TPA-NDI** CMP; (d) Galvanodynamic charge discharge curve; (e) Galvanostatic charge discharge curve; (f) Power density curve of secondary battery fabricated using **Co@TPA-NDI**; (g) Schematic showing the fabrication of flexible battery using **Co@TPA-NDI** CMP; (h) Image showing the flexible nature of battery (worn as a wrist band).

Motivated by the bi-functional behavior of **Co@TPA-NDI**, the secondary battery was constructed (Figures 20d-f) and the power density was calculated to be 40 mW/cm^2. To check the robustness of the battery, galvanostatic charge-discharge curves were recorded at a current density of 5 mA/cm^2 up to 19 hours which showed that the voltage dropped by 0.36 V after 18 hours operation. Further, the CMP being light weight and possessing sheet like morphology can withstand stress when coated onto a flexible substrate without getting damaged. To demonstrate its use in wearables and flexible electronics, an all solid state battery was designed using PVA/PEO gel as an electrolyte, carbon cloth as a current collector along with **TPA-NDI** material coated as a cathode material and the Zn foil as the anode. The battery was fabricated on a cylindrical surface which can be worn on the wrist as shown in the Figure 20h.

Recently, Bhaumik and co workers synthesized a metal free covalent organic polymer containing porphyrin unit as electrocatalyst for HER.[32] It was shown that nitrogen atoms in the porphyrin ring acted as an active centre for proton binding. Similarly, due to the presence of nitrogen atom in TPA unit can act as a binding site for proton. Motivated by this fact, HER was studied by LSV recorded in 0.5 M H_2SO_4.

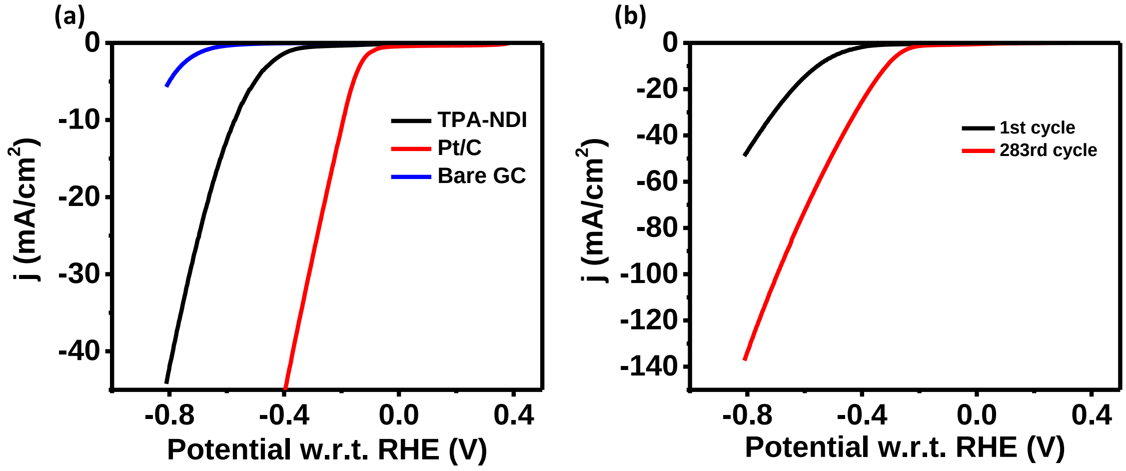

Figure 21: (a) LSV curves of **TPA-NDI**, Pt/C and bare GC electrode; (b) Cycling stability of **TPA-NDI** for HER.

TPA-NDI showed a current density of 44.22 mA/cm^2 with the overpotential of 571.4 mV. The sharp increase in the current density with the applied potential showed the beginning of the HER reaction. The LSV is further compared to the noble and state of art catalyst Pt/C and also the bare GC electrode (Figure 21a). The bare GC was found out to be inactive for HER reaction. So the catalyst **TPA- NDI** plays a key role in HER activity. With comparison to Pt/C, the catalyst **TPA-NDI** was not able match the activity but is still valuable because of low cost, metal free system. The tafel slope was found out to be 193 mV/dec. Moreover to check the stability of the catalyst, repeated LSV cycles were carried out and it was observed that the activity increased many folds. The current density increased to 144.88 mA/cm^2 with lowering of the overpotential by 241 mV. As the synthesis of **TPA-NDI** was a Pd catalyzed reaction, so to prove that even the minor amount of Pd did not play any role in HER catalysis and to find the binding site for proton, control reaction was carried out which lacked the **TPA** unit.

As **TBA-NDI** lacked the binding site for proton, HER was not observed (Figure 22). The synthesis of **TBA-NDI** was also a Pd catalyzed reaction, this proves the fact that a very minute quantity of leftover Pd in the pores of the framework does not help in HER. This shows that the binding site is very important for the catalytic reaction to take place. Also, **TBA-NDI** does not form a donor acceptor pair, also signifies the importance of donor acceptor pair as in **TPA-NDI**.

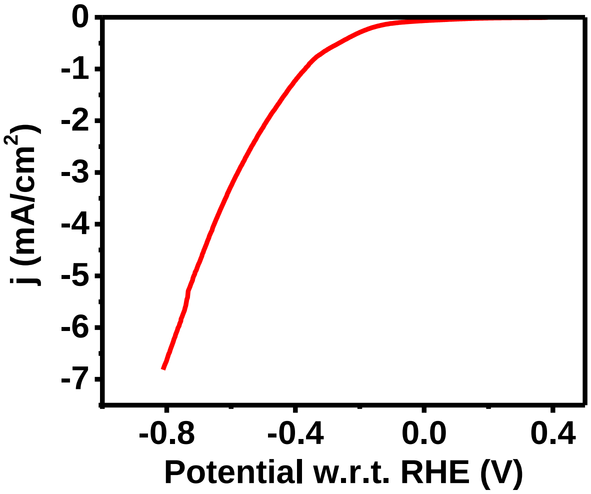

Figure 152: LSV curve of **TBA-NDI** for electrocatalytic hydrogen reaction.

With **TPA-NDI** showing ORR and HER, and **Co@TPA-NDI** being active for OER and ORR, self powered overall electrochemical water splitting was demonstrated. For overall water splitting, OER and HER processes occur simultaneously. This process was powered by the two Zn air batteries, fabricated above, connected in series. While the ORR and OER process occur during charging and discharging of the battery, simultaneously OER and HER processes also take place in the electrochemical water splitting cell. For the demonstration, the material was coated onto a glassy carbon electrode which was further connected to the battery. For the fabrication of the water electrolyser, an H-type cell with 0.1 M KOH in first compartment and 0.5 M H_2SO_4 in the other. Both the compartments were separated by a proton conducting membrane (Nafion 117).[33] The circuit was completed by connecting the positive terminal of the battery to the GC electrode in KOH and negative to the GC electrode in H_2SO_4.

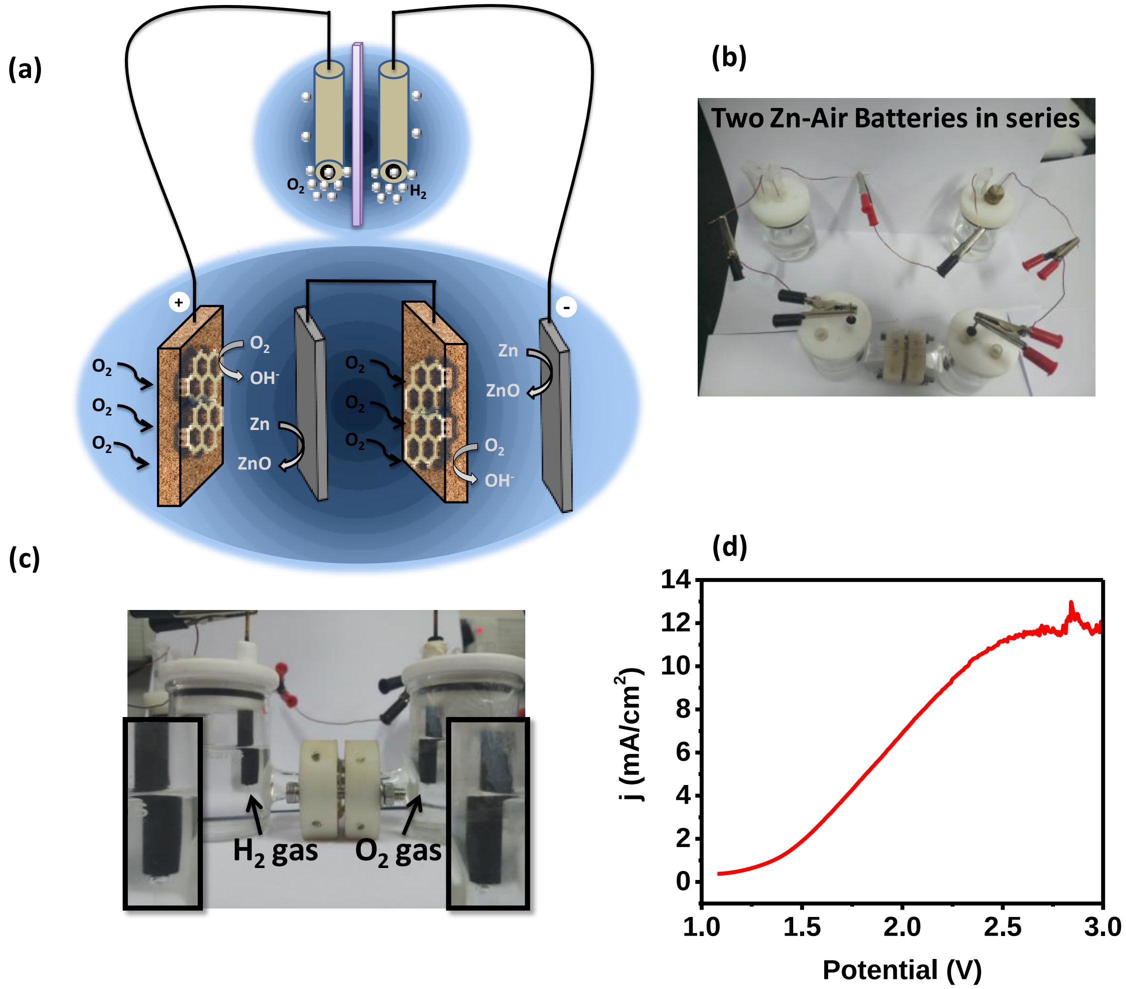

Figure 163: (a) Schematic showing the overall water splitting; (b) Optical image showing two Zn-air batteries connected in series which were further connected to water electrolyzer; c) Optical image showing the evolution of O_2 and H_2 at glassy carbon electrode (inset: magnified images of evolved gasses); (d) Polarization curves in two electrode configuration in H-type cell.

On completion of the circuit, oxygen and hydrogen gas bubbles were observed on the electrodes surface and thus showing self powered overall water splitting. Maximum current density of 11.5 mA/cm^2 was obtained at the potential of 2.6 V. The saturation in the polarization curve was observed after 2.6 V because of the formation of the bubbles on the electrode surface.

3.8. Computational Results:

To find out the catalytic sites DFT calculations were performed. Molecular orbital (MO) analysis of model 1 (**TPA-NDI**) displayed that the highest occupied molecular orbital (HOMO) is located on the triphenyl amine (**TPA**) unit and the lowest unoccupied molecular orbital (LUMO) is situated on the napthalene diimide (**NDI**) unit. Similarly, in model 2 (**TBA-NDI**), **NDI** unit holds LUMO exclusively whereas the HOMO is distributed over phenyl rings. Thus, in the donor-acceptor CMP, the **TPA** unit acts as an electron donor whereas the **NDI** unit acts as an acceptor.

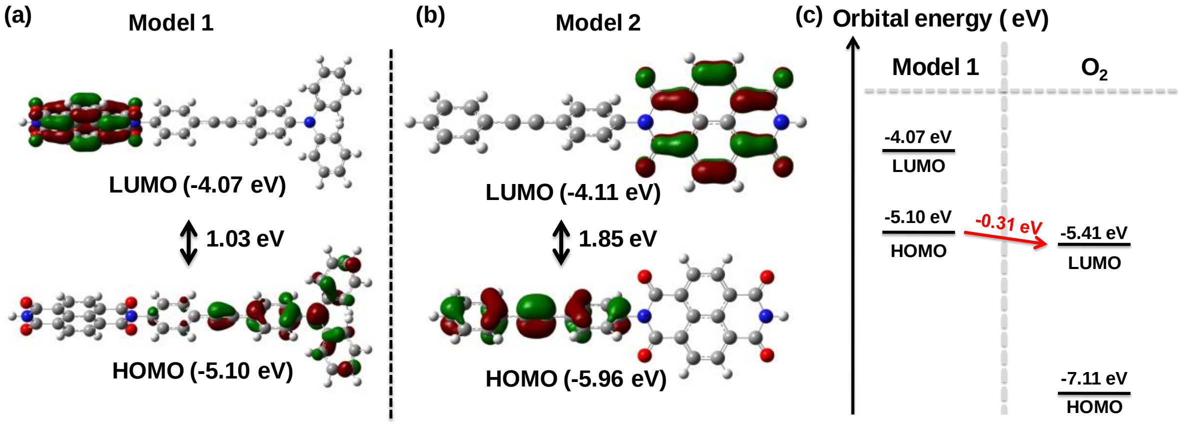

Figure 174: Representation of HOMO-LUMO diagram of the (a) model **1** (**TPA-NDI**) and (b) model **2** (**TBA-NDI**). (c) HOMO-LUMO comparison of model **1** with dioxygen.

The HOMO-LUMO gaps of model **1**&**2** were found to be 1.03 and 1.85 eV, respectively, indicating semiconducting behavior and, therefore, both the CMPs were found to exhibit electrocatalysis. The Nyquist plot revealed that the model **1** has less resistance over model **2**. The observation was also supported computationally. We optimized the models as charge-separated species by putting a negative charge on **NDI** unit and a positive charge on the remaining part of the models. Charge-separated states were found to be higher in energy by 6.03 and 7.80 eV from their respective ground state of model **1** and model **2**, respectively, indicating that model **1** possesses higher conductivity than model **2**.

The CMP exhibited very good ORR electrocatalysis and we investigated the dioxygen binding capability on **TPA** as well as **NDI** units. In model 1, dioxygen binding on **TPA** released 11.9 kcal/mol of energy whereas binding on **NDI** released only 6.34 kcal/mol, indicating that **TPA** offers a better binding site to dioxygen than that for **NDI**.

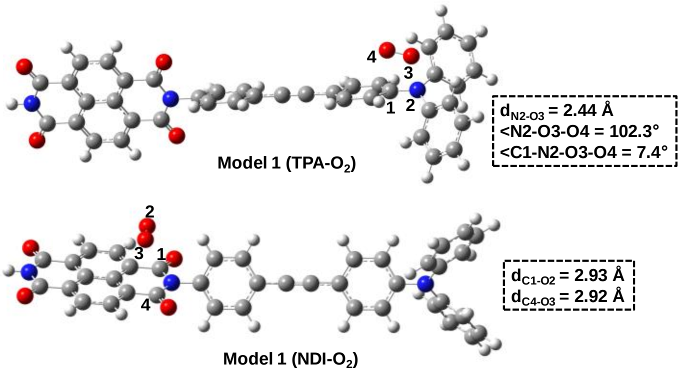

Figure 185: Binding site of O_2 on **TPA** and **NDI** units in model **1**.

For a successful ORR electrocatalysis process, electron must be transferred from the HOMO of the catalyst to the LUMO of dioxygen. The computation revealed that the LUMO of dioxygen is situated by 0.31 eV lower in energy than the HOMO of model 1, indicating such electron transfer is feasible. Moreover, the computed reduction potential of model 1 and model 2 are -1.19 and -1.18 V, respectively, whereas the reduction potential of dioxygen under the experimental condition is +0.59 V. The above data signify that both the CMPs are capable of reducing dioxygen.

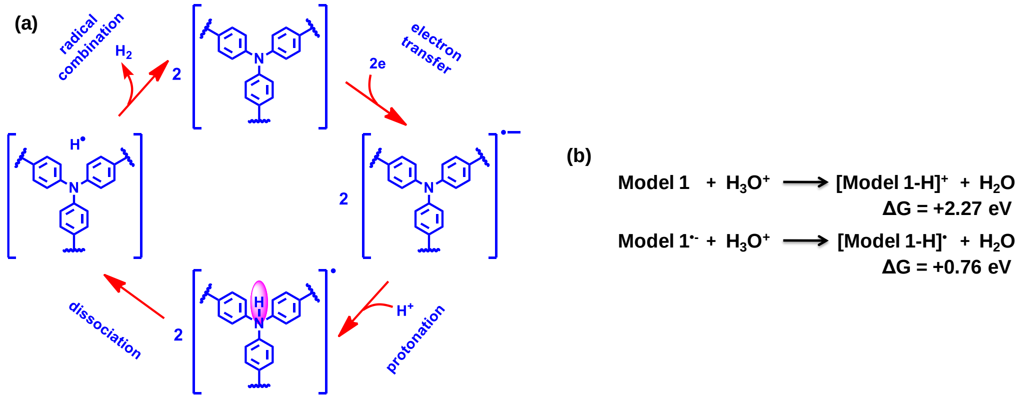

Figure 196: (a) A possible mechanism for HER activity and (b) free energy release upon proton binding with **TPA** unit.

The **TPA-NDI** CMP showed activity for electrocatalytic hydrogen evolution reaction. To gain more insight about the process, we investigated proton binding capability of **TPA** unit in model 1 which showed a relatively easier binding capability ($\Delta G = 0.76$ eV) in its radical anion form than that in neutral state ($\Delta G = 2.27$ eV). The radical anion state can be formed upon taking electron from the electrode. Therefore, we propose that the **TPA** radical anion accommodate proton and produce hydrogen radical those combine together to produce dihydrogen as shown in Figure 26a.

4. Conclusion

In conclusion, we have put forward an idea of utilizing the donor acceptor based redox active conjugated microporous polymer **TPA-NDI** as a bifunctional metal free catalyst for ORR, HER and ORR, HER upon in-situ stabilization of cobalt nanoparticles (**Co@TPA-NDI**) in which closely placed nitrogen sites from **TPA** acted as sites for the adsorption of a proton for HER and as a binding site for oxygen which could lead to overall catalysis. Moreover, their low overpotentials, excellent onset, high electrocatalytic stability and low cost give an edge over the other noble metal catalysts. Further, we were able to successfully construct a Zn-Air battery **Co@TPA-NDI** conjugated microporous polymer as a cathode material. This material being organic, possesses flexibility and thus can be used as a cathode material in all solid state flexible Zn-air batteries. Moreover, the material being active for OER and HER was shown as the potential material for water electrolyzers and thus the self powered overall water splitting. We have a firm belief that this will open a new branch of cathode materials, not only for Zn-Air batteries but in general for all the metal-air batteries and potential materials for efficient energy conversion devices.

5. References

1. R. R. K. Bandhana Devi, Aditi Halder, *ACS Sustain. Chem. Eng*, 2019, **7**, 2187.
2. Z. W. Xin Qin, Jingrui Han, Yonglan Luo, Fengyu Xie, Guangwei Cui, Xiaodong Guo and Xuping Sun, Xiaodong Guo Xuping Sun, *Chem. Commun*, 2018, **54**, 7693.
3. G. Z. Min Kuang, *small,* 2016, **12**, 5656.

4. Q. L. Hui Li, Peng Wen, Trey B. Williams, Shiba Adhikari, Chaochao Dun, Chang Lu, Dominique Itanze, Lin Jiang, David L. Carroll, George L. Donati, Pamela M. Lundin, Yejun Qiu, and Scott M. Geyer, *Adv. Mater.*, 2018, **30**.
5. Z. M. Huabin Zhang, Jingjing Duan, Huimin Liu, Guigao Liu, Tao Wang, Kun Chang, Mu Li, Li Shi, Xianguang Meng, Kechen Wu, and Jinhua Ye, *ACS Nano*, 2016, **10**, 684.
6. M. A. a. J.-M. Tarascon, *Nature*, 2008, **451**, 652.
7. C. N. C. Joseph F. Parker, Irina R. Pala, Meinrad Machler, Michael F. Burz, Jeffrey W. Long, Debra R. Rolison, *Science*, 2017, **356**, 415.
8. Z. K. Tingting Wang, Shichun Mu, Jingping Liu, Daping He, Ibrahim Saana Amiinu, Wen Meng, Kui Zhou, Zhixiong Luo, Somboon Chaemchuen, and Francis Verpoort, *Adv. Funct. Mater.*, 2018, **28**.
9. H. C. Chang-Yuan Su, Wei Li, Zhao-Qing Liu, Nan Li, Zhufeng Hou, Fu-Quan Bai, Hong-Xing Zhang, and Tian-Yi Ma, *Adv. Energy Mater.*, 2017, **7**, 1602420.
10. Y. Z. Yifan Xu, Ziyang Guo,Jing Ren, Yonggang Wang, Huisheng Peng, *Angew. Chem. Int. Ed.*, 2015, **54**, 15390.
11. M.-L. L. Hui Cheng, Chang-Yuan Su, Nan Li, and Zhao-Qing Liu, *Adv. Funct. Mater.*, 2017, **27**.
12. Z. P. C. Jing Fu, Moon Gyu Park, Aiping Yu, Michael Fowler, and Zhongwei Chen, *Adv. Mater.*, 2017, **29**.
13. P. Y. Yingying Guo, Jianan Zhang, Yongfeng Hu, Ibrahim Saana Amiinu, Xin Wang, Jigang Zhou, Huicong Xia, Zhibo Song, Qun Xu, Shichun Mu, *ACS Nano*, 2018, **12**, 1894.
14. K. S. Danni Ding, Xiaodong Chen, Huirong Chen, Junying Chen, Ting Fan, Rongfang Wu, Yingwei Li, *ACS Catal.*, 2018, **8**, 7879.
15. K. A. K. Guangyu Chen, Dong Su, Meng Li, Chiu-Hui Wang, David Buceta, Chunyu Du, Yunzhi Gao, Geping Yin, Kotaro Sasaki, Miomir B. Vukmirovic, Radoslav R. Adzic, *Chem. Mater*, 2016, **28**, 5274.
16. H. D. Yanguang Li, *Chem. Soc. Rev.*, 2014, **43**, 5143.
17. J.-P. G. Olga Kasian, Simon Geiger, Serhiy Cherevko, Karl J. J. Mayrhofer, *Angew. Chem. Int. Ed.*, 2018, **57**, 2488.

18. Y. Y. Bao Yu Xia, Nan Li, Hao BinWu, XiongWen (David) Lou and XinWang, *Nature energy*, 2016, **1**.
19. Q. D. Mingdao Zhang, Hegen Zheng, Mindong Chen, and Liming Dai, *Adv. Mater.*, 2018, **30**.
20. S. Z. Xiaxia Li, Ling Jin, Yan Li, Pengbiao Geng, Huaiguo Xue, Huan Pang, Qiang Xu, *Adv. Energy Mater.*, 2018, **8**.
21. C. Z. Yingbo Li, Jie Liu, Xiaoqiao Zeng, Shengxiang Qu, Xiaopeng Han, Yida Deng, Wenbin Hu, and Jun Lu, *Adv. Mater.*, 2018, **30**.
22. P. Y. Yueyang Qiao, Yongfeng Hu, Jianan Zhang, Shichun Mu, Jihang Zhou, Hao Li, Huicong Xia, Jing He, and Qun Xu, *Adv. Mater.*, 2018, **30**.
23. X. H. Shengjie Peng, Linlin Li, Shulei Chou, Dongxiao Ji, Huangjiao Huang, Yonghua Du, Jian Liu, and Seeram Ramakrishna, *Adv. Energy Mater.*, 2018, **8**.
24. X. W. Jia Yang, Bo Li, Liang Ma, Lei Shi, Yujie Xiong, Hangxun Xu, *Adv. Funct. Mater.*, 2017, **27**.
25. G. W. T. M. J. Frisch, H. B. Schlegel, G. E. Scuseria, M. A. Robb, J. R. Cheeseman, G. Scalmani, V. Barone, B. Mennucci, G. A. Petersson, H. Nakatsuji, M. Caricato, X. Li, H. P. Hratchian, A. F. Izmaylov, J. Bloino, G. Zhe.
26. J. A. H. K. S. Grimme, S. Ehrlich, *J. Chem. Phys.*, 2010, **132**.
27. A. D. Becke, *J. Chem. Phys.*, 1993, **98**, 5648.
28. O. A. V. A. V. Krukau, A. F. Izmaylov, and G. E. Scuseria, *J. Chem. Phys.*, 2006, **125**.
29. S. Roy, A. Bandyopadhyay, M. Das, P. P. Ray, S. K. Pati and T. K. Maji, *Journal of Materials Chemistry A*, 2018, **6**, 5587.
30. A. Singh, S. Roy, C. Das, D. Samanta and T. K. Maji, *ChemComm*, 2018, **54**, 4465.
31. C. C. L. McCrory, S. Jung, J. C. Peters and T. F. Jaramillo, *J. Am. Chem. Soc.*, 2013, **135**, 16977.
32. S. K. Bidhan Chandra Patra, Rabindra Nath Manna, Sujan Mondal, Debabrata Pradhan, Anirban Pradhan, Asim Bhaumik, *ACS Catal.*, 2017, **7**, 6120.
33. J. Yin, P. Zhou, L. An, L. Huang, C. Shao, J. Wang, H. Liu and P. Xi, *Nanoscale*, 2016, **8**, 1390.

Chapter 5

Metallated Conjugated Microporous Polymer as a Trifunctional Electrocatalyst, Cathode Material for Zinc-Air Batteries & Self-powered Overall Water Splitting

Abstract

The development of cost effective, green and renewable energy resources is of vital significance to prevent further deterioration of the Earth's atmosphere as caused by large combustion of fossil fuels. The use of different and highly expensive noble metal based electrocatalysts for oxygen reduction reaction (ORR), oxygen evolution reaction (OER) and hydrogen evolution reaction (HER) has hindered the commercialization process. As an alternative to this, the development of efficient non-noble metal based electrocatalyst for energy storage and conversion devices is of prime importance. This chapter discusses an approach to design and synthesize a highly stable porous metal free electrocatalyst **POR-PQ** that consists of donor porphyrin (**POR**) as a node and an acceptor 2,7-dibromophenanthrene-9,10-dione (**PQ**) as a linker. **POR-PQ** is found to be active towards oxygen reduction reaction (ORR). Upon metallation of porphyrin with Co(II) led to the introduction of OER and HER thus showing trifunctional behavior. Further, the trifunctional catalyst is used as a cathode material for rechargeable Zn-air batteries which utilizes ORR during the discharge process and OER during the charging process. Moreover, the same catalyst was used as an anode and cathode for water electrolysis to generate hydrogen and oxygen which was powered by the fabricated Zn-air battery. We believe that the development of such trifunctional catalyst will help in easy and fast commercialization of not only efficient metal air batteries and water electrolyzers but also various green energy storage and conversion devices.

1. Introduction

In this era of ever increasing energy requirement, the burden on conventional non renewable energy sources is increasing drastically which is followed by enhancement of various environment related issues at a global scale.[1-3] To overcome this, various green energy sources are being developed which are still very far from the stage of commercialization. One of the greener ways that is currently being exploited to the maximum is the electrochemical pathway for energy generation, storage and conversion. This can be achieved by the development of systems such as efficient fuel cells,[4, 5] water electrolyzers,[6] metal air batteries[7] and supercapacitors.[8, 9] But the dire challenge for the development of these efficient systems is the sluggish nature of the electrochemical reactions taking place which include oxygen reduction reaction (ORR), oxygen evolution reaction (OER) and hydrogen evolution reaction (HER).[10] Many state of art catalysts such as Pt/C for ORR and HER and oxides RuO_2 and IrO_2 for OER activity have been developed. Moreover, these being scarcely present in the earth curst and are highly expensive which prevent their commercialization. So in this situation, development of an efficient, stable and non-noble metal based trifunctional catalyst active towards ORR, OER as well as HER which can be used in regenerative fuel cells, water elecrolyzers and metal-air batteries will be a blessing in disguise.

The dream of development and realization of a trifuctional catalyst can be achieved by the careful optimization of electronic properties of the system and also by introducing the competent active sites for the reaction to take place. The development of efficient rechargeable metal-air batteries (particularly Zn-air battery) requires a bifunctional catalyst which is active towards both ORR and OER. On the other hand, complete electrolysis of water requires OER and HER to take place. Till date, many bifunctional catalysts active towards ORR and OER have been developed which have been successfully realized as the cathode material in Zn-air batteries.[11] On the other hand, bifunctional catalysts possessing OER and HER activities for overall water splitting reaction have also been widely reported.[12] But the number of trifunctional catalysts active towards ORR, OER as well as HER are still rare and easily countable. Many MOF derived metallated carbonaceous nanostructures, 2-D carbon based materials with heteroatom doping (such as B, N, F) and metal doping or metal free porous materials have been found to possess bifunctionality and in few cases trifunctionality is reported.[13] Recently, Dai *et al*. have synthesized nitrogen, phosphorous and fluorine doped graphene and showed trifunctionalility towards ORR, OER and HER. Also self powered overall water splitting was carried out.[14] Further, Yao and coworkers systematically demonstrated the effect of defects by the removal of heteroatoms from graphene and thus the achievement of a trifunctional electrocatalyst.[15] But these suffer from various serious concerns such as non-renewability, porosity and structural irregularities. So as an alternative, π conjugated conducting organic compounds, such as organosulfur[16-18], organic carbonyl,[19-22] organic free radical[23-25] and conducting polymers are being explored as electrode materials. However, these organic materials do not possess long-term stability making seldom use in existing technologies. Apart from this, M-N_4 (M = Fe, Co) moieties were studied for electrocatalytic reactions.[26, 27] But these possessed low catalytic activity and stability. To overcome this, carbonaceous materials were formed which provided a good support to M-N_4 moieties. These are found to be highly active towards electrocatalytic reactions such as ORR, OER and HER.[28-31] But, a major limitation is very high temperature synthesis. Recently, Singh *et al*. showed Co(II) metalated phthalocyanines in CMP active for OER.[32] Along with this, the necessity of the framework in catalytic activity was also proved. In an another report, Roy *et al*. designed and synthesized redox active donor-acceptor metal free CMP with enhanced catalytic activity towards ORR and showed nitrogen in triphenylamine moiety as the active site for oxygen binding.[33]

We herein design and synthesize a novel redox active donor-acceptor conjugated microporous polymer with donor 5,10,15,20-tetra(4-ethynylphenyl)porphyrin as the node and redox active acceptor 2,7-dibromophenanthrene-9,10-dione as the linker with the covalent bond between the monomers providing a robust and porous framework (**POR-PQ**). The porous nature allows the facile movement of the reactants to and back from the catalytically active sites. Moreover, the formation of CMP leads to dense packing and regular placement of nitrogen atoms which are well known binding sites for oxygen reduction reaction. So, the metal free system was found to be active for ORR. We envision that the metallation of porphyrin with Co will lead to the formation of a trifunctional electrocatalyst (having ORR, OER and HER) due to the presence of Co-N_4 moieties. Moreover, the presence of N_4 coordinating site of porphyrin provides easy accessibility and high stability to the metal ion and thus prevents leaching of metal ion from the framework. So, upon metalation of cobalt(II) into the porphyrin ring, the resultant CMP (**Co-POR-PQ**) possessed highly catalytically active Co-N_4 site and thus was found to be good for ORR, OER as well as HER. Further, **Co-POR-PQ** was used as a cathode material in Zn-air battery as well as the cathode and anode material in water electrolyzer. The water electrolyzer was powered by the Zn-air battery and thus self powered overall water splitting was carried out.

2. Experimental Section

2.1 Materials

All chemicals were purchased from Sigma-Aldrich, TCI or spectrochem and were used as it is without any purification. Required solvents were dried using standard procedure.

2.2 Synthesis

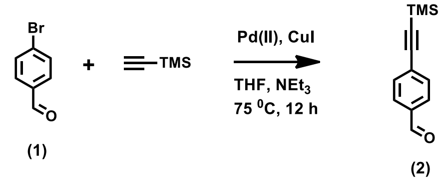

Scheme 1: Reaction for synthesis of 4-((trimethylsilyl)ethynyl)benzaldehyde

2.2.1 Synthesis of 4-((trimethylsilyl)ethynyl)benzaldehyde(2)

4-bromobenzaldehyde (5 g, 27.02 mmol)(**1**), $Pd(PPh_3)_2Cl_2$ (1.9 g, 2.7 mmol), CuI (1.0 g, 5.25 mmol) were added into a schlenk flask which was degassed and purged with nitrogen. This procedure was repeated thrice for complete inert atmosphere. This was then followed by the addition of dry and degassed THF (75 mL) and triethylammine (75 mL). Then, trimethylsilylacetylene (TMSA) (15.35 mL, 108.08 mmol) was added to reaction mixture and the reaction flask was sealed properly. The reaction mixture was heated to 75 ^{0}C and stirred overnight. The trimethylsilyl protected product (2) (Scheme 1) was purified by silica gel coloumn chromatography. Yield: 3.2 g, 15.81 mmol, 60 %

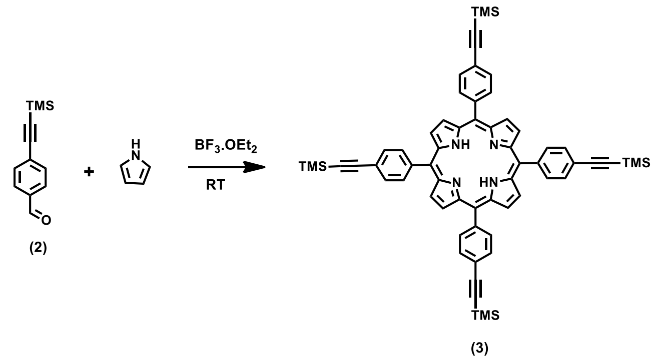

Scheme 2: Reaction for synthesis of 5,10,15,20-tetrakis(4-trimethyl(phenylethynyl)silane)porphyrin

2.2.2 Synthesis of 5,10,15,20-tetrakis(4-trimethyl(phenylethynyl)silane)porphyrin(3)

The synthesis of **3** was carried out by dissolving **2** (1 g, 4.94 mmol) and pyrrole (0.342 mL, 4.93 mmol) in 700 mL $CHCl_3$ (Scheme 2). The solution was degassed for one hour followed by the addition of 1.5 mL of $BF_3.OEt_2$ and was stirred at room temperature. After 3 hours, 1.12 g of DDQ was added followed by stirring overnight. After the completion of reaction, the solvent was evaporated under reduced pressure and the product was dissolved in hexane and DCM (50% each) followed by purification by column chromatography in neutral alumina and was dried to obtain product (3) as a purple solid. Yield: 250 mg, 0.25 mmol, 5.1 %.

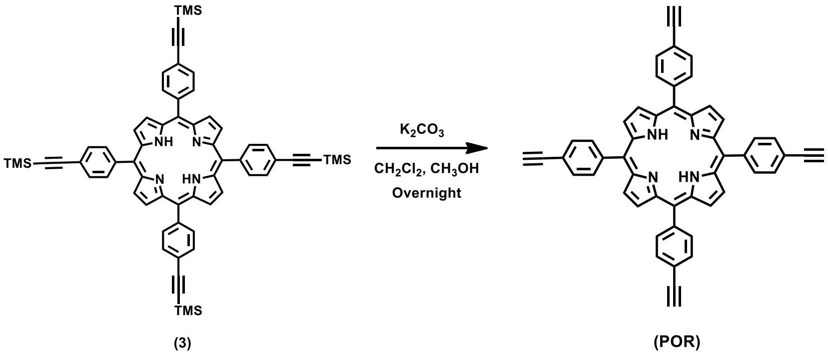

Scheme 3: Reaction for synthesis of 5,10,15,20-tetrakis(4-ethynylphenyl)porphyrin

2.2.3 Synthesis of 5,10,15,20-tetrakis(4-ethynylphenyl)porphyrin(POR)

For desilylation, **3** (250 mg, 0.25 mmol) was dissolved in mixture of DCM/methanol (75 mL/50 mL) along with 1 g of K_2CO_3 (Scheme 3). The mixture was stirred overnight followed by filtration. The solvent was dried under vacuum followed by purification by coloumn chromatography using neutral alumina with DCM as eluent. Yield: 160 mg, 0.23 mmol, 92%. Metalation of POR by Co(II) was performed by refluxing **POR** and excess $CoCl_2·6H_2O$ in dimethylformamide to produce **Co-POR**.

2.2.4 Synthesis of POR-PQ and Co-POR-PQ Conjugated Microporous Polymer

The synthesis of **POR-PQ** was carried out by adding 5,10,15,20-tetra(4-ethynylphenyl)porphyrin (190 mg, 0.267 mmol) (POR), 2,7-dibromophenanthrene-9,10-dione (PQ) with $Pd(PPh_3)_4$ (300 mg, 0.259 mmol) as the catalyst in the schlenk flask. The flask was degassed and purged with N_2. The procedure was repeated thrice. Following this, dry and degassed DMF/triethylamine (3 mL/0.5 mL) were added to the schlenk flask. The reaction mixture was added heated at 120 ^{0}C. After 12 hours, the reaction mixture was cooled down to room temperature and filtered. The product was purified by soxhlet in THF, methanol and chloroform. The obtained product was used for further characterizations. Same procedure was followed with Co-POR to obtain **Co-POR-PQ**

2.3 Physical Measurements

Infrared spectra were recorded in transmittance mode by making KBr pellets in Bruker FT-IR spectrophotometer. The thermal stability of the CMPs were measured with Mettler Toledo TGA 850 instrument in N_2 atmosphere and at a scan rate of 5 ^{o}C/min. The temperature was varied from 50 ^{o}C to 800 ^{o}C. To study the powder X-Ray diffraction of the sample, Bruker D8 discover instrument was used by scanning 2ϴ from 5^o to 60^o. Morphological images were obtained using ZEISS Gemini SEM 500 Field Emission Scanning Electron Microscope (FESEM) by drop casting dispersion of the samples in ethanol onto the precleaned silicon wafer and captured under high vacuum with an accelerating voltage of 2kV. The TEM images were captured using JEOL JEM 2100 PLUS microscope at an acceleration voltage of 200kV and coating the dispersion of the samples on the carbon coated copper grid. Solid state ^{13}C cross-polarization magnetic angle spinning (CP/MAS) NMR spectrum was measured on a Varian infinity plus 300WB spectrometer at a MAS rate of 5 kHz and a CP contact time of 1.4 ms. ^{1}H NMR is recorded on a Bruker AV-400 spectrometer with chemical shifts reported as ppm.

2.4 Adsorption Measurements

Adsorption Measurements were carried out to study the porous nature of the CMPs using Quantachrome Quadrasorb instrument at 77 K for N_2. 80 mg-100 mg of the samples were transferred into an adsorption cell and degassed at 190 ^oC under a vaccum of $1x10^{-1}$ Pa to empty the pores of the polymer. Helium gas was used to evacuate the chamber and make the system free from any N_2 present. Further, all the operations were computer controlled.

2.5 Electrochemical Measurements

Electrochemical measurements were done using Autolab PGSTAT12 potentiostat/galvanostat along with Metrohm RDE-2 rotator. To study electrochemical activity of the samples, rotating disc electrode (RDE) and rotating ring disc electrode (RRDE) voltammetery techniques were used. The glassy carbon rotating disc electrode was polished by rubbing it onto the polishing cloth along with alumina powder (0.05 um mesh). The electrode was then rinsed with MilliQ water followed by ultrasonication in MilliQ water for about 10 second. The electrode was dried in open air and a mirror like shining surface was obtained. To prepare the catalytic ink, 2.5 mg of compound, 2.5 mg of Vulcan C, 490 uL of IPA and 490 uL of water along with 20 uL of Nafion (5 wt %, Sigma Aldrich) were taken in a vial and then sonicated for about an hour to make a uniform dispersion. 8 µL of the prepared ink was coated onto the cleaned glassy carbon electrode surface and was dried for 2 hours in the open atmosphere. For ORR and OER, 0.1 M KOH solution was prepared as an electrolyte. All the measurements were done in three electrode configuration with Hg/HgO(1M NaOH) as the reference electrode and the Pt coil as the counter electrode. For OER, the electrolyte was purged with Ar for 30-45 min to remove all the dissolved oxygen. The CV was recorded at a scan rate of 50mV/sec whereas LSV was recorded at a scan rate of 5 mV/sec and 1600 RPM. For ORR, a CV was recorded in Ar purged electrolyte at a scan rate of 50 mV/sec. To show the ORR catalytic activity, the solution was saturated with oxygen. A CV was recorded at a scan rate of 50mV/sec showing the ORR peak. Further LSV curves were recorded at a scan rate of 5 mV/sec and at different rotation speeds. The RRDE voltammogram was recorded by coating 8 uL of the above dispersion ink on the disc to record the amount of H_2O_2 produced. For HER 0.5 M H_2SO_4 solution was used as an electrolyte along with Ag/AgCl as the reference electrode and the Pt as the counter electrode. All the recorded potentials were converted to the potentials w.r.t RHE. All the measurements were carried out at room temperature. The number of electrons involved in the reduction process were calculated using Koutecký–Levich (K–L) equation:

$$\frac{1}{j} = \frac{1}{j_L} + \frac{1}{j_K}$$

$$\frac{1}{j} = \frac{1}{B\omega^{1/2}} + \frac{1}{j_K}$$

$$B = 0.62nFC_0(D_0)^{2/3}\nu^{-1/6}$$

$$j_K = nFkC_0$$

where, j correspond to the measured current density, j_K and j_L correspond to the kinetic and diffusion-limited current densities, ω corresponds to the angular frequency of the RDE in radians per second, n is the number of electrons involved in the reaction, F is the Faraday constant (96485 C mol^{-1}), D_0 is the diffusion coefficient of O_2 in the electrolyte (1.93 × 10^{-5} cm^{2}s $^{-1}$), ν is the kinematic viscosity of the electrolyte (1.01 × 10^{-2} cm^{2}s $^{-1}$), C_0 is the concentration of O_2 in the electrolyte (1.26 × 10^{-6} mol cm^{-3}) and k is the electron transfer rate constant. The number of electrons and the amount of H_2O_2 formed during ORR were calculated using rotating ring disk electrode (RRDE) voltammetry technique which is based on the ratio of the disk and the ring current obtained, as shown in the equations given below. For the RRDE experiments, the ring electrode was held at a potential of 1 V to oxidize hydrogen peroxide.

$$n_e = \frac{4|I_D|}{|I_D| + \frac{|I_R|}{N}}$$

$$\%H_2O_2 = \frac{\frac{I_R}{N}}{I_D + \frac{I_R}{N}} \times 200$$

Where, N = 0.2678 is the collection efficiency, I_D is the Faradaic disk current, and I_R is the Faradaic ring.

2.6 Fabrication of Zn-air Battery

Zn- Air battery was tested in a two electrode system. The catalyst ink was prepared by mixing 2 mg of **Co-POR-PQ**, 2 mg of Vulcan C in 245 uL of water, 245 uL of IPA and 10 uL of Nafion(5 wt %, Sigma-Aldrich). Effectively 1 mg/cm^2 of the sample was coated on the carbon fiber paper. Zn foil was used as an anode and the **Co-POR-PQ** as the cathode. 6 M KOH along with 0.2 M Zinc acetate dihydrate was used as the electrolyte. The electrolyte was completely purged with O_2 before any measurement.

2.7 Self Powered Overall Water Splitting

For the fabrication of water electrolyser, an H-type cell was used with a Nafion 117 membrane between the two cells. Initially, the nafion membrane was placed between the two compartments and both the compartments were filled with water to hydrate the membrane. For the electrolysis, **Co-POR-PQ** was coated onto two glassy carbon electrodes and were dipped into two compartments of the electrolyser with 0.1 M KOH solution and 0.5 M H_2SO_4 in the two compartments. For self powered overall water splitting, two Zn-air batteries were connected in series. The positive terminal of the battery was connected to the anode of the electrolyser (for OER) and the negative terminal was connected to cathode (for HER). Further to record the polarization curve of the electrolyser, potentiostat was used in two electrode setup with the anode of the electrolyser as the working electrode and cathode was connected to counter and reference (both short circuited) of the potentiostat.[34]

2.8 Computational Details

DFT calculations were performed with Gaussian09 program package.[35] The model consisted of POR and PQ unit. B3LYP hybrid functional in with 6-31G* basis set were used for the ground state geometry optimizations. Along with this, to tackle weak interactions, Grimme's d3 dispersion was used.[36, 37] The optimized geometries were verified by frequency analysis. To evaluate the molecular orbital energies, HSEH1PBE/6-31+G* was used.

3. Results and Discussion

3.1 Characterization:

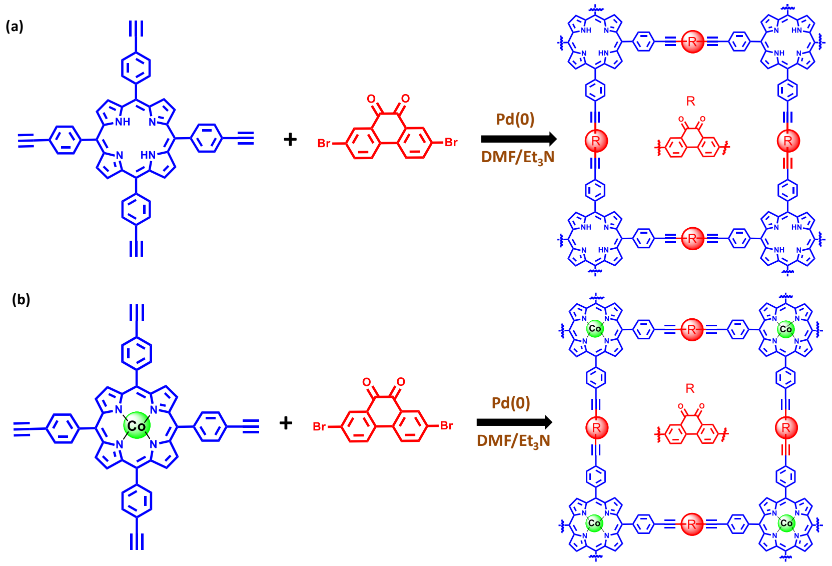

Figure 1: Schematic showing synthetic scheme of (a) **POR-PQ**; (b) **Co-POR-PQ**

In this study, two redox active donor acceptor conjugated microporous polymers (CMPs) were designed and synthesized by Sonogashira-Hagihara coupling reaction between 2,7-dibromophenanthrene-9,10-dione (**PQ**) and 5,10,15,20-tetra(4-ethynylphenyl)porphyrin (**POR**) forming **POR-PQ**, and **PQ** coupled with **POR** metalated with cobalt(II) as shown in Figure 1 . Assynthesized CMPs (**POR-PQ** and **Co-POR-PQ**) were characterized by powder X-ray diffraction (PXRD), thermogravimetric analysis (TGA), N_2 adsorption studies, UV-visible, infrared (FT-IR), ^{13}C cross polarization magic angle spinning solid state NMR spectroscopies, FESEM and TEM studies.

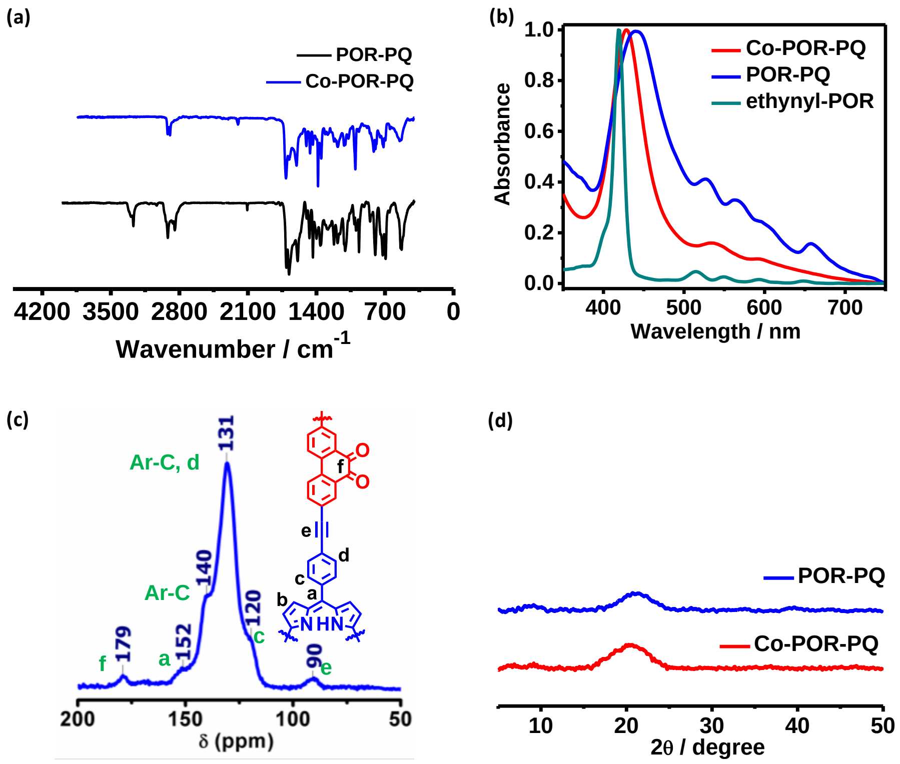

Figure 2: (a) FT-IR spectra; (b) UV-Vis Spectra; (c) ^{13}CSolid State NMR; (d) PXRD patterns of **POR-PQ** and **Co-POR-PQ.**

FT-IR spectrum of **POR-PQ** (Figure 2a) showed peaks at 3268 cm^{-1}, 2107 cm^{-1} and 1682 cm^{-1} which correspond to N-H, C≡C and C=O bonds respectively. This indicated the presence of POR and PQ in the polymer backbone. Whereas, FT-IR spectrum of **Co-POR-PQ** lacked N-H stretching vibration which supported complete occupancy of porphyrin units by Co(II). Moreover, UV-Vis spectrum of **POR** and **POR-PQ** CMP (Figure 2b) showed a soret band at 411 nm and four Q bands at 527 nm, 563 nm, 597 nm and 657 nm, thus confirming the presence of **POR** in the backbone. Notably, the soret band of **POR-PQ** was red shifted by 23 nm which is due to the increased conjugation of **POR** on formation of the completely conjugated framework. After Co insertion (in **Co-POR-PQ**) the soret band was blue shifted by 9 nm as it was observed at 432 nm and the number of Q bands was also reduced to two. Further, ^{13}C cross polarization magic angle spinning solid state NMR was performed to confirm the formation of the desired CMP. The peaks at 90 ppm, 131 ppm, 179 ppm showed the presence of acetylene carbon, aromatic core and C=O carbons respectively and thus confirming the presence of both the monomers into the framework as shown in the

Figure 2c. To study the packing of synthesized **POR-PQ** and **Co-POR-PQ**, PXRD patterns were recorded which showed a broad peak at 21^0, as shown in Figure 2d. The interlayer spacing was found to be 4 Å, and indicates the presence of π-π stacking between layers of the CMPs.

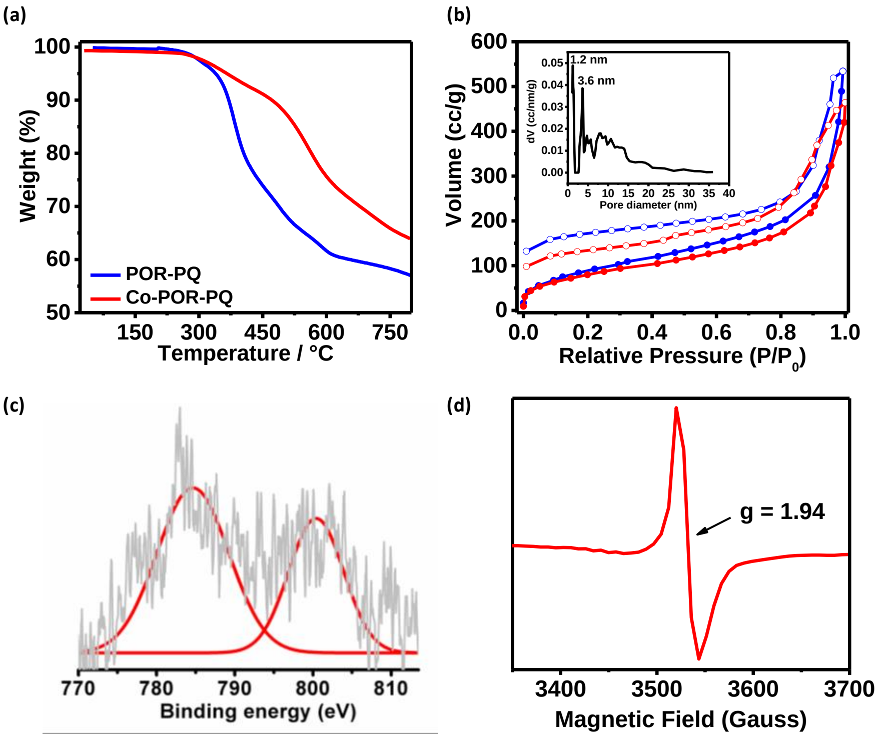

Figure 3: (a) TGA curve of **POR-PQ** and **Co-POR-PQ**; (b) N$_2$ adsorption curve at 77 K (Blue: **POR-PQ**, Red: **Co-POR-PQ**, solid dots: adsorption, hollow dots: desorption, inset: pore size distribution of **POR-PQ**; (c) XPS analysis of **Co-POR-PQ**; (d) EPR spectrum of **POR-PQ**.

TGA of the synthesized **POR-PQ** and **Co-POR-PQ** frameworks (Figure 3a) showed high stability till 250 ^{0}C without any observable decrease in weight of the sample. So, the samples were degassed at 190 ^{0}C under high vacuum to study the porosity of CMPs. Interestingly, N$_2$ adsorption of **POR-PQ** at 77 K showed type II profile with high uptake of 534 mL/g at the relative pressure of 1 as shown in Figure 3b. The isotherm gave high BET surface area of 316 m^2/g showing porous nature of the synthesized framework. Fitting of the isotherm with a non-local DFT model (NLDFT) revealed an average pore diameter of 1.2 nm along with several minor peaks in the range of 3.6 to 13.3 nm and this suggested coexistence of both micro- and mesopores in the framework. Whereas, **Co-POR-PQ** showed decreased N_2 uptake of 463.8 mL/g (at $P/P_0 = 1$) with reduced BET surface area of 192 m^2/g indicating the presence of cobalt in the pores of the porphyrin ring. Further, XPS (Figure 3d) was carried out to confirm the valence of cobalt and as expected, peaks at 800.4 eV and 784.6 eV corresponding to Co(II) were only obtained and thus confirming the coordination of Co into porphyrin ring.[38, 39]

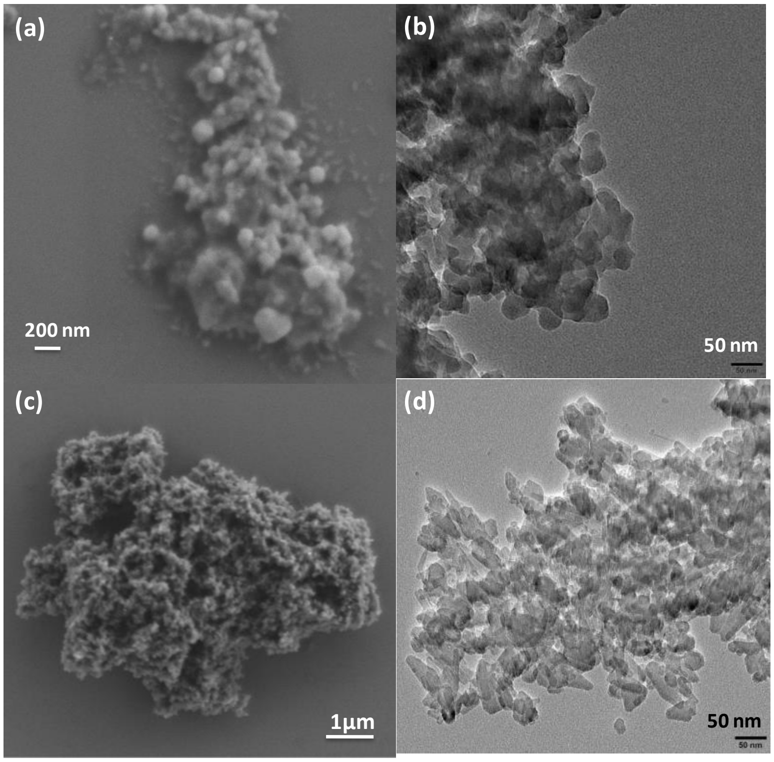

Figure 4: (a,b) FESEM and TEM images of **POR-PQ**; (c,d) FESEM and TEM images of **Co-POR-PQ**.

FESEM and TEM images of **POR-PQ & Co-POR-PQ** were recorded to study the morphology, which showed the presence of aggregated flaky particles. Further, the EPR spectra revealed the presence of charge separation in **POR-PQ** with the *g* value of 1.94 which indicated a single electron transfer from donor node (porphyrin) to acceptor linker (phenanthrenequinone) strut in the polymer network.

3.2 Electrochemical behavior

The presence of phenanthrenequinone with two carbonyl groups in conjugation with each other inspired us to study the redox active behavior of the framework. So, cyclic voltammetry curve of **POR-PQ** was recorded in anhydrous acetonitrile with tetrabutylammonium hexaflorophosphate ($TBAPF_6$) as supporting electrolyte. Interestingly, two reduction peaks at -0.9 V and -1.2 V were observed which corresponded to the conversion of **PQ** to radical anion and dianion, respectively along with their oxidation peaks. This showed the redox active nature of the formed framework.

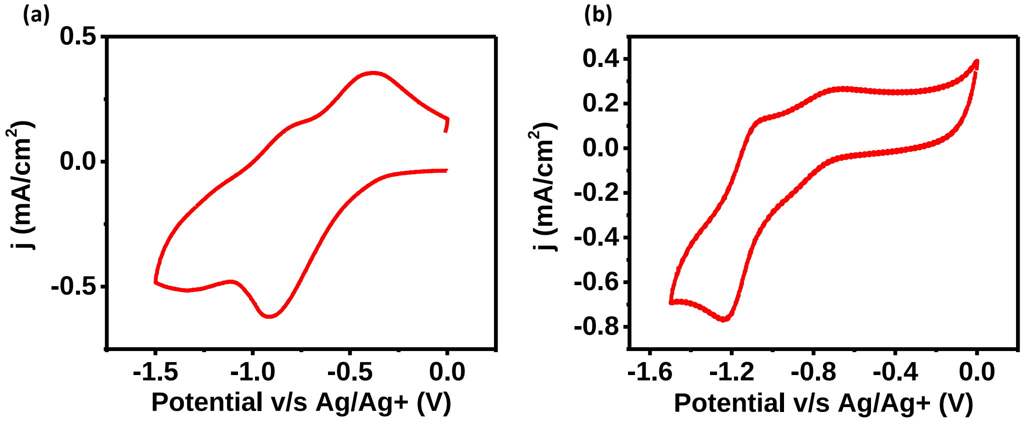

Figure 5: CV of (a) Phenanthraquinone; (b) **POR-PQ** showing the charge separated state.

The redox active nature, donor acceptor design of the framework, high stability due to formation of covalent bond between node and linker, and the presence of complete delocalization inspired to use **POR-PQ** as the electrocatalyst.

3.3 Oxygen Reduction Reaction by Metal Free POR-PQ

Many nitrogen containing nanostructures are found out be active for ORR due to the presence of active binding centre for oxygen. So, **POR-PQ** was studied for its activity towards oxygen reduction reaction (ORR). As a first step towards ORR, CV was performed in 0.1 M KOH under argon and oxygen atmosphere as shown in the Figure 6a. Interestingly, no peak was observed in argon saturated solution whereas a sharp reduction peak at -0.58 V was observed on saturating the solution with oxygen indicating the oxygen reduction reaction. To study the activity of **POR-PQ**, LSV curves were recorded at different rotation speeds of rotating disc electrode. It was observed that **POR-PQ** showed maximum current density of -6 mA/cm^2 at 1600 RPM with low onset of 0.89 V (v/s RHE). Moreover, current density of -1 mA/cm^2 was observed at low potential of 0.77 V.

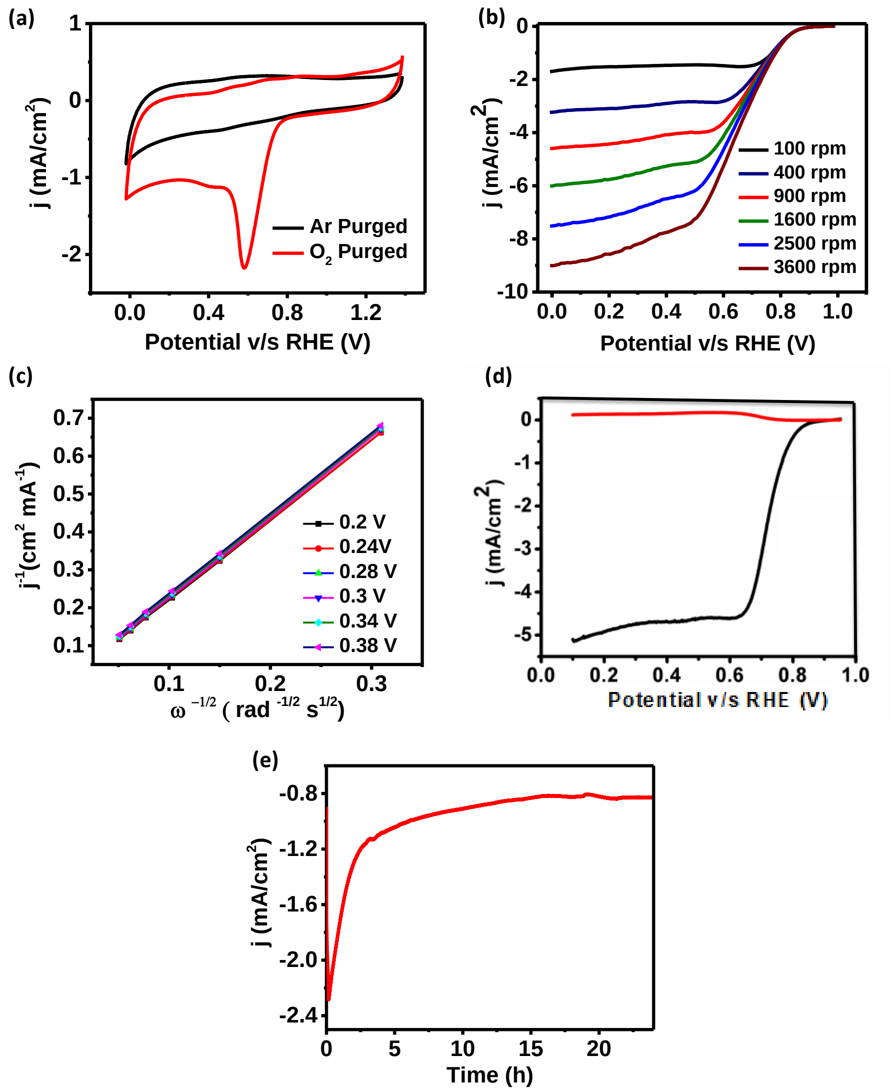

Figure 6: (a) CV in Ar saturated and O_2 saturated medium; (b) LSV curves at various rotation speeds; (c) K-L plot; (d) RRDE curve; (e) Chronoamperometry curve of **POR-PQ**.

The current density increased on increasing the rotation speed of electrode due improved mass transport (Figure 6b). The number of electron transferred during the reaction was found out from the Koutecky-Levich (K-L) plot (Figure 6c) and rotating ring disc electrode (RRDE) analysis (Figure 6d). ORR was found to proceed through four electron process as found shown by K-L plot in Figure 6. The linearity of the K-L plot indicates the first order kinetics with respect to the dissolved oxygen. Moreover, RRDE also showed $4e^-$ transfer with 1.1 % of H_2O_2 production. Further, for any useful application the catalyst must be high stable. So, to check the stability of **POR-PQ**, chronoamperometry was carried out for 24 hours and no significant change of current density was observed, as in Figure 6e, and thus proving robust nature of the electrocatalyst.

3.4 Electrocatalysis of Co-POR-PQ

Recently, Maji *et al*. showed Co(II) containing CMP active towards oxygen evolution reaction (OER)[40] where as Bhaumik *et al*. showed a porphyrin containing metal free CMP active towards hydrogen evolution reaction (HER).[41] So to strive for a trifunctional catalyst active towards ORR, OER as well as HER, Co(II) was metallated into the porphyrin ring which was coupled to PQ to form a conjugated microporous polymer (**Co-POR-PQ**). As **Co-POR-PQ** contained Co(II) doped porphyrin ring with large number of nitrogen centers as the binding site for oxygen in close proximity, oxygen reduction reaction (ORR) was studied (Figure 7). The sample was coated onto the glassy carbon electrode along with 50 wt% of Vulcan C and nafion binder. This was first investigated by CV in both Ar saturated & O_2 saturated 0.1 M KOH (Figure 7a). In oxygen purged electrolyte, a reduction peak of oxygen at 0.63 V was observed which was absent in Ar saturated electrolyte. To study the activity, LSV curves recorded by RDE technique in O_2 saturated electrolyte at the scan rate of 5 mA/cm^2, showed that the current density increases on increasing the rotating speed of the electrode due to the improved mass transport. As it can seen in Figure 7b, high current density of 5.76 mA/cm^2 was obtained with the low onset potential of 0.879 V at the rotation speed of 1600 rpm. Current density of -1 mA/cm^2 was obtained at the potential of 0.786 V which is found to be better than most of the reported values with organic polymers as the catalyst. To study the kinetic parameters, K-L equation was used. The linear nature of the obtained K-L plot (Figure 7c) showed that the reaction followed first ordered kinetics at the concentration of the dissolved oxygen. Further, to find the number of electron transfer during the oxygen reduction reaction and the amount of H_2O_2 produced, RRDE analysis was performed (Figure 7e). This showed that the 13.8 % of H_2O_2 was produced and 3.7 electrons transfer was found to be occurring at 0.3 V showing the reaction proceeds through four electron transfer pathway. Chronoamperometric curve was recorded at the potential of 0.69 V v/s RHE to check the stability of the sample (Figure 7d). It was found the current density was constant for the experimental period of 24 hours. This is due to the strong covalent bond between the donor node and the acceptor spacer.

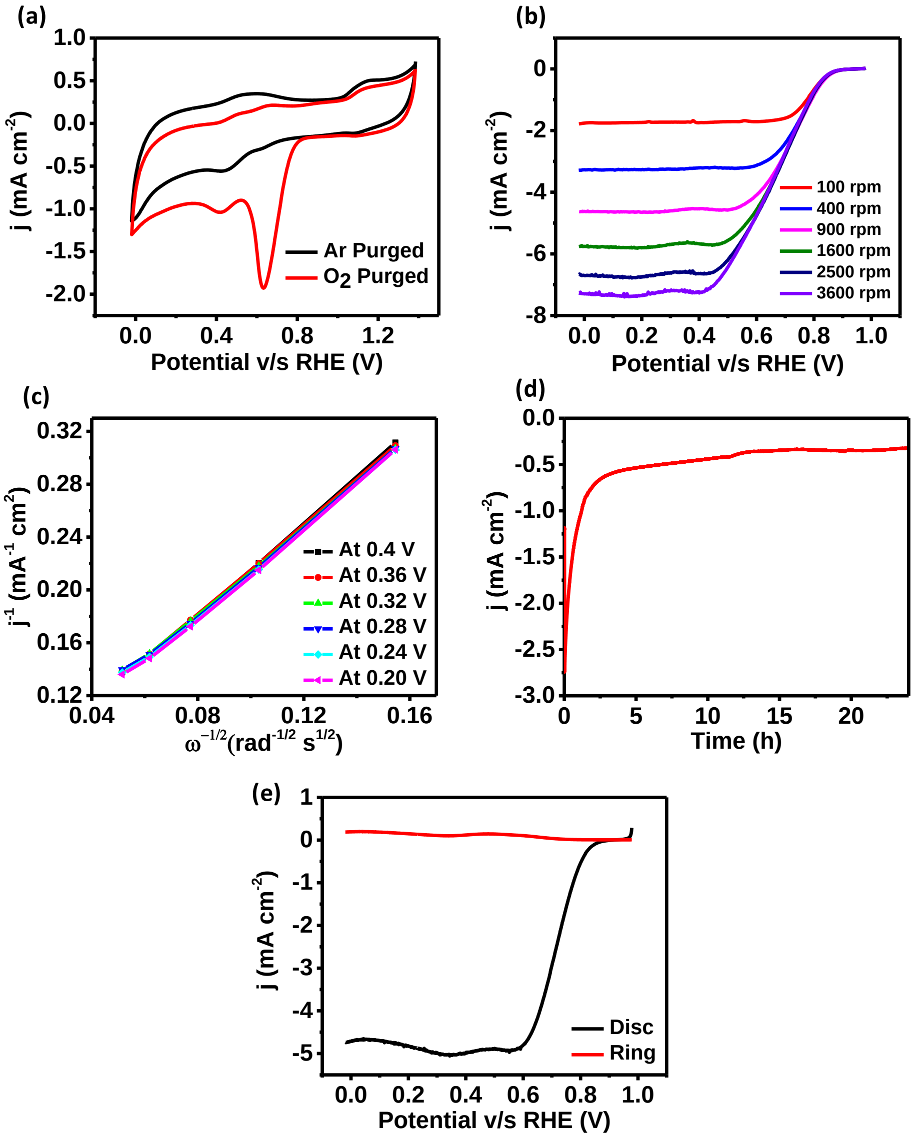

Figure 7: (a) CV in Ar and O$_2$ atmosphere; (b) LSV curves at different rotation speeds; (c) K-L plot; (d) Chronoamperometry curve; (e) RRDE curve of Co-**POR-PQ**.

Further, the presence of Co(II) motivated us to study the oxygen evolution reaction. The CV was recorded in 0.1 M KOH solution and maximum current density of 14.16 mA/cm^2 was observed (Figure 8a). To study the activity of the sample, LSV was recorded at a scan of 5 mV/s and at rotation speed of 1600 rpm. This showed maximum current density of 21.33 mA/cm^2 with the low onset potential of 1.56 V and reached the current density of 10 mA/cm^2 at a potential of 1.82 V v/s RHE.

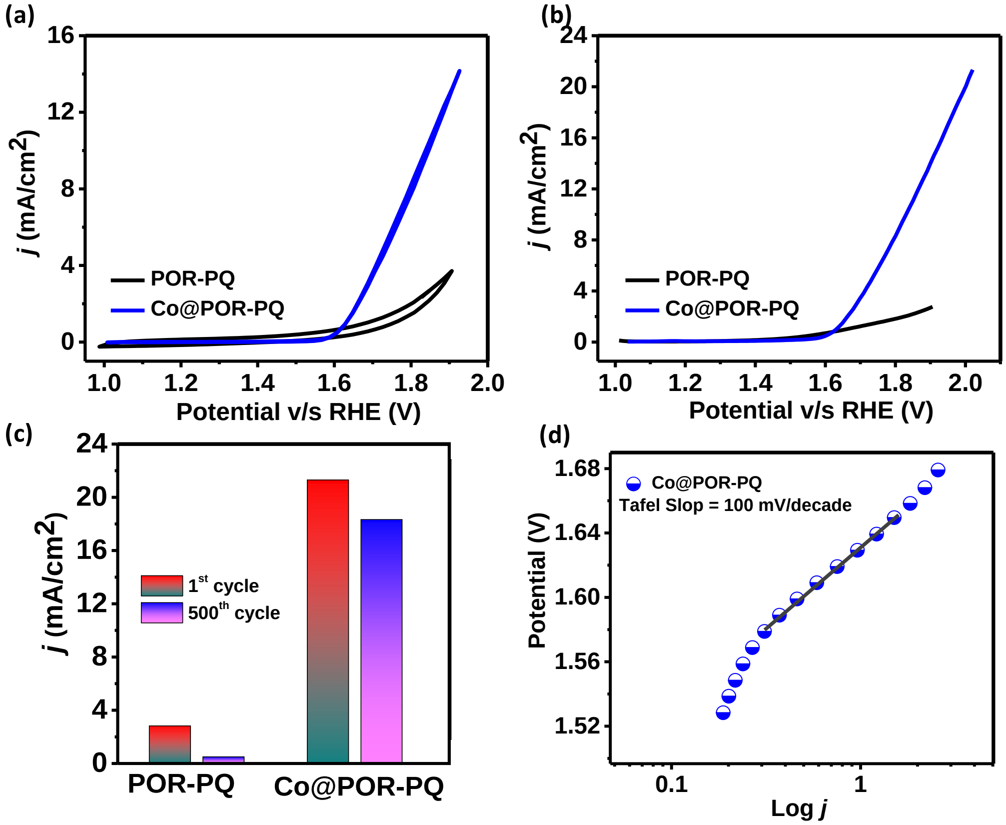

Figure 8: (a) CV of **POR-PQ** & **Co-POR-PQ** in Ar atmosphere; (b) LSV curve; (c) Plot showing current density before and after 500 cycles; (d) Tafel Plot of **Co-POR-PQ**.

On the other hand, the metal free **POR-PQ** was found out to be inactive towards OER with very low current density of 2.76 mA/cm^2 as seen in Figure 8b). So the presence of Co(II) is expected to be an active centre and responsible for OER activity. Moreover, the tafel slope of **Co-POR-PQ** was found out to be 100 mV/decade in the potential range of 1.57 V to 1.64 V (v/s RHE) (Figure 8d). To check the stability of the catalyst formed, 500 cycles of LSV were performed (Figure 8c). The current density changed from 21.3 mA/cm^2 to 18.33 mA/cm^2 after 500 cycles whereas, the metal free CMP showed large decrease in the current density of 2.32 mA/cm^2.

3.5 Zn-Air Battery

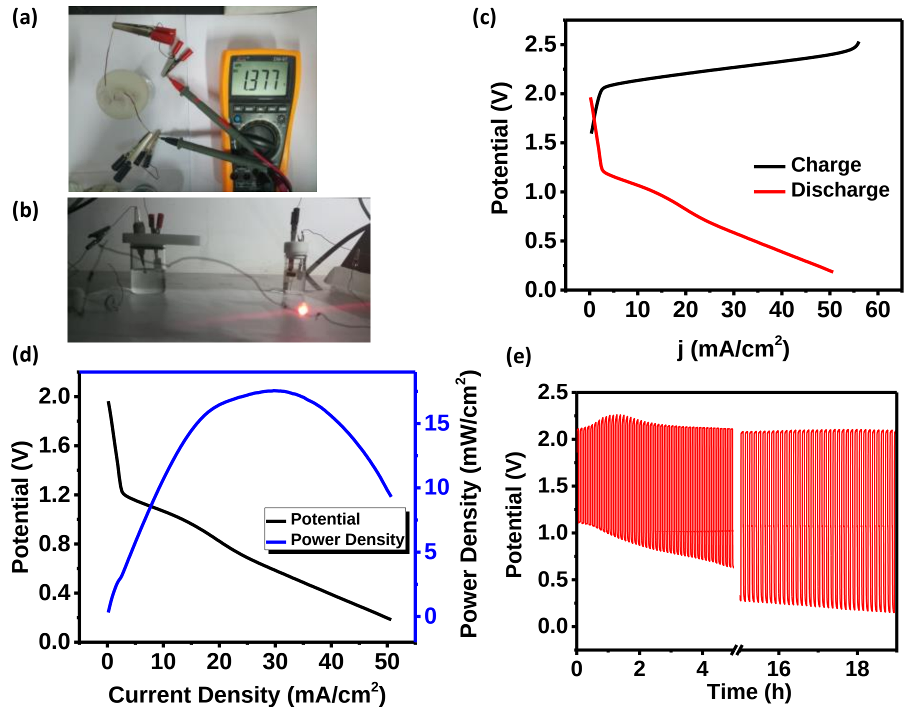

Figure 9: Optical image (a) showing OCP of Zn-Air battery (b) Bright RED glowing LED; (c) Galvanodynamic charge discharge curve; (d) Power density curve; (e) Galvanostatic charge discharge curve of **Co-POR-PQ**.

As the conjugated microporous porous polymer **Co-POR-PQ** possessed both ORR and OER, an electrically rechargeable Zinc-air battery was constructed in two electrode system with the material coated on carbon paper as a cathode and zinc foil as an anode. The open circuit voltage was found to be 1.37 V as shown in Figure 9a. Galvanodynamic charge discharge curve showed the current density of 50.7 mA/cm^2 at the potential of 0.2 V. From the discharge curve the maximum power density was calculated to be 18 mW/cm^2. To check the cycling stability of the constructed battery, galvanostatic charge discharge curves (Figure 9e) were obtained at a current density of 5 mA/cm^2. It was observed that the battery retained its initial charge discharge voltage for initial few cycles but as the cycling continued, the difference between the charged and discharged voltage changed drastically from 1 V to 2.7 V after 19 hours of cycling. It has been shown by Verpoort *et al*. that the battery in three electrode system posses better cycling stability because it prevents the use of same electrode from both oxidative and reductive potential.[42] So the increase in difference may be due to the battery cycling in two electrode configuration as the same electrode is used for both charging and discharging purpose. Further to obtain its practical application and the ability to meet the required power density, the cells can be connected in series or parallel connection. As an illustration of the same, the two cells are connected in series along with a 100 ohm resistance to light up a standard red LED.

3.6 Hydrogen Evolution Reaction (HER)

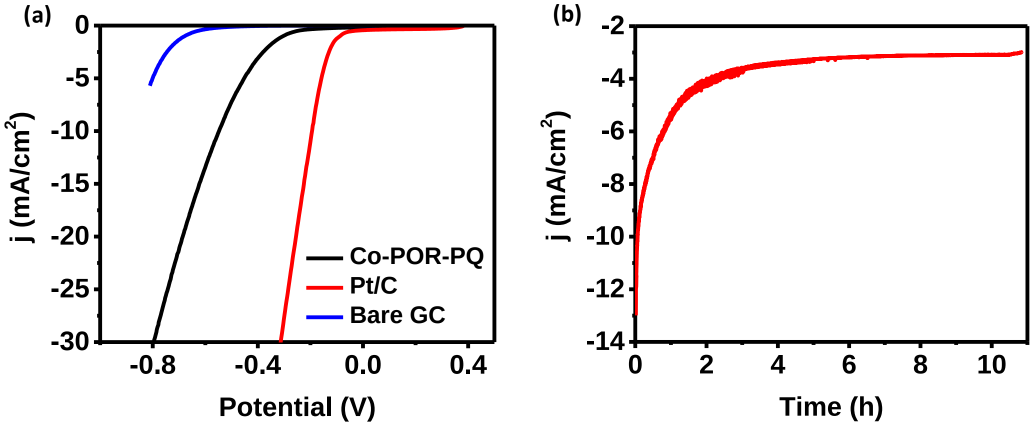

Figure 10: (a) LSV Curves of **Co-POR-PQ**, Pt/C and Bare GC; (b) Tafel Plot; (c) Chronoamperometry curve of **Co-POR-PQ**.

Figure 10a shows the HER polarization curves of **Co-POR-PQ**, Pt/C and bare glassy carbon electrode in 0.5 M H_2SO_4. With **Co-POR-PQ** as the catalyst, the onset potential of the reaction was found out to 225 mV after which the current density increased rapidly. Moreover the working potential of 0.547 V was found at the current density of 10 mA/cm^2 with an overpotential of 354 mV as compared to the state of art catalyst Pt/C. Further, to study the kinetics of the reaction, Tafel slope of 232 mV/decade was obtained. The high tafel slope indicated slower kinetics of **Co-POR-PQ** in comparison to state of art catalyst Pt/C. For the use of the catalyst in applications, one of the most important parameter is its stability. So, on studying the stability of **Co-POR-PQ** by chronoamperometric technique (Figure 10b), no significant decrease in the current density was obtained even after 11 hours. This may be due to the roboust nature of the **Co-POR-PQ** framework, and densely and tightly packed Co(II) ions in the porphyrin ring.

3.7 Self-Powered Overall Water Splitting

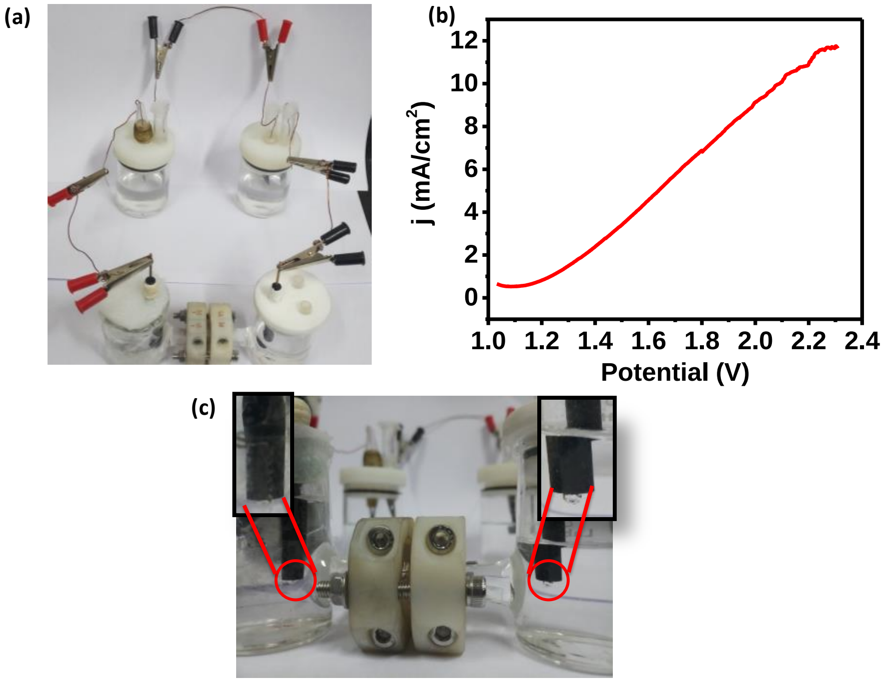

Figure 11: (a) Optical image showing two Zn-Air batteries connected in series which intern is connected to water electrolyser (b) Polarization curve of water electrolyser; (c) Optical image showing formation of O_2 and H_2 bubbles on the GC electrode with **Co-POR-PQ** coated (inset: magnified image)

As expected, **Co-POR-PQ** being trifunctional in nature possessed ORR, OER as well as HER, we thought to use the same material both as anode and cathode in water electrolyser as well as a cathode in Zn-air battery and thus power the water electrolyser with the battery fabricated with **Co-POR-PQ** as shown in Figure 11a. Water splitting was carried out in H-type cell along with Nafion 117 membrane between two compartments as shown in Figure 13a. The porous polymer **Co-POR-PQ** was coated onto two GC electrodes. The same **Co-POR-PQ** was used as the cathode material for Zn-air battery. To overcome the overpotential required for OER and HER reaction, two cells were connected in series (Figure 11a). The positive terminal of the resultant battery was connected to the anode of the electrolyser (undergoes water oxidation reaction) and the negative terminal was connected to the cathode (undergoes hydrogen evolution reaction). The discharge of the battery was across the electrolyser and thus the evolution of oxygen and hydrogen bubbles were seen on the GC electrodes as shown in the Figure 11c and thus showing self powered overall water splitting. Further to the polarization curve recorded in a two electrode configuration (Figure 11b) showed less potential of 2.08 V is required to achieve a current density of 10 mA/cm^2.

3.8 Computational Results

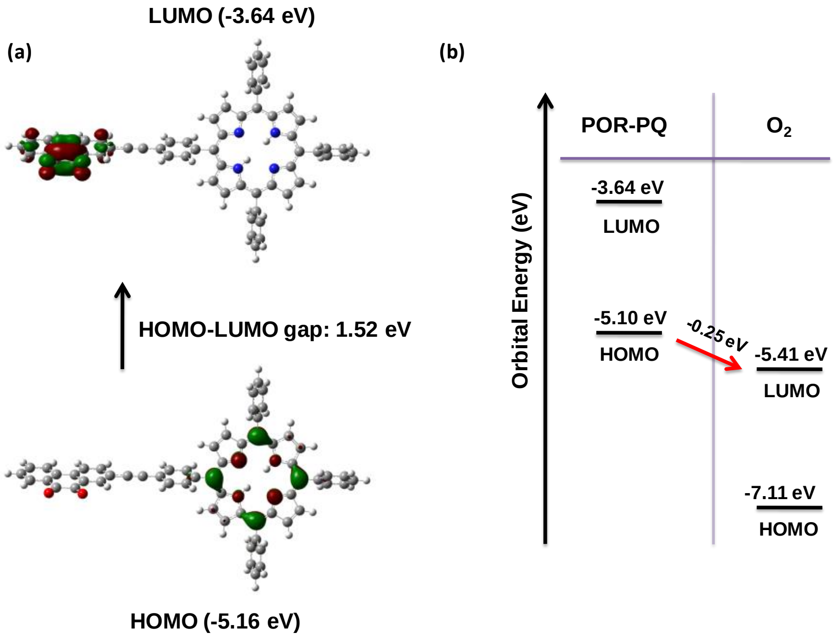

Figure 12: (a) Representation of HOMO-LUMO of **POR-PQ**; (b) HOMO-LUMO levels of **POR-PQ** with dioxygen.

To show the charge separated states, DFT calculations were performed. Molecular orbital analysis of the **POR-PQ** (containing **POR** and **PQ** unit) showed that highest occupied molecular orbital (HOMO) lies on **POR** unit whereas, lowest unoccupied molecular orbital lies on **PQ.** This showed that **POR** unit acts as a donor whereas **PQ** unit act as an acceptor (Figure 12a) and thus forms a donor acceptor system. HOMO-LUMO band gap was found out to be 1.52 eV and thus showing the semiconducting behavior. To study ORR, energies of HOMO and LUMO levels of dioxygen were calculated and compared with those of **POR-PQ**. For ORR, the electron transfer should take place from HOMO of the catalyst to LUMO of dioxygen. As shown in Figure 12b, LUMO of dioxygen is situated lower than HOMO of **POR-PQ** by 0.25 eV. This indicates that the electron transfer from POR-PQ to dioxygen is feasible and thus **POR-PQ** is found to be active for ORR.

4. Conclusion

Excitingly, metal free redox active donor-acceptor organic conjugated microporous polymer was carefully designed and synthesized which showed high catalytic activity towards ORR with low onset potential, high current density and stability. Further, doping of cobalt lead to the transformation from monofunctional electrocatalyst to a trifunctional electrocatalyst which possessed ORR, OER as well as HER. The porous polymer **Co-POR-PQ** being trifuntional in nature was used as a cathode material in electrically rechargeable Zn-air batteries and also as both anode and cathode material in water electrolyser. Finally, the fabricated Zn-air battery with **Co-POR-PQ** as the cathode material successfully powered the water electrolyser and thus splitting water into clean fuels i.e hydrogen and oxygen with less potential of 2.08 V only. It is believed that the development of the organic conjugated microporous trifunctional electrocatalyst will open up a new branch of materials for cathode in Zn-air batteries and water electrolyzers.

5. References

1. S. D. Musa, T. Zhonghua, A. O. Ibrahim and M. Habib, *Renew. Sust. Energ. Rev.*, 2018, **81**, 2281.
2. F. Barbir, T. N. Veziroğlu and H. J. Plass, *Int. J. Hydrogen Energy*, 1990, **15**, 739.
3. P. Perera Frederica, *Environ. Health Perspect.*, 2017, **125**, 141.
4. L. An, T. S. Zhao and Y. S. Li, *Renew. Sust. Energ. Rev.*, 2015, **50**, 1462.
5. Z. P. Cano, D. Banham, S. Ye, A. Hintennach, J. Lu, M. Fowler and Z. Chen, *Nat. Energy*, 2018, **3**, 279.
6. J. Ding, S. Ji, H. Wang, B. G. Pollet and R. Wang, *ChemCatChem*, 2019, **11**, 1026.
7. S. S. Shinde, C. H. Lee, J.-Y. Jung, N. K. Wagh, S.-H. Kim, D.-H. Kim, C. Lin, S. U. Lee and J.-H. Lee, *Energy Environ. Sci.*, 2019, **12**, 727.
8. Z. Song, J. Li, J. Hou, H. Hofmann, M. Ouyang and J. Du, *Energy*, 2018, **154**, 433.
9. Z.-B. Zhai, K.-J. Huang and X. Wu, *Nano Energy*, 2018, **47**, 89.

10. N. Wang, L. Li, D. Zhao, X. Kang, Z. Tang and S. Chen, *Small*, 2017, **13**, 1701025.
11. J. Fu, R. Liang, G. Liu, A. Yu, Z. Bai, L. Yang and Z. Chen, *Adv. Mater.*, 2018, **0**, 1805230.
12. B. Zhu, D. Xia and R. Zou, *Coord. Chem. Rev.*, 2018, **376**, 430.
13. T. Sun, S. Zhang, L. Xu, D. Wang and Y. Li, *Chem. Commun.*, 2018, **54**, 12101.
14. J. Zhang and L. Dai, *Angew. Chem. Int. Ed.*, 2016, **55**, 13296.
15. Y. Jia, L. Zhang, A. Du, G. Gao, J. Chen, X. Yan, C. L. Brown and X. Yao, *Adv. Mater.*, 2016, **28**, 9532.
16. S. J. Visco, M. Liu, M. B. Armand and L. C. de Jonghe, *Molecular Crystals and Liquid Crystals Incorporating Nonlinear Optics*, 1990, **190**, 185.
17. N. Oyama, T. Tatsuma, T. Sato and T. Sotomura, *Nature*, 1995, **373**, 598.
18. H. Kim, J. Lee, H. Ahn, O. Kim and M. J. Park, *Nat. Commun.*, 2015, **6**, 7278.
19. Z. Song, H. Zhan and Y. Zhou, *Angew. Chem. Int. Ed.*, 2010, **49**, 8444.
20. B. Tian, G.-H. Ning, W. Tang, C. Peng, D. Yu, Z. Chen, Y. Xiao, C. Su and K. P. Loh, *Mater. Horizons*, 2016, **3**, 429.
21. S. Renault, V. A. Oltean, C. M. Araujo, A. Grigoriev, K. Edström and D. Brandell, *Chem. Mater.*, 2016, **28**, 1920.
22. T. Yokoji, Y. Kameyama, N. Maruyama and H. Matsubara, *J. Mater. Chem. A*, 2016, **4**, 5457.
23. T. Janoschka, M. D. Hager and U. S. Schubert, *Adv. Mater.*, 2012, **24**, 6397.
24. J. K. Feng, Y. L. Cao, X. P. Ai and H. X. Yang, *J. Power Sources*, 2008, **177**, 199.
25. C. Su, Y. Ye, L. Xu and C. Zhang, *J. Mater. Chem.*, 2012, **22**, 22658.
26. R. Liu, C. von Malotki, L. Arnold, N. Koshino, H. Higashimura, M. Baumgarten and K. Müllen, *J. Am. Chem. Soc.*, 2011, **133**, 10372.
27. C. T. Carver, B. D. Matson and J. M. Mayer, *J. Am. Chem. Soc.*, 2012, **134**, 5444.
28. Z. Chen, D. Higgins, A. Yu, L. Zhang and J. Zhang, *Energy Environ. Sci.*, 2011, **4**, 3167.
29. J. Maruyama, T. Ioroi, T. Hasegawa, T. Mori, Y. Orikasa and Y. Uchimoto, *ChemCatChem*, 2014, **6**, 2197.
30. L. Shang, H. Yu, X. Huang, T. Bian, R. Shi, Y. Zhao, G. I. N. Waterhouse, L.-Z. Wu, C.-H. Tung and T. Zhang, *Adv. Mater.*, 2016, **28**, 1668.

31. Z.-S. Wu, L. Chen, J. Liu, K. Parvez, H. Liang, J. Shu, H. Sachdev, R. Graf, X. Feng and K. Müllen, *Adv. Mater.*, 2014, **26**, 1450.
32. A. Singh, S. Roy, C. Das, D. Samanta and T. K. Maji, *Chem. Commun.*, 2018, **54**, 4465.
33. S. Roy, A. Bandyopadhyay, M. Das, P. P. Ray, S. K. Pati and T. K. Maji, *J. Mater. Chem. A*, 2018, **6**, 5587.
34. J. Yin, P. Zhou, L. An, L. Huang, C. Shao, J. Wang, H. Liu and P. Xi, *Nanoscale*, 2016, **8**, 1390.
35. G. W. T. M. J. Frisch, H. B. Schlegel, G. E. Scuseria, M. A. Robb, J. R. Cheeseman, G. Scalmani, V. Barone, B. Mennucci, G. A. Petersson, H. Nakatsuji, M. Caricato, X. Li, H. P. Hratchian, A. F. Izmaylov, J. Bloino, G. Zhe.
36. J. A. H. K. S. Grimme, S. Ehrlich, *J. Chem. Phys., 2010*, **132**, 154104.
37. A. D. Becke, *J. Chem. Phys.,*, 1993, **98**, 5648.
38. D. Sardar, S. K. Neogi, S. Bandyopadhyay, B. Satpati, R. Jain, C. S. Gopinath and T. Bala, *New J. Chem.*, 2014, **38**, 4107.
39. H. Jia, Z. Sun, D. Jiang and P. Du, *Chem. Mater.*, 2015, **27**, 4586.
40. S. A. Bhat, C. Das and T. K. Maji, *J. Mater. Chem. A*, 2018, **6**, 19834.
41. B. C. Patra, S. Khilari, R. N. Manna, S. Mondal, D. Pradhan, A. Pradhan and A. Bhaumik, *ACS Catal.*, 2017, **7**, 6120.
42. T. Wang, Z. Kou, S. Mu, J. Liu, D. He, I. S. Amiinu, W. Meng, K. Zhou, Z. Luo, S. Chaemchuen and F. Verpoort, *Adv. Funct. Mater.*, 2018, **28**, 1705048.